HIGH-RESOLUTION NUMERICAL INVESTIGATION OF HYDRODYNAMICS AND SEDIMENT TRANSPORT WITHIN EMERGENT VEGETATION CANOPY

BY

PALLAV RANJAN

THESIS

Submitted in partial fulfillment of the requirements
for the degree of Master of Science in Civil Engineering
in the Graduate College of the
University of Illinois at Urbana-Champaign, 2018

Urbana, Illinois

Advisor:

Assistant Professor Rafael Omar Tinoco Lopez

Abstract

High resolution Large Eddy Simulations of flow through staggered rigid emergent vegetation patch were performed using a spectral-element based solver, Nek5000. The staggered pattern of vegetation was similar to experiments conducted on the Odell-Kovasznay racetrack flume where a 5 cm gap was created within the vegetation patch to measure flow velocity using a 3D PIV setup. The main objective of this study was to investigate if flow conditions in the gap are representative of that within the array of vegetation. Flow characteristics such as time averaged velocity, turbulent kinetic energy, bed shear stress and turbulence intensity were investigated for increasing Reynolds number of the flow, and it was found that experimental measurements within the gap would be non-representative of flow conditions within the array. Further, a suspended sediment transport model was developed in Nek5000 and was used to simulate suspended sediment transport within a patch of emergent rigid vegetation. The results were found to be in good agreement with the theory, making it probably one of the first successful attempts at high resolution LES of suspended sediment transport through vegetation canopy.

||आ नो भद्राः क्रतवो यन्तु विश्वतः||

Let noble thoughts come to us from all directions

To my eternal inspiration - Swami Vivekananda

Acknowledgments

This work would not have been possible without the technical, personal, and practical support of a host of people. Foremost acknowledgment belongs to my adviser, Prof. Rafael Tinoco, who not only directed me into this field of research and gave me an excitement for a study that crosses the departmental divide, but also provided every possible resource to help me mature as a graduate student. Bridging this interdisciplinarity would not have been possible without constant mentoring and support from Prof. Paul Fischer, the Nek5000 group (a.k.a *Neks)* and Dr. Som Dutta. Som has invested both technically and emotionally in this work, mostly during our long conversations (and free coffee for me) at some cafe in Urbana-Champaign. He initiated me into the area of high resolution CFD and helped me mature as a researcher by training me to ask the correct questions. Special thanks to fellow Nekian and friend Ketan Mittal who has waded along in tricky situations and helped in creating mesh for the simulations. Appreciation for my friend Dimitrios Fytanidis, who gave very helpful insights from his experience and bore with me during some long debugging sessions. Many thanks to him and the other ecohydraulics and ecomorphodynamics group members, Jorge San Juan, Andrew Leman, Chien-Yung Tseng, Andr´es Prada, and Jieyu Qin for being such good friends and coworkers over the past two years.

This research is part of the Blue Waters sustained-petascale computing project, which is supported by the National Science Foundation (awards OCI-0725070 and ACI-1238993) and the state of Illinois. Blue Waters (Bode et al., 2013) is a joint effort of the University of Illinois at Urbana-Champaign and its National Center for Supercomputing Applications. I'm

thankful to the Blue Waters project for providing me the requisite computational resources, without which this work would have been unfathomable. I am also grateful to the Ravindra K and Kavita Kinra fellowship and Civil and Environmental Engineering Department at the University of Illinois, Urbana-Champaign, for their financial support in the completion of this study.

I'm always grateful to my family who have made numerous sacrifices and gone great lengths to support my endeavors. Wherever I stand today, is due to the blessings of my parents and the omnipresent divine.

Contents

List of Symbols

u_i	Instantaneous velocity of fluid
U_i	Mean velocity of fluid
ρ	Fluid density
p	Fluid pressure
μ	Dynamic viscosity of fluid
x_i	Coordinates associated with the system
f_i	External body forces acting on the fluid
δ_{ij}	Kronecker delta function
$\tilde{x_i}$	Non-dimensional coordinates associated with the system
t	Time
$\tilde{t}$	Dimensionless time
$\tilde{p}$	Dimensionless pressure
H	Height of the channel
d	Diameter of rigid cylinders
h	Half channel height
U_b	Bulk velocity of the fluid
∇	Dimensionless vector differential operator
Re_b/Re	Bulk Reynolds number of the flow
$\tilde{u}$	Dimensionless velocity of the fluid
k	Turbulent Kinetic Energy of the fluid

λ	Canopy density
n	Number of cylinders
A	Area of the channel bed
X	Streamwise coordinate
Y	Spanwise Coordinate
Z	Vertical coordinate
u_i'	Fluctuations in flow velocity
τ_{ij}	Reynolds stress tensor
u_x	Component of fluid velocity in streamwise direction
u_y	Component of fluid velocity in spanwise direction
u_z	Component of fluid velocity in vertical direction
$lx1$	Polynomial order
u'_{rms}	Root Mean Squared velocity fluctuation
U	Magnitude of mean velocity
I	Turbulence intensity
$\overline{u'v'}$	Component of the Reynolds stress tensor
$\overline{\bullet}$	Ensemble mean operator
$\langle\bullet\rangle$	Spatial averaging operator
$\overline{c}$	Volume suspended-sediment concentration averaged over turbulence
c'	Instantaneous fluctuations in concentration
$\tilde{c}$	Dimensionless sediment concentration
F_i	Volume flux vector of suspended sediment averaged over turbulence
V_s	Fall velocity of sediment in quiescent water
D	Eddy diffusivity of suspended sediment
κ	von Kármán constant
u_*	Shear velocity
c_b	Near bed sediment concentration

$\tilde{\mathbf{V}}_s$	Dimensionless fall velocity vector
$\tilde{V_s}$	Dimensionless fall velocity
Re_τ	Shear Reynolds number of flow
Re_d	Stem Reynolds number
Sc	Turbulent Schmidt number
c^v	Volume averaged sediment concentration
ρ_s	Sediment density
ρ_f	Fluid density
$c^{(h)}$	Horizontally averaged dimensionless sediment concentration
$\tilde{\mathbf{G}}$	Dimensionless pressure gradient
ν	Kinematic viscosity of fluid
V	Volume of a system
Ri_τ	Shear Richardson Number
C_D	Drag coefficient
τ_b	Bed shear stress
$\tilde{L_x}$	Dimensionless length of channel
$\tilde{L_y}$	Dimensionless width of channel
$\tilde{L_z}$	Dimensionless height of channel

Chapter 1

Introduction

Flow through vegetation has been a topic of constant inquiry and investigation. Whether located on the floodplain, on the banks or in the channel, vegetation has extensive impact on the fluvial system and has long been the focus of river management activities. In the following sections, we will review the existing literature on flow through vegetation and describe the merits and concerns of the previous studies which will justify and set the context for the current study. The literature review is subdivided into two sections, namely Experimental and Numerical Studies for the convenience of the reader.

1.1 Literature Review

Historically, aquatic vegetation has been treated as a source of hydraulic resistance which impedes the conveyance of channels and aggravates flooding (Kouwen & Unny, 1973), resulting in their removal from streams, canals and rivers. However, over the last few decades, positive ecological effects of vegetation have been identified. Being primary producers, aquatic vegetation plays a vital role for many food webs (E. P. Green et al., 2003) and enhance local water quality by filtering nutrients and heavy metals. Also, drag created by vegetation canopies reduce bed shear stress, enhancing sedimentation and nutrient retention, which creates a more suitable habitat for benthic fauna (Sand-Jensen et al., 1989; Carpenter & Lodge, 1986). Studies on the effects of aquatic vegetation on erosion control, stream restoration, bank stability and pollutant filtering, and wildlife habitat among others, established aquatic vegetation as stream engineers (Koch, 2001), furthering its ecological importance.

This new attitude towards aquatic vegetation, brings about an increased need to understand flow through and above vegetation. A vital component to understanding the overall effect of vegetation is to understand the hydrodynamics of flow in vegetated channels, and how it drives other physical, chemical and biological processes.

1.1.1 Experimental Studies

Hydraulic resistance offered by vegetation is influenced by plant morphology, stiffness and distribution pattern within channel. Over the decades, there have been numerous attempts to convert these heterogeneous characteristics into a simple predictor for a roughness coefficient, but it still remains a challenge. Pioneering work on flow through vegetated channels was done by Ree and Palmer (1949) who accounted vegetation for increased roughness in channels and characterized it by adjusting the Manning's roughness coefficient. They concluded that the relation between Manning's roughness n coefficient and product of channel mean velocity U and hydraulic radius R_h is dependent on the physical properties of grass and independent of channel geometry and flow conditions. Chow (1959) presents a summary of the traditional approaches in the calculation of Manning's roughness coefficient for rivers and channels and makes attempts to characterize the Manning's roughness coefficient for flow in vegetated open channels (Chow, 1959). The values of Manning's n for natural streams with varying vegetation density given by Chow (1959) have been referred by hydraulic engineers for decades to estimate discharge in rivers and channels. However, Chow (1959) doesn't give a generalized relationship between hydraulic resistance and quantifiable vegetation characteristics. In attempts to derive generalized formulations for flow resistance due to vegetation, coupled with the development of novel experimental techniques and unprecedented computational ability, the research emphasis shifted from micro level characteristics (Manning's n) to micro level understanding of drag and turbulence characteristics at both individual stem and patch scales. Understanding of such micro characteristics of the flow can be translated into accurate predictors for resistance coefficients at the reach level. Moreover, conventional

resistance (Manning's, Chezy's, Darcy-Weisbach) are unfitting for flow through emergent vegetation because, where resistance is primarily offered by vertically varying stem drag rather than by shear stress at the bed.

Flow resistance problems can be classified into two groups: flow through submerged, and flow through emergent vegetation. It is found that the velocity profile, drag and turbulent characteristics vary drastically among these cases. While emergent vegetation damps the mean flow velocity throughout the channel depth, submerged vegetation results in the formation of a shear layer at the interface, resulting in an inflection point in the velocity profile near the shear interface (Fig.1.1). In addition to affecting the mean velocity, vegetation also affects the turbulence intensity and diffusion. Mean kinetic energy of the flow is converted into turbulent kinetic energy at the scale of plant stem, enhancing turbulence intensity. Diffusion is limited due to reduction of turbulent length scales compared to open channels (H. Nepf et al., 1997). Further complexity arises upon considerations of flexibility in vegetation.

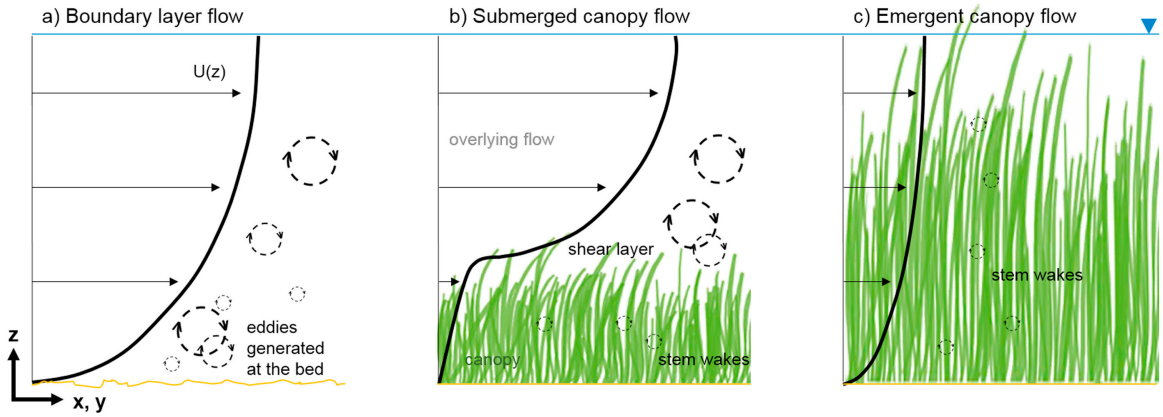

Figure 1.1: Velocity profile for channel with a) no vegetation b) submerged vegetation and c) emergent vegetation (Beudin et al., 2017)

Li and Shen (1973) studied the wake of several vegetation patterns and developed a mathematical model to estimate the flow resistance due to different arrangement patterns of tall rigid vegetations and hence calculated the reduction in sediment yield due to reduced flow

rates. Petryk and Bosmajian III (1975) presented a model to estimate Manning's n as a function of hydraulic radius and vegetation density for emergent rigid vegetation and established that roughness coefficient increases in proportion to two-thirds power of hydraulic radius for constant vegetation density and flow depth. Extending the work of Li and Shen (1973), a method to calculate the drag coefficient of single plant in a group (C_{WR}) and a friction factor for vegetation (f_p) was developed by Lindner (1982). On the basis of a one-dimensional model regarding turbulent shear stresses as apparent wall shear stresses in vegetatively roughened flood plains, Pasche and Rouvé (1985) developed a relation to predict roughness induced by rigid emergent vegetation as a function of independent and deterministic flow parameters. Chen (1976) conducted experiments on laminar flow in shallow grassed channels to characterize flow resistance in terms of the Darcy-Weisbach friction coefficient and found that friction factor decreases with Reynold's number, but increases with the slope.

Extending the flow resistance formulations developed for rigid vegetation would give a wrong predictions for scenarios with flexible vegetation. To account for flow resistance due to flexible vegetation, Kouwen and Unny (1973) defined dimensionless parameters which relate the shear induced by boundary roughness to its stiffness. Fathi-Maghadam and Kouwen (1997) conducted experiments on flow through emergent flexible vegetation using tree saplings to obtain relationship between roughness conditions (i.e. density and flexural rigidity) and flow conditions (i.e. velocity and depth) for floodplains and vegetative zones of natural waterways. It was found that friction factor changed significantly with mean flow velocity due to bending of vegetation as a result of linear increase in momentum absorption (i.e. drag force). Oplatka (1998) studied flow resistance of flexible willows and found that the product of drag coefficient and effective plant area, $C_D A_v$, decreases rapidly with increasing velocity to reach an asymptotic value. Wu et al. (1999) investigated the variation of roughness coefficients for increasing water level in a vegetated channel, and found that vegetative roughness coefficient tends to increase with increasing depth up to a certain level, but decreases asymptotically

as the water level continues to rise further.

Several attempts to express the resistance coefficient in the Manning's, Darcy-Weisbach or Chezy form have been summarized in the book *Channel flow resistance: Centennial of Manning's formula* (Yen, 1992). Järvelä (2002) conducted a diverse set of experiments to characterize flow resistance of natural grasses, sedges and willows. They found that friction factor was dependent mostly on relative roughness in case of grasses, on the flow velocity in case of willows and sedges combined, and on flow depth in the case of leafless willows. Stone and Shen (2002) conducted laboratory experiments on submerged and emergent rigid cylindrical vegetation, and developed a generalized method to calculate flow resistance under both emergent and submerged conditions. Accounting for resistance exerted by stem drag throughout the flow, rather than by bed shear stress, James et al. (2004) arrived at an alternate equation form in which the resistance coefficient is related to measurable vegetation characteristics and can incorporate bed roughness when it is significant. Recent experimental studies by J. C. Green (2005, 2006) found that flow resistance due to vegetation is predominantly determined by the spatial distribution of vegetation and hence characterized the spatial distribution in terms of a universal blockage factor.

Conventionally three blockage factors have been used, namely cross-sectional, surface and volumetric blockage factors representing the fraction of vegetation blocking the channel cross-section, surface and volume respectively (Watson, 1987; Champion & Tanner, 2000; Fisher, 1992). Using these, J. C. Green (2006) derived a universal blockage factor to mitigate the inherent biases of the other three. Further Luhar et al. (2008) used the results from J. C. Green (2006) to derive a relation for Manning's n in terms of the three blockage factors. Most recently, Kothyari et al. (2009a) measured drag on a single stem in a staggered patch arranged and found that drag coefficient, C_D depends weakly on stem Reynolds number, R_d and show strong correlation with stem staggering pattern. Based on these findings, a new

relationship for stem drag coefficient was proposed.

While it is important to arrive at empirical solutions to characterize vegetative resistance, it is also imperative to understand the flow structure through the vegetation. Klopstra et al. (1996) derived a generalized velocity profile in emergent vegetation by deriving velocity profiles for both vegetation and surface layer by analyzing momentum equations for the two layers and then smoothly matching the two profiles through boundary conditions at the interface. They assumed steady, uniform flow and used the eddy viscosity model for turbulent shear stress. H. Nepf (1999) developed a model to predict drag, turbulence intensity and diffusion within emergent vegetation of varying density and stem Reynolds number. It was found that the turbulent intensity is directly dependent on vegetative drag, and for vegetation density as low as 1% the bed-drag and bed-shear production are negligible compared to vegetative counterparts. Also, diffusion is reduced within the vegetation as the turbulent length scales, l are reduced and scale with stem geometry, d ($l \sim d$) compared to open channels where it scales with flow depth, h ($l \sim h$). In contrast to free shear layers, which continuously grow downstream, shear layers generated by submerged vegetation are limited to a finite thickness due to coherent vortex structures and vertical mixing (Ghisalberti & Nepf, 2004).

Carollo et al. (2002) arrived at a theoretical four-coefficient velocity profile for vegetated channels based on experimental velocity measurements in flow over flexible bottom vegetation. It was also found that inflection point in velocity profile is located at the depth of maximum turbulent intensity, which is also the height of the bent vegetation. Using a two-layer approach, where flow above and through vegetation layer is described separately, a model for depth averaged flow velocity in presence of submerged vegetation was developed by Huthoff et al. (2007) . Huai et al. (2009) used a three-layer model by dividing vegetation layer in inner and outer layer to derive a representative velocity profile for submerged vege-

tation. However, the contribution of the inner layer to the overall flow appears to be small. García et al. (2004) conducted experiments to investigate flow structure and drag coefficient of rigid and flexible simulated vegetation. The results showed that there is vertical variation in vegetation induced drag coefficient for open channel flows, which had historically been assumed to be a constant (Fig.1.2).

The previous studies some of which are mentioned above (Raupach & Shaw, 1982; Carollo et al., 2002; H. Nepf, 1999; García et al., 2004), use spatial and temporal averaging of velocity profiles obtained at several locations to create a single profile which is representative of a bulk flow behavior. However the inhomogeneity and anisotropy of the flow characteristics through vegetation, result in averaging procedures not representative of the conditions at all locations within the canopy (Fairbanks & Diplas, 1998). Liu et al. (2008) used discrete measurements within the canopy to develop velocity and turbulence intensity profiles and observe the changes in flow characteristics within the patch. The results show that velocity within the array is constant with depth and the velocity profile is logarithmic above it. Yang and Choi (2010) applied the two-layer approach and derived a layer-averaged velocity profile for a submerged flexible canopy and further arrived at an analytical relation for Manning's roughness coefficient.

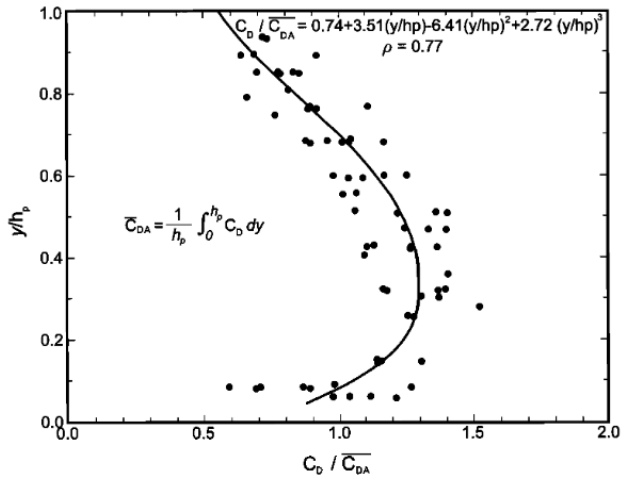

Figure 1.2: Vertical variation of the drag coefficients inside the canopy for rigid cylinders (García et al., 2004)

1.1.2 Numerical Studies

Most of the previous studies have been experimental and field based (H. M. Nepf, 2012), which provide us with valuable insights, but are limited by the capabilities of the instruments being used (Pujol et al., 2013). Quantifying mechanisms of flow and sediment transport withing the canopy requires high resolution flow field data through the canopy, which is still a challenge during experiments. Low resolution of data within the canopy adds significant uncertainty to the estimates of spatially averaged flow properties. In order to get around this issue, the total drag exerted by the canopy has been calculated from energy slopes, exposing the drag estimates to substantial uncertainty (Tanino & Nepf, 2008; Kothyari et al., 2009b).

Recent studies have been able to circumvent the issues associated with the aforementioned drag measurement techniques, by directly measuring the total drag acting on the canopy using a drag plate (Tinoco & Cowen, 2013), however we still need high resolution data of flow field to investigate other flow statistics. This can be remedied by performing high-resolution computational fluid dynamics (CFD) simulations that can provide flow field data at unprecedented resolution. In the past, a limited number of numerical studies on flow through vegetation have been undertaken, and an even lesser number of high-resolution simulations have been performed owing to the monumental cost of such simulations. The majority of CFD models solve a 3D steady or unsteady Reynolds-averaged-Navier-Stokes (RANS) equations and are capable of predicting the time-averaged characteristics of the flow. Vegetation drag in RANS is accounted for by employing an additional source term in the momentum equation and the turbulence transport equations. Additionally RANS equations require modified turbulence closure models for drag-related sink terms in the turbulent transport equations, which requires a-priori knowledge of drag coefficient and additional empirical results (Stoesser et al., 2010).

Lopez and Garcia (1997); López and García (2001) performed numerical studies on steady, uniform flow through vegetation by solving RANS equations using the standard $\kappa - \epsilon$ turbulence closure model with wall functions, with PROBE, which is a RANS based equation solver (Svensson, 1986). They introduced a source term in the RANS equation to represent vegetative drag $F = \frac{1}{2} C_D \lambda |U| U$, where C_D is the local drag coefficient, U is the local time averaged velocity and λ is the local resistance area per unit volume of flow. The κ and ϵ equations were also modified to account for drag related turbulence production. López and García (1998) further performed similar studies to also estimate suspended sediment transport processes within the vegetated channels. Fischer-Antze et al. (2001) performed 3D simulation of flow in channel with submerged vegetation by solving RANS equations with $\kappa - \epsilon$ turbulence closure model using the SSIM model (Olsen & Stokseth, 1995; Stoesser, 1997)and compared the calculated drag force with the findings of laboratory based experiments of (Tsujimoto et al., 1991), (Lopez & Garcia, 1997) and (Pasche, 1984). Furthering the work of (Shimizu, 1994) and (Lopez & Garcia, 1997), Neary (2003) used a $\kappa - \omega$ closure model to simulate flow in channel with submerge vegetation. The closure model is a better predictor of near bed shear stress over the previous $\kappa - \epsilon$ model with wall functions for a wide range of roughness (Patel & Yoon, 1995). The above RANS models with isotropic turbulence closures simulate time averaged flow features, and hence provide a limited description of turbulence statistics within vegetation which is marked by anisotropy. Also, these models are not universal, requiring a priori calibration of drag and other model coefficients. The strength of RANS or unsteady RANS (URANS) models is their computational efficiency and applicability to field scale flows. However they are limited by their inability to resolve flow and predict turbulence around single cylinder or through an array of cylinders (Rodi, 1997; Rollet-Miet et al., 1999).

Recently, Large Eddy Simulation (LES) has become a popular research tool to investigate turbulence dominated flows. LES provides an almost complete description of instantaneous

unsteady 3D turbulent flow field by resolving the large scale eddies resulting from flow instabilities while modeling the small scales of dissipation. Cui and Neary (2002); Stoesser et al. (2006) and Palau et al. (2007) were among the first to use LES to simulate 3-dimensional flow through submerged vegetation. They provided evidence that LES is able to resolve large scale turbulent structures and explain its influence on flow resistance, Reynolds stresses and other turbulent quantities. Later Cui and Neary (2008) furthered their previous work to understand the role of coherent structures on the momentum transfer across the water-plant interface. They modeled the effect of vegetation on flow by introducing a drag term in the momentum equation for all grid points within the vegetation layer. Although this approach doesn't model the flow around individual stems, it still resolves the coherent structures responsible for sweep and ejection events at the top of vegetation, which induces significant momentum exchange and substantial magnification of the Reynolds stress. Stoesser et al. (2009) simulated the experimental setup used by Liu et al. (2008) and provided evidence for the mixing layer analogy proposed by Raupach et al. (1996). Furthering their previous work, Stoesser et al. (2010) performed LES of open channel flow through a staggered array of rigid emergent cylinders. Analyzing the distribution of drag and lift forces on the cylinder, they concluded that flow and turbulence are more influenced by vegetation density than by cylinder Reynolds number. However, this is not a settled debate, as some studies indicate that canopy drag coefficient decreases with increasing density (H. Nepf, 1999) while other studies (Kothyari et al., 2009a; Stoesser et al., 2010; Tanino & Nepf, 2008; Cheng & Nguyen, 2010) point that canopy drag coefficient increases with density. This contradiction calls for detailed investigation of canopy drag by investigating the mechanisms responsible for modifying the canopy drag coefficient.

Based on this argument, Etminan et al. (2017) simulated flow through a staggered array of emergent cylinders and investigated the influence of three mechanisms modifying canopy drag, namely, blockage (Maskell, 1963), sheltering (Raupach, 1992) and delayed separation.

It was found that while sheltering and delayed separation slightly reduced the drag of sparse canopy, the blockage effect significantly increased the drag of dense canopies. Chang et al. (2017) simulated flow around an emergent porous cylinder with varying solid volume fraction (SVF) and studied the turbulence structures, velocity field and bed shear stress and interpolated the it's implications on scour around the cylinders. They used Detached Eddy Simulations (DES) which combines LES with the RANS model to account for unresolved turbulence in RANS. The largest eddies simulated in a LES simulation is limited by the maximum size of the mesh elements, a complete resolution would require the mesh size to be equivalent to the smallest eddy, which would have high computational expense. One can perform Direct Numerical Simulation (DNS) which resolves smallest eddies hence giving the most accurate prediction of turbulence and wake characteristics. Nicolle and Eames (2011) simulated flow through an array of circular cylinders using 2-D DNS, with varying cylinder density to estimate the lift and drag experienced by the cylinders. However, DNS is computationally expensive and has been limited to simulating smaller domains and simple geometries. To the author's knowledge 3D DNS of flow through vegetation has not been performed till date.

1.2 Motivation

This study aims to bridge the gap between numerical and experimental studies by simulating laboratory scale experiments at high resolution using Large Eddy Simulations (LES) and Direct Numerical Simulations (DNS). Experimental measurements of flow field are of coarse resolution limited by the capabilities of the instrument being used, and hence fail to capture the small scale turbulence statistics which affect flow resistance and sediment transport characteristicss of vegetated channels. High resolution numerical simulation can provide information at unprecedented resolution which can be used to predict turbulence statistics with high accuracy. Previous numerical simulations have established that LES

and DNS are remarkable tools to investigate flow over and through vegetation canopy. The maximum number of vegetation elements simulated using LES is 64 (Stoesser et al., 2010), which may provide a very representative picture of most experimental and field scenarios.

This work is a continuation of the previous attempts, but at a higher resolution and with more number of rigid vegetation elements (192) in the canopy. In the current study, a high-order spectral element based incompressible Navier-Stokes solver has been used to conduct 3D high-resolution LES of flow through staggered emergent vegetation canopies; with the goal to analyze the flow structure and canopy drag, with increasing Reynolds number. The staggered pattern of vegetation is similar to the experiments conducted on the Odell-Kovasznay racetrack flume where a 5 cm gap was created within the vegetation patch to measure flow characteristics using a 3D PIV setup. One of the main objectives of this study is to investigate if flow conditions in the gap are representative of that within the array of vegetation.

Further the model has been extended to include suspended sediments which have been been modeled in the Eulerian framework as active scalars. To the author's knowledge, LES of suspended sediment transport through vegetation has not been attempted due to the inherent complexities associated in modeling active scalars and high computational cost involved.

Chapter 2

Theoretical Framework and Model Description

2.1 Introduction

The governing equations for the fluid flow are the Navier-Stokes equations which account for momentum and mass balance within a control volume of fluid. In the past, researchers have accounted for momentum reduction in vegetation canopy by employing an additional sink term in the equations for momentum and kinetic energy (Li & Shen, 1973; Lopez & Garcia, 1997), which requires a case-by-case calibration of the model by estimating the bulk drag coefficient of the vegetation canopy. A better calibration requires better models to estimate drag, which in turn depends on understanding the various mechanisms of drag offered at both stem and canopy levels. In the past this has been attempted both experimentally (H. Nepf, 1999; Liu et al., 2008) and numerically (Stoesser et al., 2010; Etminan et al., 2017), but the problem is still far from settled. In this study, flow through vegetation has been studied by numerically solving the N-S equations for a control volume comprising a channel with rigid cylinders arranged in a staggered array. The current setup numerically replicates experiments performed on the Odell-Kovasznay flume at Ven Te Chow Hydrosystems Laboratory, UIUC. The equations have been solved using a high-order spectral element method based incompressible Navier Stokes solver, Nek5000 (Argonne National Laboratory, Illinois, 2017). For simplicity water has been treated as incompressible fluid with a constant viscosity. The following sections will describe the governing equations and the mathematical model used to understand flow characteristics in open channels with emergent rigid vegetation.

2.2 Governing Equations

The equations for conservation of momentum and mass are collectively called the Navier-Stokes equations, which are given as:

$$Conservation\ of\ Momentum : \frac{\partial u_i}{\partial t} + u_j \frac{\partial u_i}{\partial x_i} = -\frac{1}{\rho}\frac{\partial p}{\partial x_i} + \mu \frac{\partial^2 u_i}{\partial x_i^2} + f_i \tag{2.1}$$

$$Conservation\ of\ Mass : \frac{\partial u_i}{\partial x_i} = 0 \tag{2.2}$$

where,

u_i is the fluid velocity (m/s)

ρ is the fluid density (kg/m^3)

p is the fluid pressure (N/m^2)

μ is the constant fluid viscosity $(m^2/s)$and

f_i is the acceleration induced due to external body forces (m/s^2)

Here we use the tensor notation, x_i to account for the three spatial components, $x_1 = x$ (longitudinal) and $x_2 = y$ (lateral) and $x_3 = z$ (vertical), with their associated velocities, u, v and w respectively. However, for the ease of analysis of the problem which is at study, and to reduce the number of free parameters in the model, the equations are non-dimensionalized using scales for each of the variables. For this study, Height of the channel, H is the length scale, bulk flow velocity, U_b is the velocity scale, $\frac{H}{U_b}$ forms the time scale, and ρU_b^2 is the scale for pressure. Thus, the corresponding non-dimensional variables are,

$$\tilde{x} = \frac{x}{H} \quad \tilde{u_i} = \frac{u_i}{U_b} \quad \tilde{t} = \frac{tU_b}{H} \quad \tilde{p} = \frac{p}{\rho U_b^2} \tag{2.3}$$

Substituting these quantities in equation 2.1 and simplifying, we get the non-dimensional

form of the Navier-Stokes equations:

$$\frac{\partial \tilde{\mathbf{u}}}{\partial \tilde{t}} + \tilde{\mathbf{u}}.\nabla\tilde{\mathbf{u}} = -\nabla\tilde{p} + \frac{1}{Re_b}\nabla^2\tilde{\mathbf{u}} \tag{2.4}$$

$$\nabla.\tilde{\mathbf{u}} = 0 \tag{2.5}$$

where, $\tilde{\mathbf{u}} = (\tilde{u}, \tilde{v}, \tilde{w})$ is the dimensionless velocity vector, and
$\nabla = \left(\frac{\partial}{\partial\tilde{x}}, \frac{\partial}{\partial\tilde{y}}, \frac{\partial}{\partial\tilde{z}}\right)$ is the dimensionless vector differential operator, and
$Re_b = \rho U_b H/\mu$ is the bulk Reynolds number of flow.

2.2.1 Boundary Conditions and Numerical Method

The fluid boundary is considered to be periodic in the streamwise and spanwise directions. At the channel bed and at the cylinders, a no slip boundary condition is applied. The free surface is set as a frictionless rigid lid and is treated as a plane of symmetry. Initially, the fluid is considered to be at rest. Since there is no analytical solution to equations (2.4) and (2.5) along with the above mentioned boundary conditions, the equations were solved numerically using a spectral-element based high order incompressible Navier-Stokes solver, Nek5000 (Argonne National Laboratory, Illinois, 2017).

Spectral element Method (SEM) is used for spatial discretization of the N-S equations. SEM is a high-order method that uses the weighted residual approach similar to finite element method (FEM) (Deville et al., 2002). SEM combines the flexibility of FEM with the high-order accuracy and fast convergence of Spectral methods. Higher-order polynomial based methods are especially suited and necessary for turbulent flow simulations because, high-order polynomial eliminates dispersion errors, which is very important for large-scale and long-term turbulence calculations (Kreiss & Oliger, 1972). For temporal discretization, a semi-implicit time-stepping scheme is used, in which the nonlinear terms of the Navier-

Stokes equation are treated explicitly; and the linear part that is the Stokes problem is treated implicitly. The explicit part of the time derivative is treated using a kth-order Extrapolation scheme ($EXT - k$, where $k = 2, 3$), and implicit part using a kth-order backwards difference formula ($BDF - k$, where $k = 2, 3$). For this study, spectral filtering was used to filter out the energy from the higher modes and prevent energy growth over time. Other models for dissipation such as Smagorinsky (SGS) can also be incorporated in Nek5000. Further details about the solver can be obtained from Fischer et al. (2007).

2.3 Geometric Layout

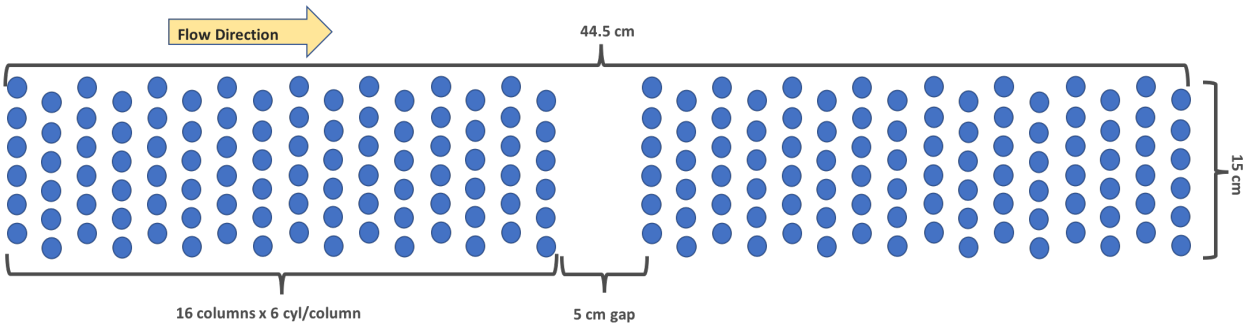

Figure 2.1: Geometric layout for simulation of flow through vegetation

The geometry of this setup (Fig. 2.1) is inspired from the setup of experiments conducted on Odell-Kovasznay racetrack flume (Fig. 2.2) at Ven-Te-Chow Hydrosystems laboratory. 672 rigid cylinders each with diameter of 0.7cm and 10cm height were placed in a staggered manner with 6 cylinders in each column to form an array. Within the array, there was a 5cm gap to monitor the flow characteristics using a 3D PIV setup. The total length of the array of cylinders including the gap was 148.5cm. The mean horizontal distance between each column of cylinders was $\frac{1}{2}$ inch. The mean vertical distance between cylinders at each column was 1 inch. The width of the array is 15 cm which equals the width of the flume. The canopy density λ, i.e. the cross-sectional area per unit bed area in the array is defined

as:

$$\lambda = \frac{1}{A}\left(\frac{n\pi d^2}{4}\right) \tag{2.6}$$

where A is the bed area, n is the number of cylinders, and d is the cylinder diameter. For the current study $\lambda = 0.1106$. Although the actual experimental array was 148.5 cm long, only a portion, i.e. 44.5 cm of the array was simulated numerically. Thus a total of 192 cylinders were modeled in the current study, as opposed to the 672 cylinders in the actual experiments. This was done to contain the expense of the simulations and also because flow patterns in a large staggered array can be replicated on a smaller domain using periodic boundary conditions.

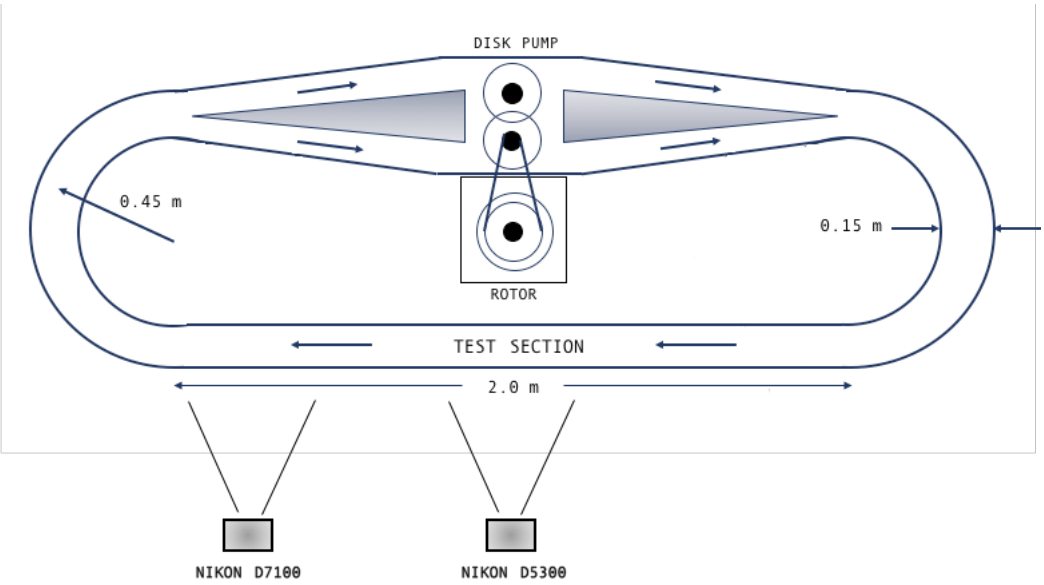

Figure 2.2: Dimensions of the Odell-Kovasznay flume

The mesh generated for the simulations is shown in fig. 2.3. The resolution of the mesh is high enough for a complete resolution of the boundary layer around the cylinders and at the bed of the channel. There are at least 10 points within the viscous sublayer layer of the cylinders and the channel bed, sufficient to caputure the shear stress acting on the bed.

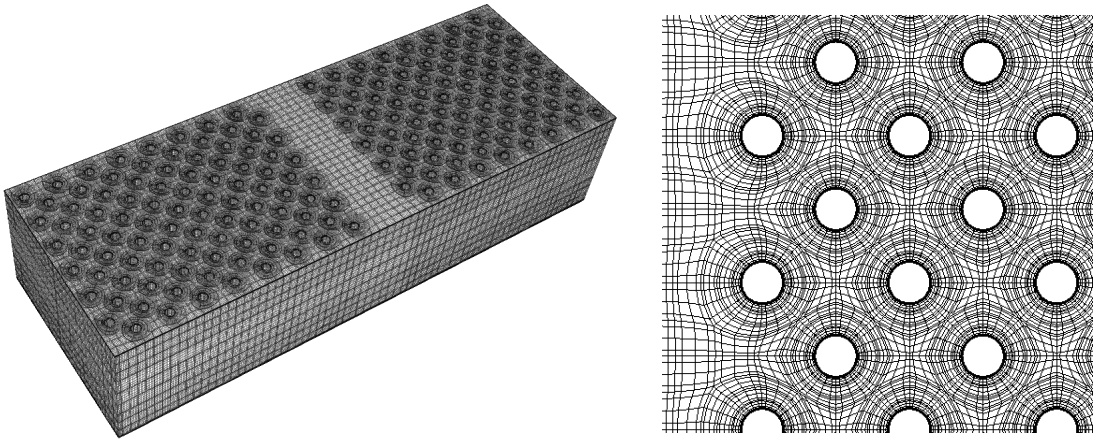

Figure 2.3: Mesh used to simulate flow through vegetation and details of the mesh around individual elements of the array

2.3.1 Cases Simulated

A number of cases were simulated to investigate the effect of increasing flow Reynolds number, Re_b on the flow characteristics within the vegetation patch. The cases and associated sales are summarized in Table 4.1

Table 2.1: Cases simulated for flow through vegetation

Case	Re_b	Length Scale, H (m)	Velocity scale, U_b (m/s)	Time scale, T (s)
Case I	12000	0.1	0.12	0.83
Case II	15000	0.1	0.15	0.67
Case III	18000	0.1	0.18	0.56
Case IV	20000	0.1	0.20	0.50

Chapter 3

Hydrodynamic Results and Discussion

In the following sections the hydrodynamics of flow through vegetation will be discussed and the results will be extrapolated to make comments on drag and sediment transport within the vegetation. Four cases with increasing bulk Reynold's number : $12000, 15000, 18000$& 20000 have been investigated. Flow characteristics have been plotted along the following seven cross-sections as shown in Fig. 3.1. I, II and III represent sections along the channel depth at $Z = 1$, 50 and 97% respectively. IV, V and VI are sections along the channel length at $X = 25$, 50 and 75% respectively, and VII is the cross section along the width of the channel at $Y = 50\%$. The following results are shown in the form of dimensionless quantities, unless mentioned otherwise. One can convert from the dimensionless to the dimensional form using the scales provided in table 4.1. All the results have been visualized using Visit, which is an open source visualization tool (Childs et al., 2012).

3.1 Instantaneous Velocity

Fig. 3.2, 3.3, 3.4 and 3.5 shows the instantaneous velocity field at sections I, II and III for increasing bulk Reynold number. It can be seen that the near bed velocities are lower than the mid channel and near surface velocities. This is evident from shortening wakes of cylinders as we move up along the channel depth. The intermediate area between the two patches is a predominantly low velocity zone for all the cases. However, with increasing Reynolds numbers, high velocity zones dominate over low velocity zones.

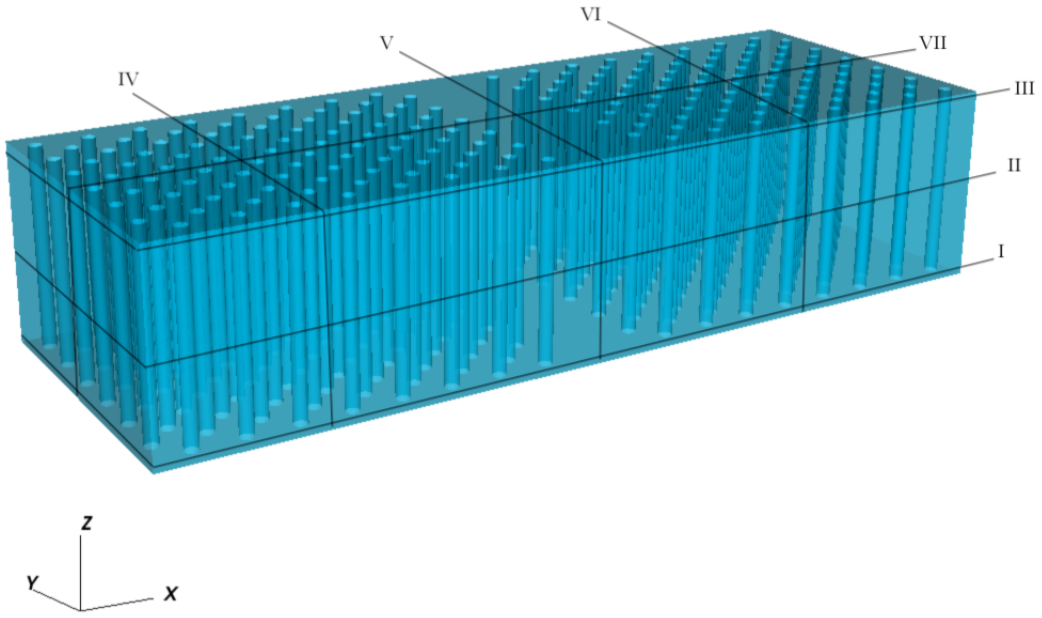

Figure 3.1: Various cross-sections of the channel for investigating flow characteristics along different channel sections

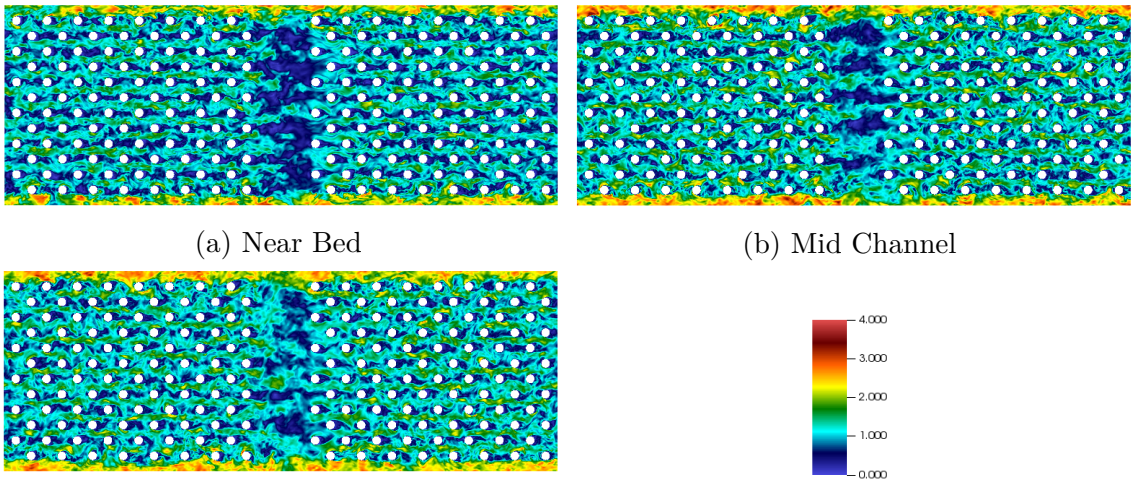

(a) Near Bed

(b) Mid Channel

(c) Near Surface

Figure 3.2: Instantaneous velocity plots for $Re_b = 12000$

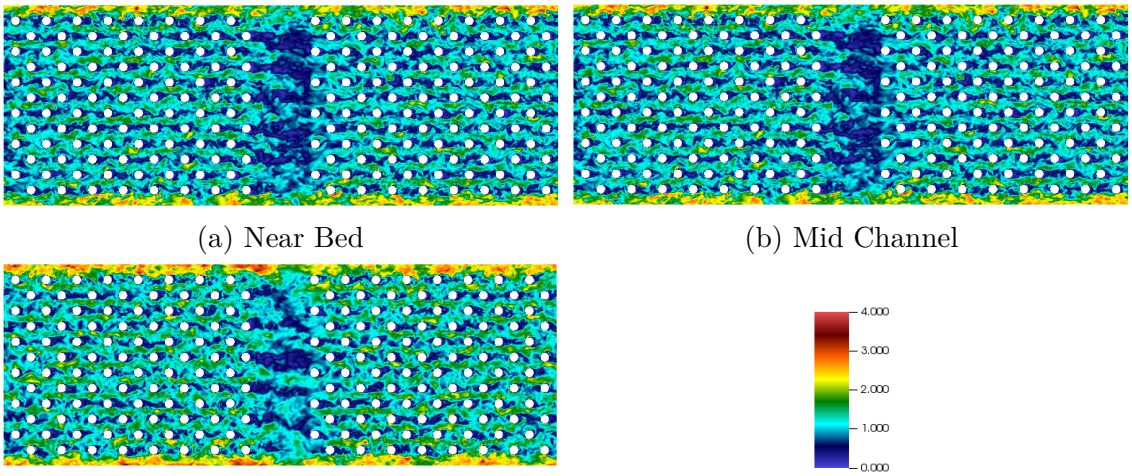

(a) Near Bed

(b) Mid Channel

(c) Near Surface

Figure 3.3: Instantaneous velocity plots for $Re_b = 15000$

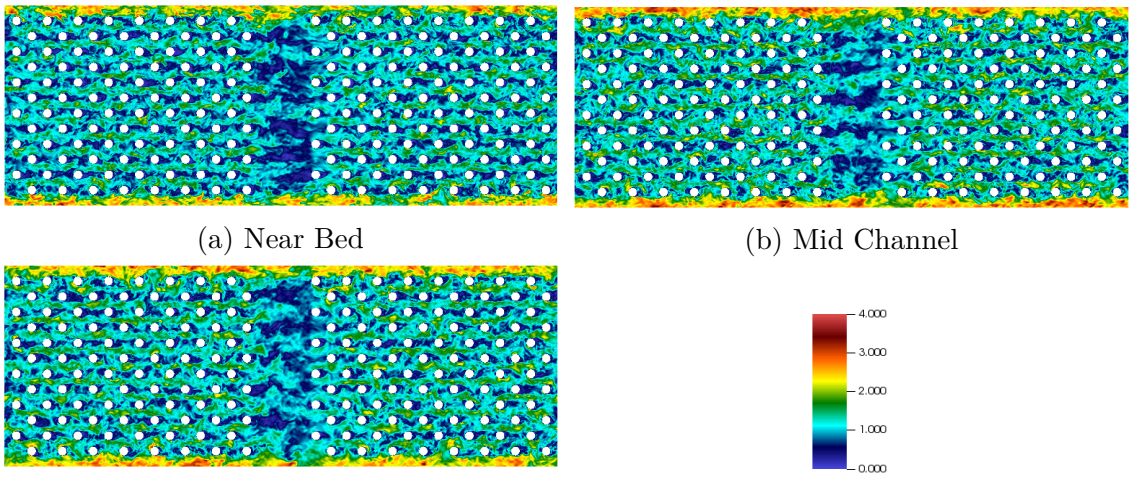

(a) Near Bed

(b) Mid Channel

(c) Near Surface

Figure 3.4: Instantaneous velocity plots for $Re_b = 18000$

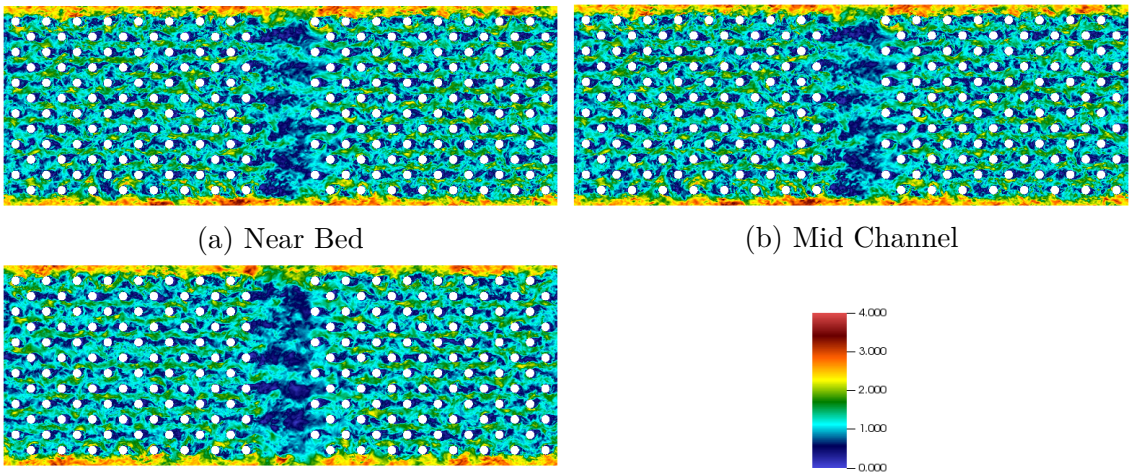

(a) Near Bed

(b) Mid Channel

(c) Near Surface

Figure 3.5: Instantaneous velocity plots for $Re_b = 20000$

3.2 Time Averaged Velocity

Figs. 3.6 - 3.17 show the time averaged velocity field at sections I-VII for increasing Reynolds number of flow. Preferential flow paths develop between two adjacent rows and dominant low velocity zones behind the wakes individual cylinders can be clearly seen for all the cases. The preferential flow paths and low velocity zones downstream of the cylinders is further visible from sections along the length of the channel. Higher velocities at the ends of the channel are a result of periodic boundary conditions in the lateral direction, which allows a wider gap than between adjacent cylinders, forming a preferential path for the flow. Further, for higher flow Reynolds number, the low velocity zones shrink while higher velocities dominate the flow. An objective of this study was to validate if measurements made in the intermediate gap are representative of the flow characteristics within the vegetation patch. It can be seen that the intermediate gap is dominantly a low velocity zone, which is expected as it lies in wake of the vegetation patch, however, it does not appear to be representative of the flow conditions within the patch as is evident from the section along channel width.

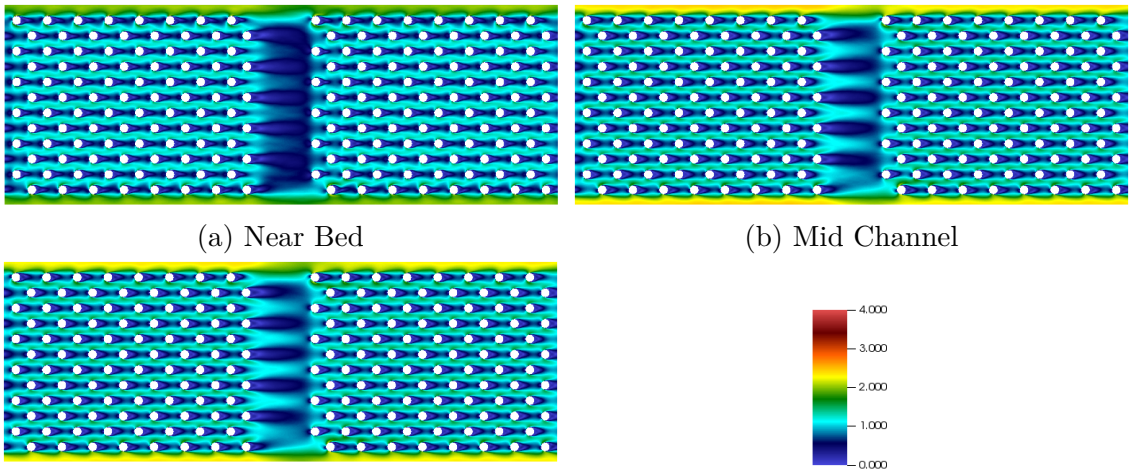

(a) Near Bed

(b) Mid Channel

(c) Near Surface

Figure 3.6: Time averaged velocity plots for $Re_b = 12000$ at sections I, II & III

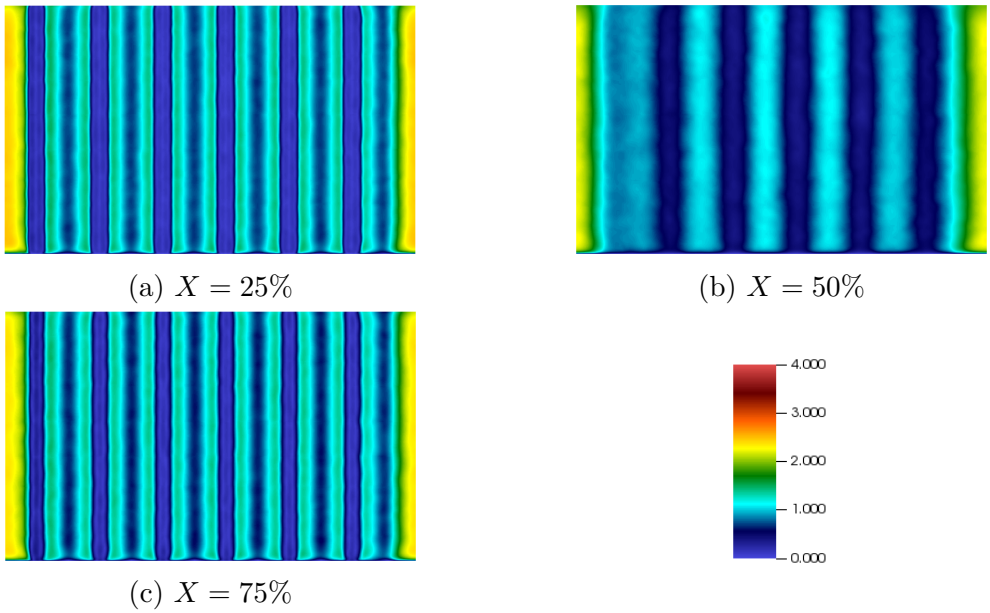

(a) $X = 25\%$

(b) $X = 50\%$

(c) $X = 75\%$

Figure 3.7: Time averaged velocity plots for $Re_b = 12000$ at sections IV, V & VI

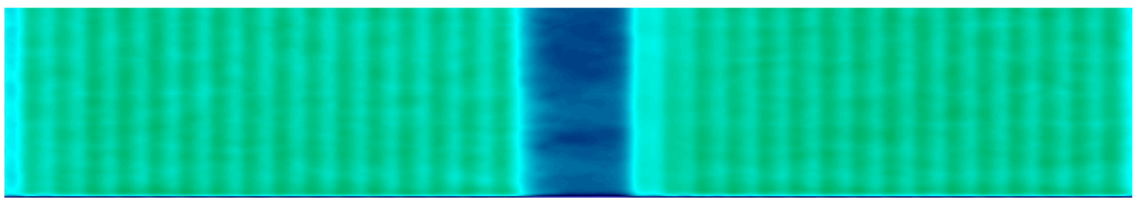

Figure 3.8: Time averaged velocity plot for $Re_b = 12000$ at section VII ($Y = 50\%$)

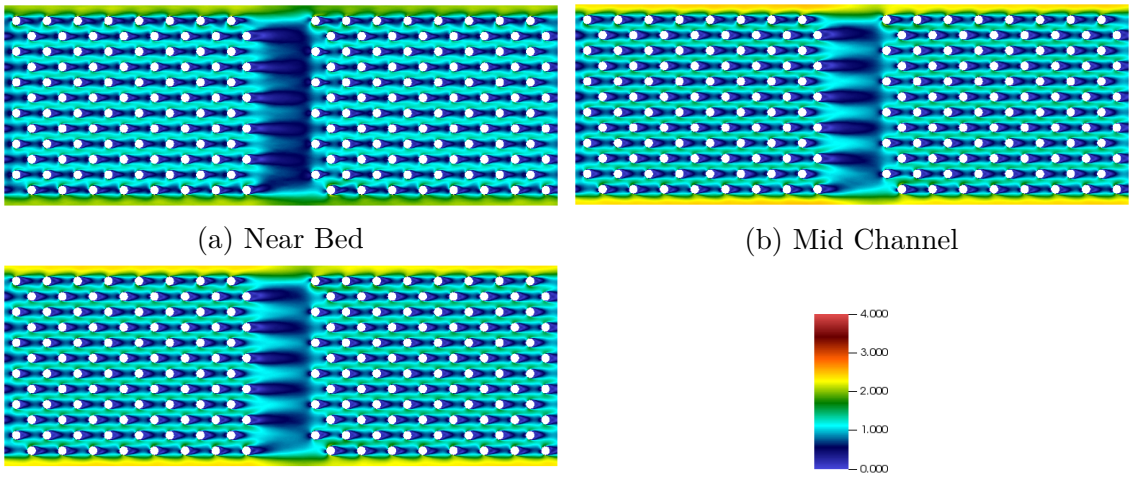

(a) Near Bed

(b) Mid Channel

(c) Near Surface

Figure 3.9: Time averaged velocity plots for $Re_b = 15000$ at sections I, II & III

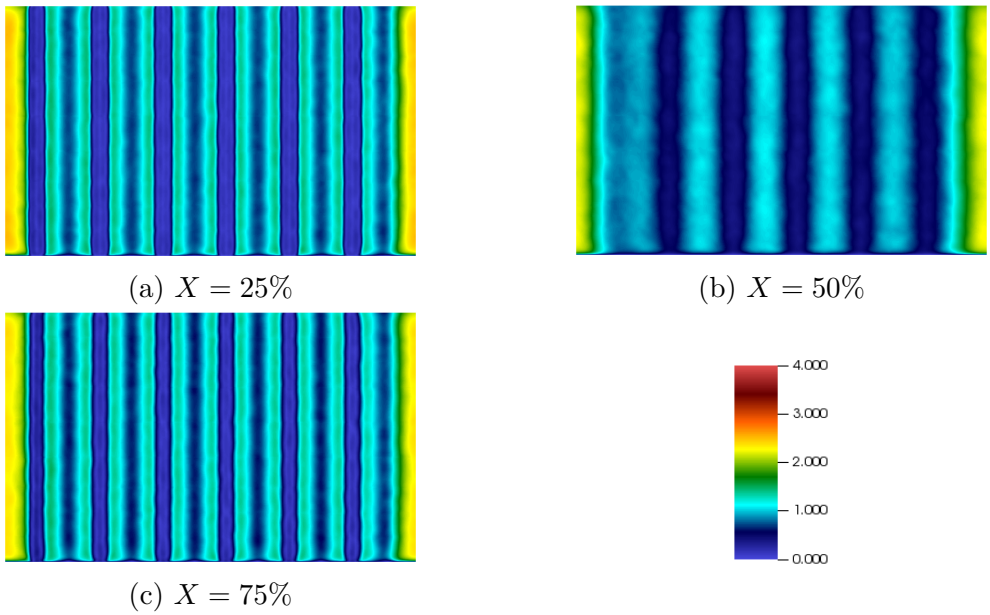

(a) $X = 25\%$

(b) $X = 50\%$

(c) $X = 75\%$

Figure 3.10: Time averaged velocity plots for $Re_b = 15000$ at sections IV, V & VI

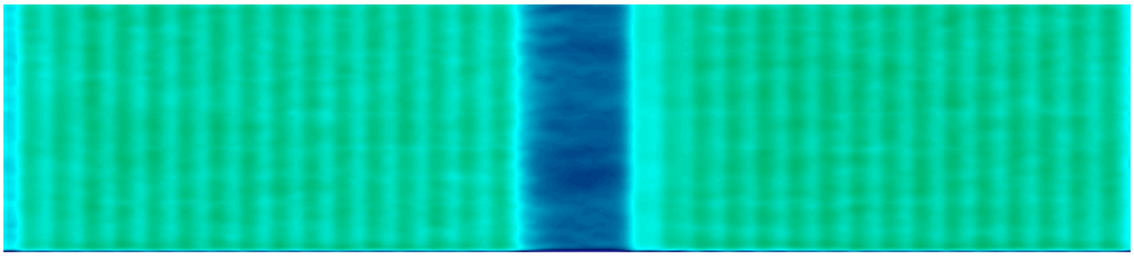

Figure 3.11: Time averaged velocity plot for $Re_b = 15000$ at section VII ($Y = 50\%$)

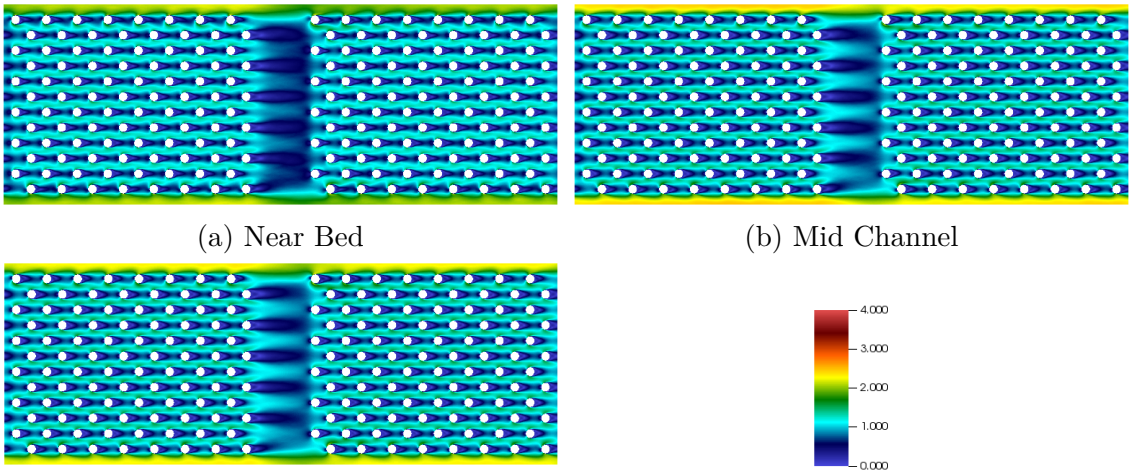

(a) Near Bed

(b) Mid Channel

(c) Near Surface

Figure 3.12: Time averaged velocity plots for $Re_b = 18000$ at sections I, II & III

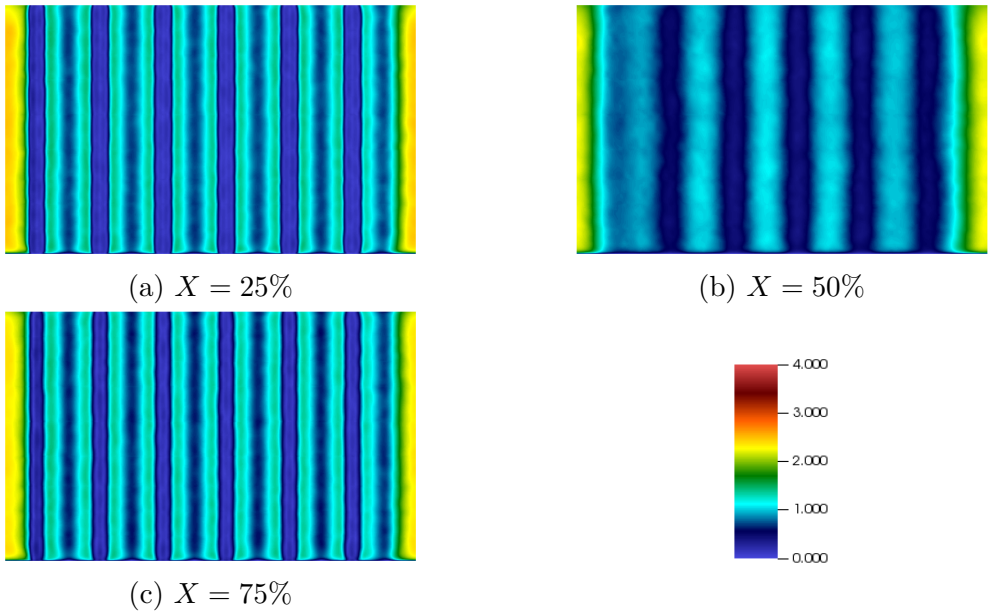

(a) $X = 25\%$

(b) $X = 50\%$

(c) $X = 75\%$

Figure 3.13: Time averaged velocity plots for $Re_b = 18000$ at sections IV, V & VI

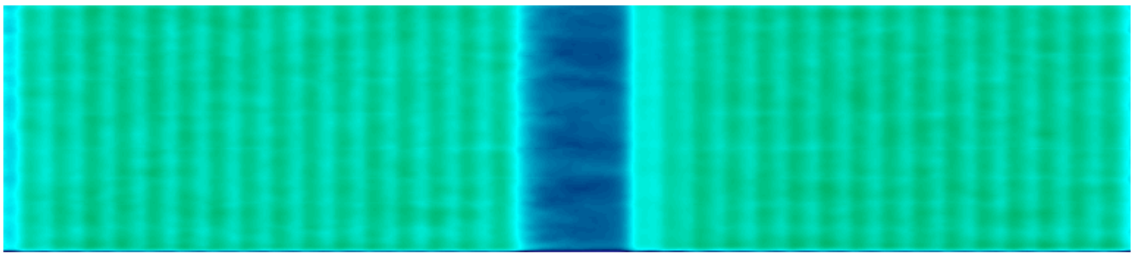

Figure 3.14: Time averaged velocity plot for $Re_b = 18000$ at section VII ($Y = 50\%$)

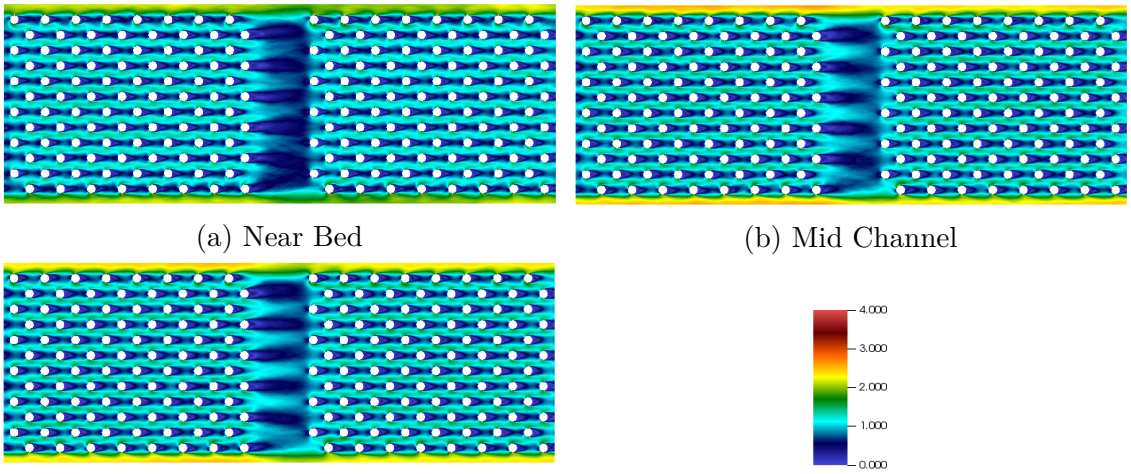

(a) Near Bed

(b) Mid Channel

(c) Near Surface

Figure 3.15: Time averaged velocity plots for $Re_b = 20000$ at sections I, II & III

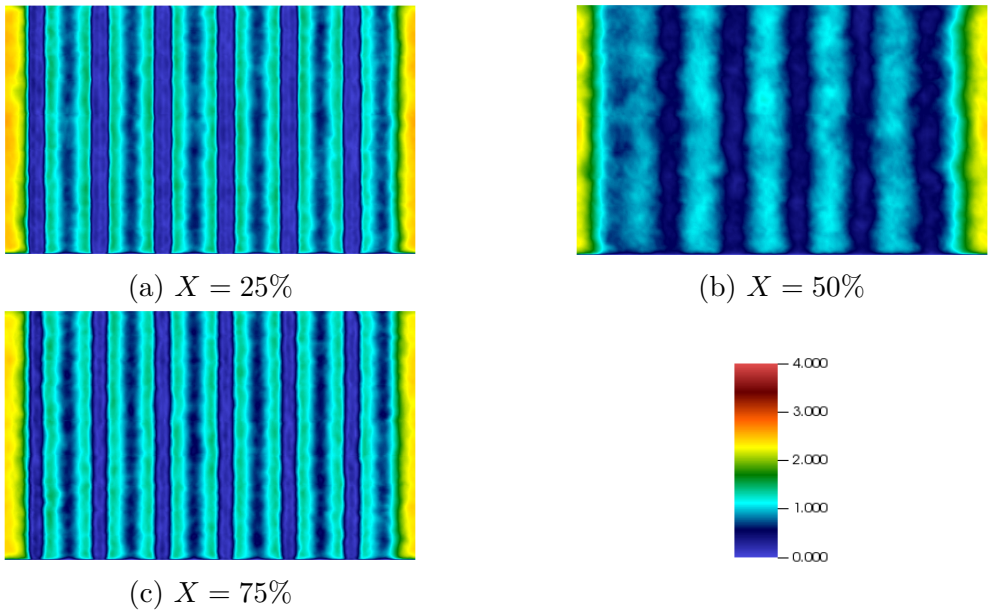

(a) $X = 25\%$

(b) $X = 50\%$

(c) $X = 75\%$

Figure 3.16: Time averaged velocity plots for $Re_b = 20000$ at sections IV, V & VI

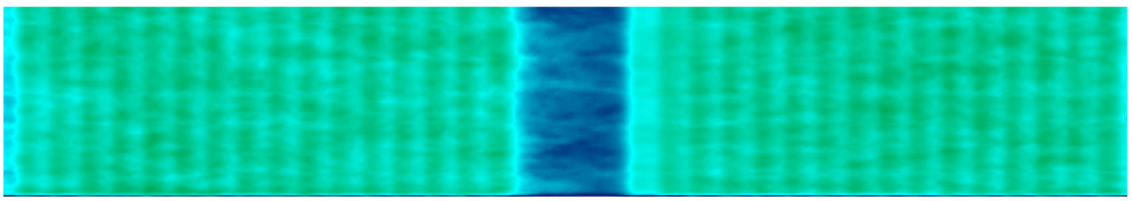

Figure 3.17: Time averaged velocity plot for $Re_b = 20000$ at section VII ($Y = 50\%$)

3.3 Turbulent Kinetic Energy

Turbulent Kinetic Energy (TKE), k in a turbulent flow refers to the kinetic energy per unit mass of the turbulent fluctuations, u_i'.

$$k = \frac{1}{2}\overline{u_i' u_i'} = \frac{1}{2}\left(u_x'^2 + u_y'^2 + u_z'^2\right) \tag{3.1}$$

Fig. 3.18-3.29 show the Turbulent Kinetic Energy (TKE) at sections I-VII for increasing Reynolds number of the flow. It can be observed that TKE increases moving up along the depth of the channel. TKE in the wake of the cylinders is high as it contributes the most towards velocity fluctuations as a result of vortex shedding in the wake, which is also validated from the plots of TKE across cross-sections along the channel length, where the stems can be seen contributing the most towards turbulence. Also, the TKE in the intermediate gap is predominantly negligible across all cases, which again suggest that the gap is not representative of turbulence characteristics within the vegetation patch. Higher TKE along the edge of the canopy is due to formation of a shear layer in the wider gap as a result of periodicity of the domain. Otherwise, the overall pattern of TKE is consistent across the domain and increases for higher Reynolds number.

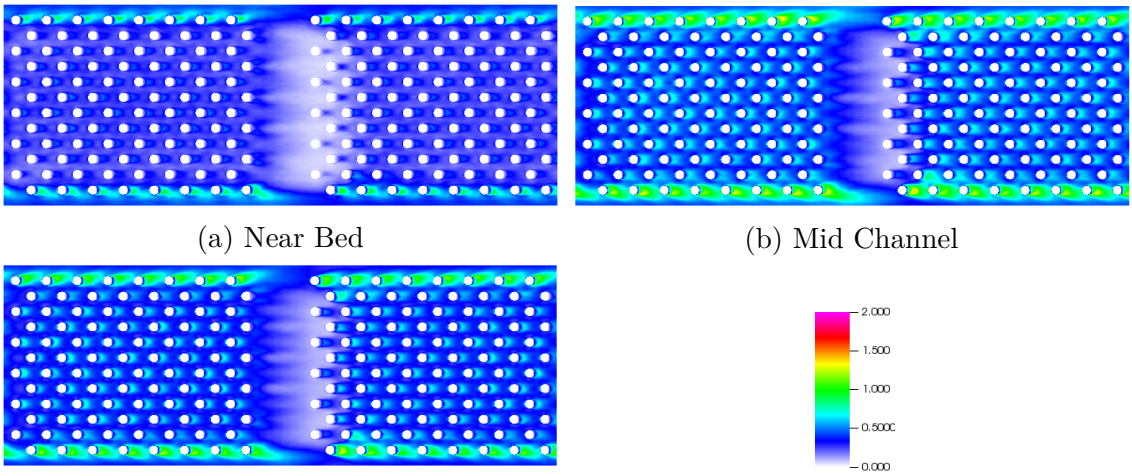

(a) Near Bed

(b) Mid Channel

(c) Near Surface

Figure 3.18: TKE plots for $Re_b = 12000$ at sections I, II & III

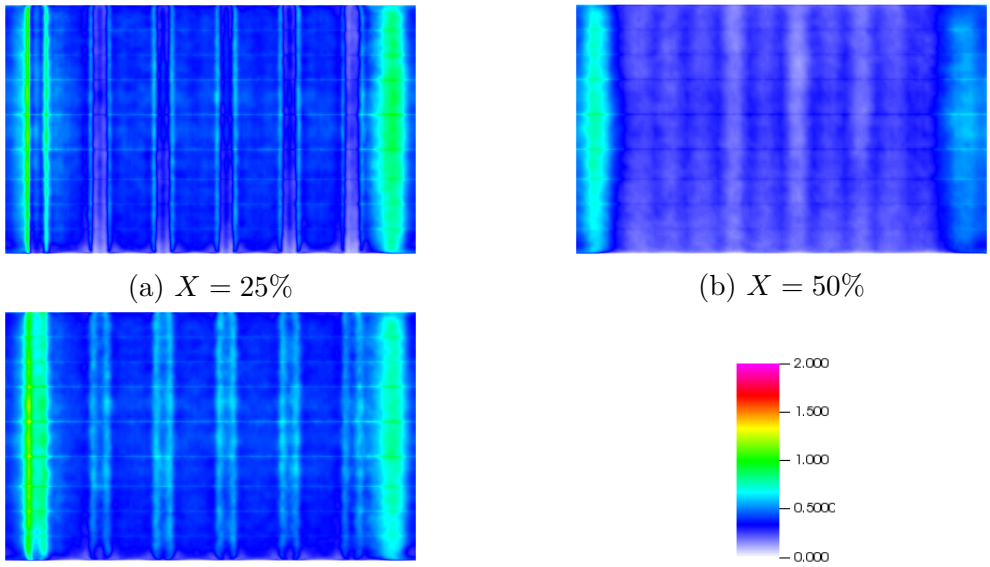

(a) $X = 25\%$

(b) $X = 50\%$

(c) $X = 75\%$

Figure 3.19: TKE plots for $Re_b = 12000$ at sections IV, V & VI

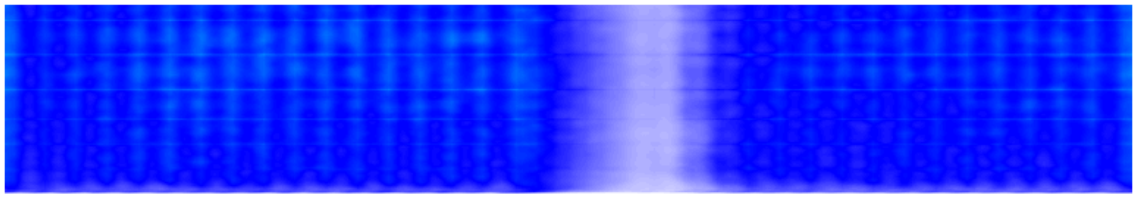

Figure 3.20: TKE plot for $Re_b = 12000$ at section VII ($Y = 50\%$)

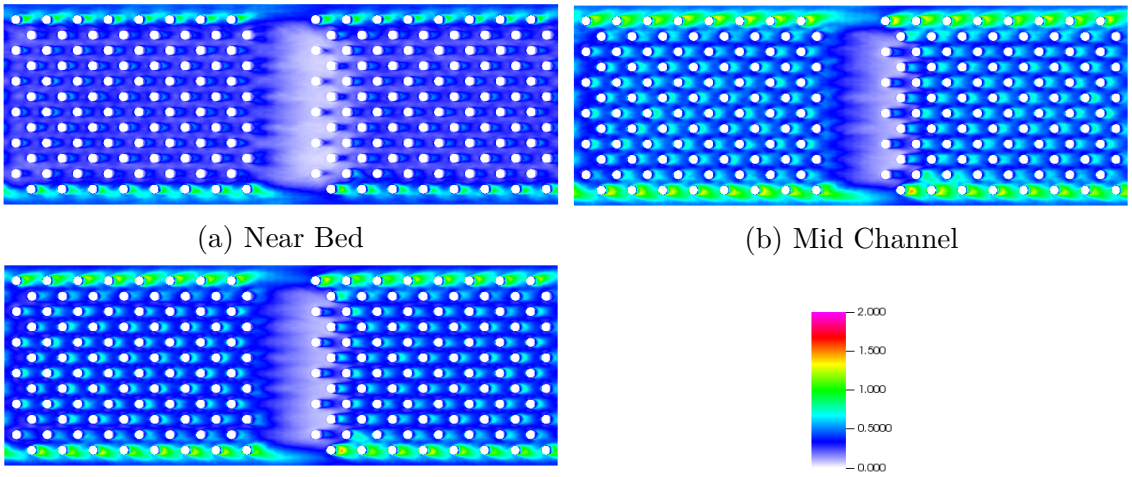

(a) Near Bed

(b) Mid Channel

(c) Near Surface

Figure 3.21: TKE plots for $Re_b = 15000$ at sections I, II & III

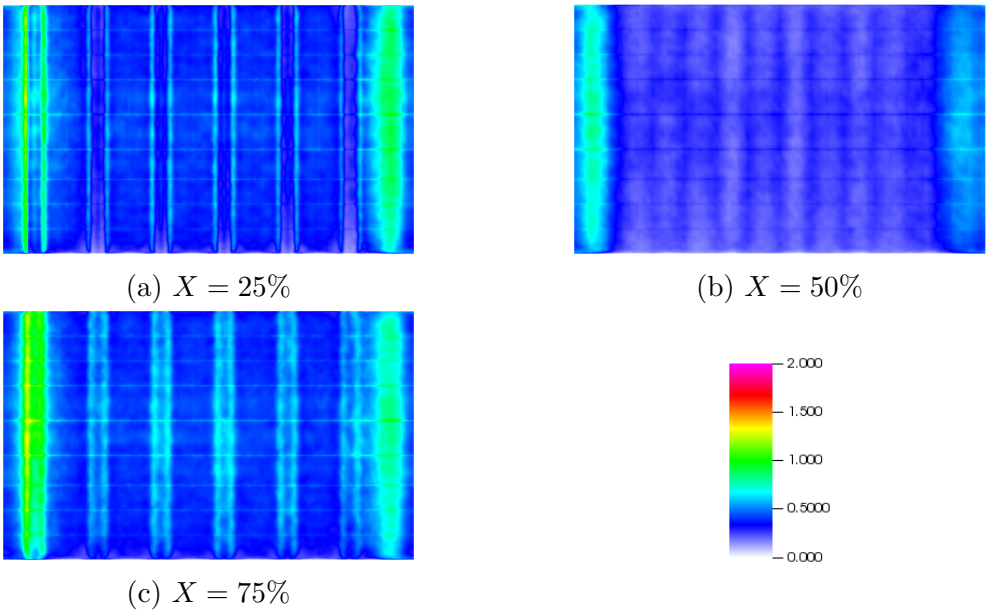

(a) $X = 25\%$

(b) $X = 50\%$

(c) $X = 75\%$

Figure 3.22: TKE plots for $Re_b = 15000$ at sections IV, V & VI

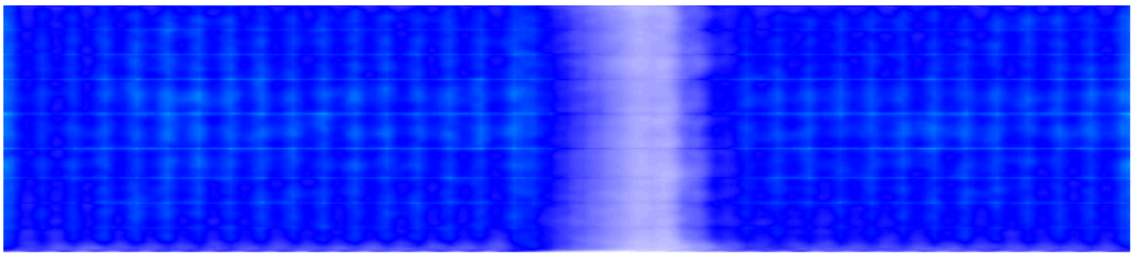

Figure 3.23: TKE plot for $Re_b = 15000$ at section VII ($Y = 50\%$)

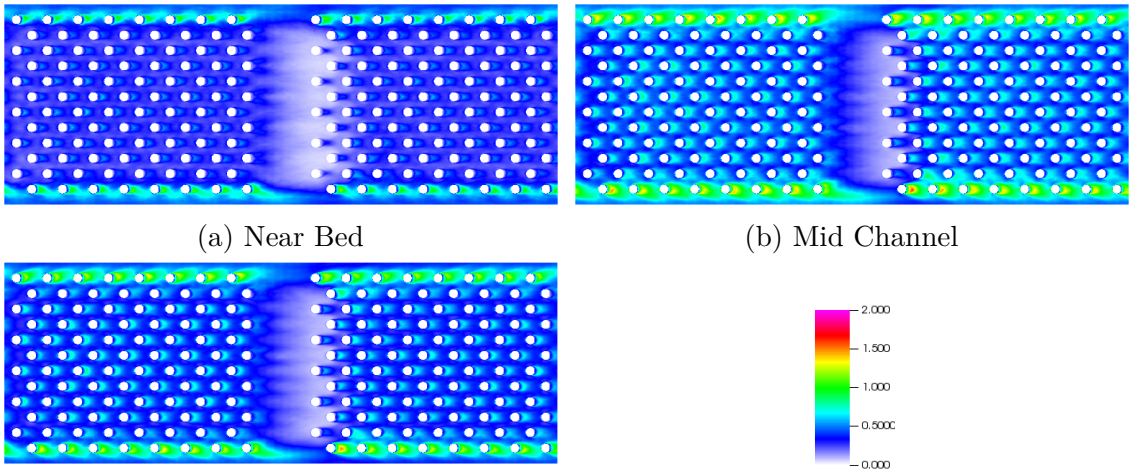

(a) Near Bed

(b) Mid Channel

(c) Near Surface

Figure 3.24: TKE plots for $Re_b = 18000$ at sections I, II & III

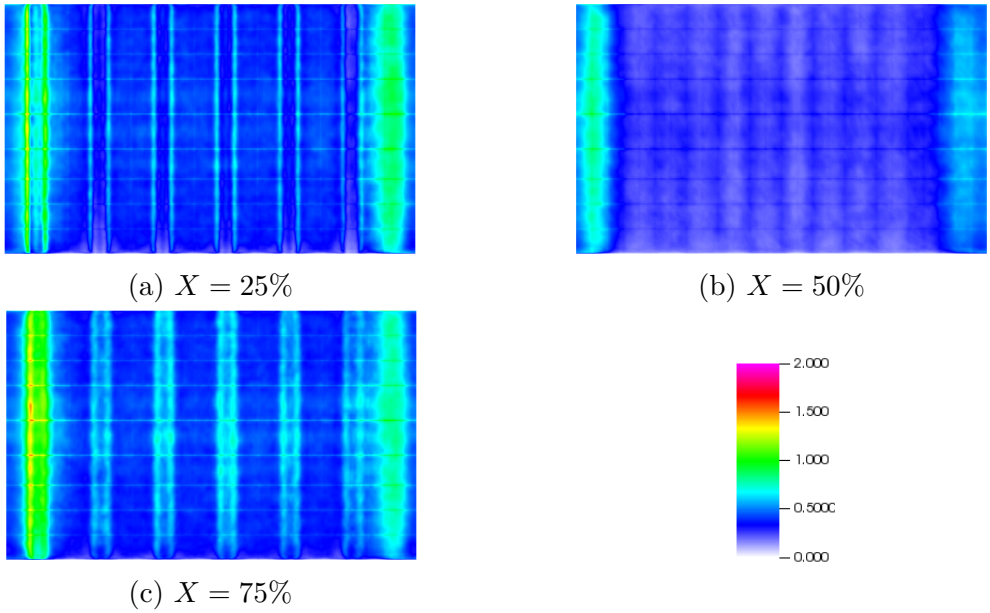

(a) $X = 25\%$

(b) $X = 50\%$

(c) $X = 75\%$

Figure 3.25: TKE plots for $Re_b = 18000$ at sections IV, V & VI

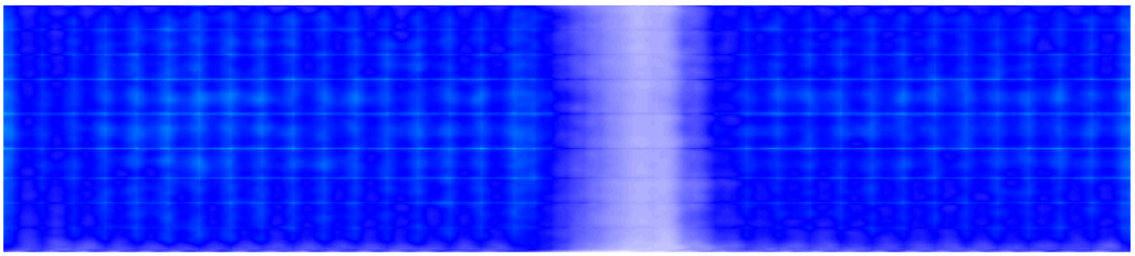

Figure 3.26: TKE plot for $Re_b = 18000$ at section VII ($Y = 50\%$)

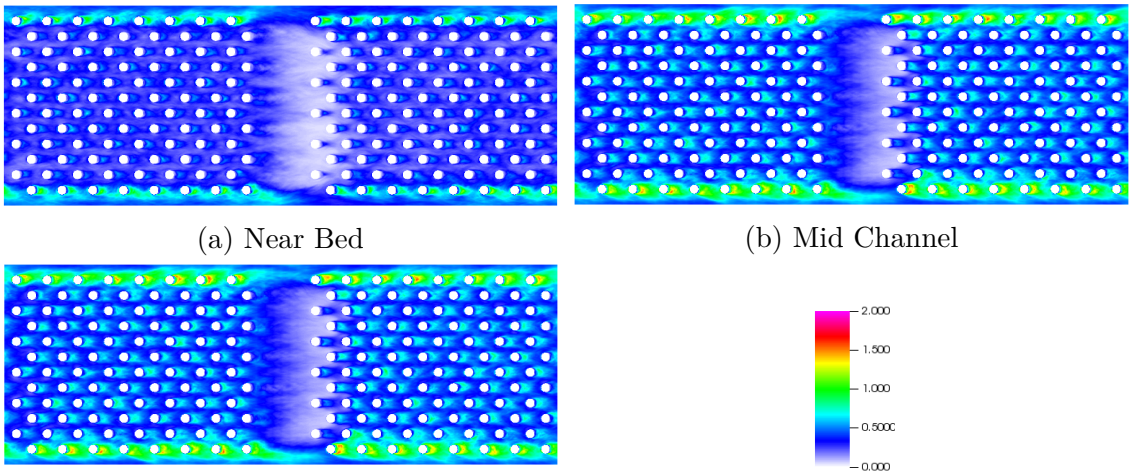

(a) Near Bed

(b) Mid Channel

(c) Near Surface

Figure 3.27: TKE plots for $Re_b = 20000$ at sections I, II & III

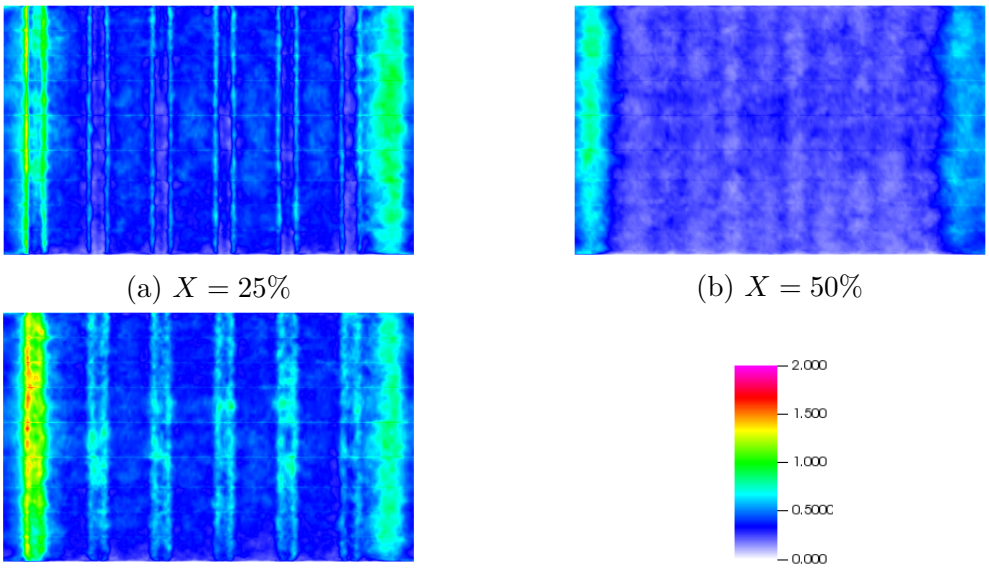

(a) $X = 25\%$

(b) $X = 50\%$

(c) $X = 75\%$

Figure 3.28: TKE plots for $Re_b = 20000$ at sections IV, V & VI

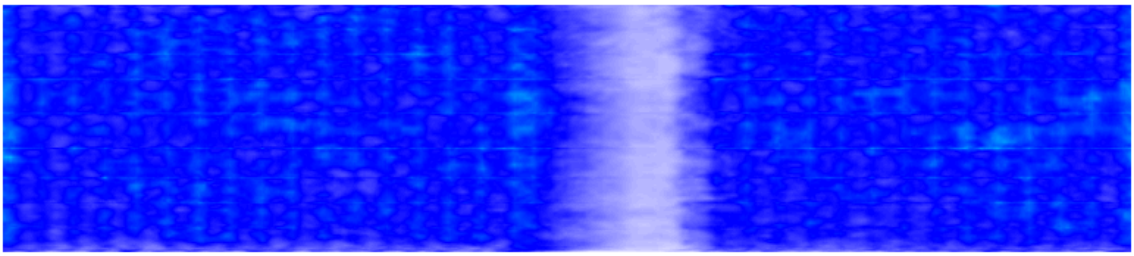

Figure 3.29: TKE plot for $Re_b = 20000$ at section VII ($Y = 50\%$)

3.4 Reynold's Stresses

Reynolds stress is a symmetric tensor representing the transport of mean momentum by turbulent motion. It is given as:

$$\tau_{ij} = \overline{u_i u_j} = \begin{pmatrix} \overline{u_x^2} & \overline{u_x u_y} & \overline{u_x u_z} \\ \overline{u_y u_x} & \overline{u_y^2} & \overline{u_y u_z} \\ \overline{u_z u_x} & \overline{u_z u_y} & \overline{u_z^2} \end{pmatrix} \tag{3.2}$$

The diagonal components of $\tau_{ij} = \overline{u_{ii}}$ represent the normal stresses and contribute less to the transport of mean momentum. It is the work done by the off diagonal shear stresses, $\overline{u_{ij}}$ which contributes to the transport of mean momentum. Fig. 3.30-3.41 show the dominant Reynold's stress, $\overline{u'w'}$ at the seven cross-sections. A clear pattern emerges, as moving downstream the Reynolds stress is negative to the left of cylinders and positive to the right. Also, the Reynolds stress pattern is constricted by interactions with the surrounding cylinders within the patch, but it fully develops in the gap. This has implications in transport of bed sediment by the flow as near bed Reynolds stress values govern scouring around the cylinders. Again, the gap is non representative of the conditions within the vegetation patch.

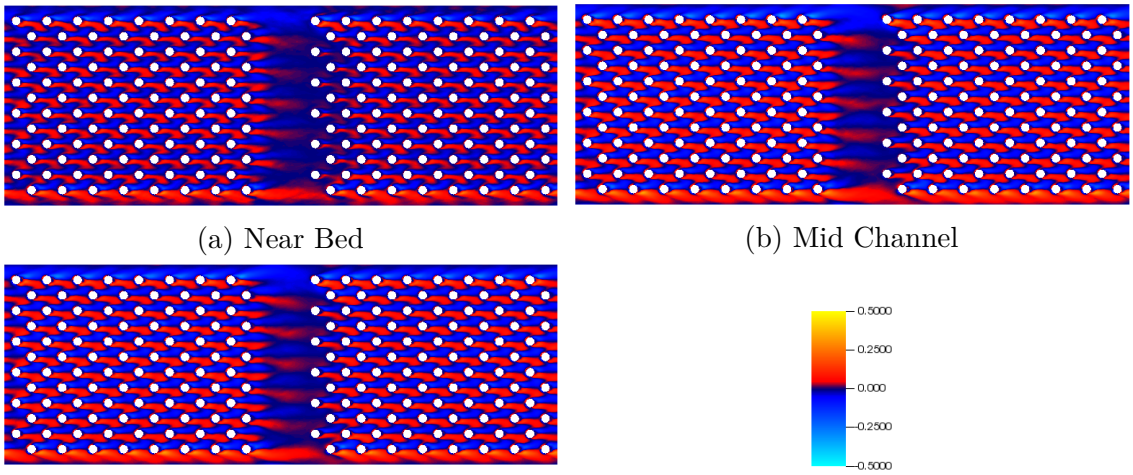

(a) Near Bed

(b) Mid Channel

(c) Near Surface

Figure 3.30: $\overline{u'w'}$ plots for $Re_b = 12000$ at sections I, II & III

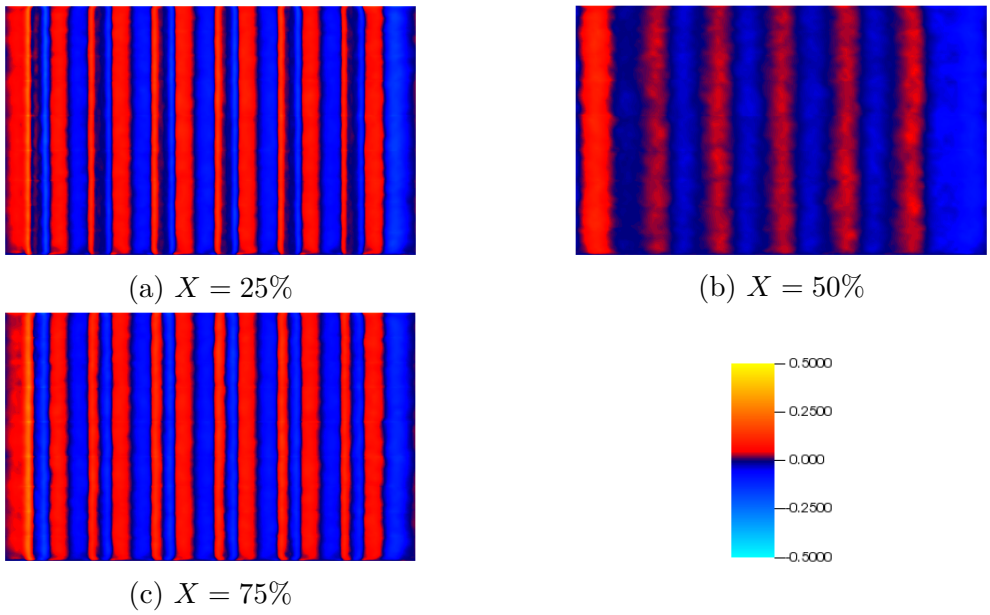

(a) $X = 25\%$

(b) $X = 50\%$

(c) $X = 75\%$

Figure 3.31: $\overline{u'w'}$ plots for $Re_b = 12000$ at sections IV, V & VI

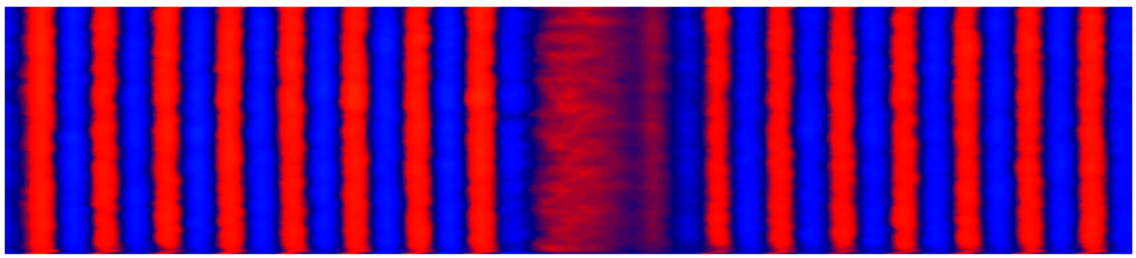

Figure 3.32: $\overline{u'w'}$ plot for $Re_b = 12000$ at section VII ($Y = 50\%$)

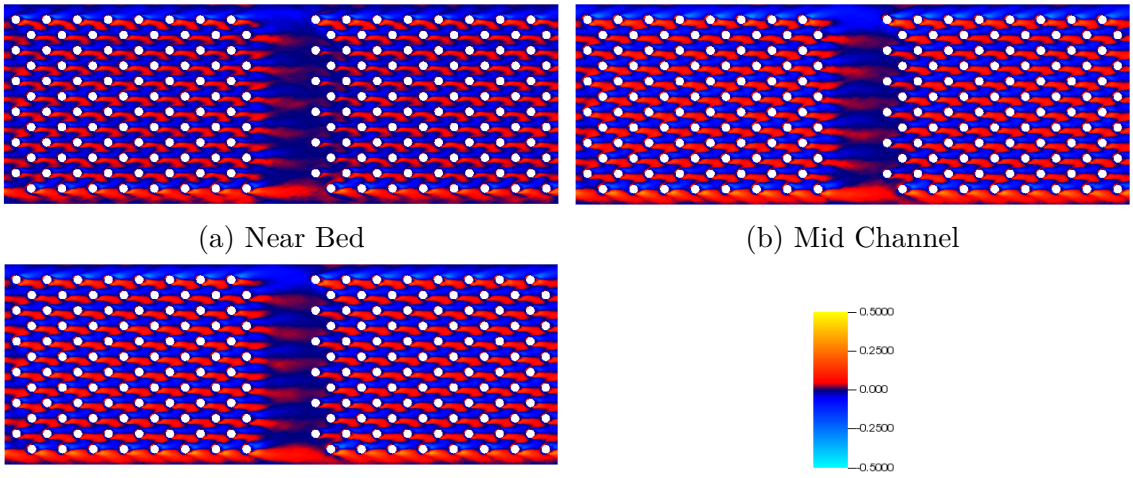

(a) Near Bed

(b) Mid Channel

(c) Near Surface

Figure 3.33: $\overline{u'w'}$ plots for $Re_b = 15000$ at sections I, II & III

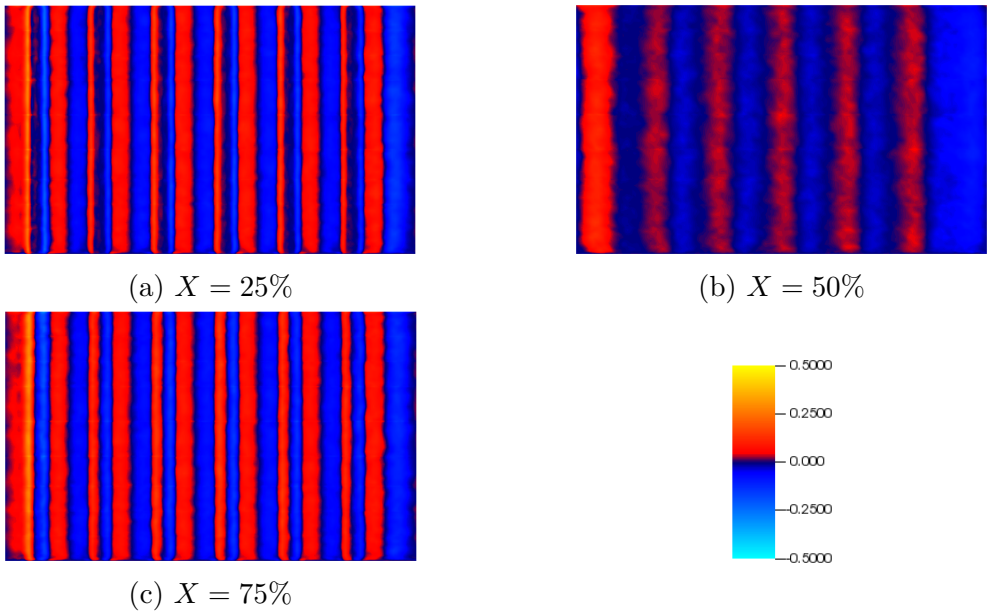

(a) $X = 25\%$

(b) $X = 50\%$

(c) $X = 75\%$

Figure 3.34: $\overline{u'w'}$ plots for $Re_b = 15000$ at sections IV, V & VI

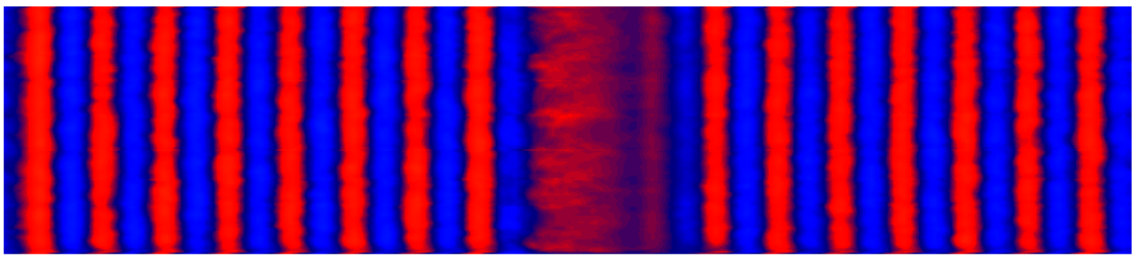

Figure 3.35: $\overline{u'w'}$ plot for $Re_b = 15000$ at section VII ($Y = 50\%$)

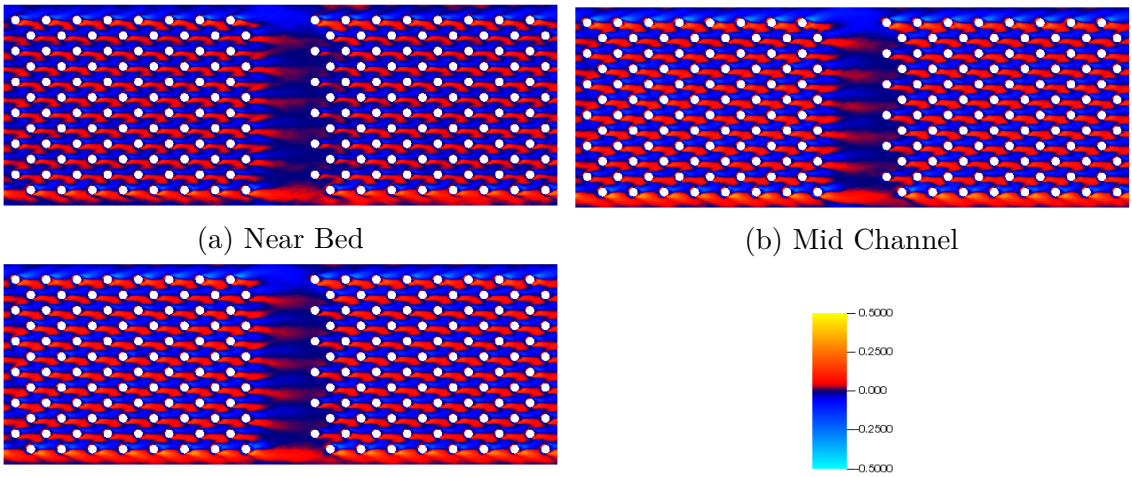

(a) Near Bed

(b) Mid Channel

(c) Near Surface

Figure 3.36: $\overline{u'w'}$ plots for $Re_b = 18000$ at sections I, II & III

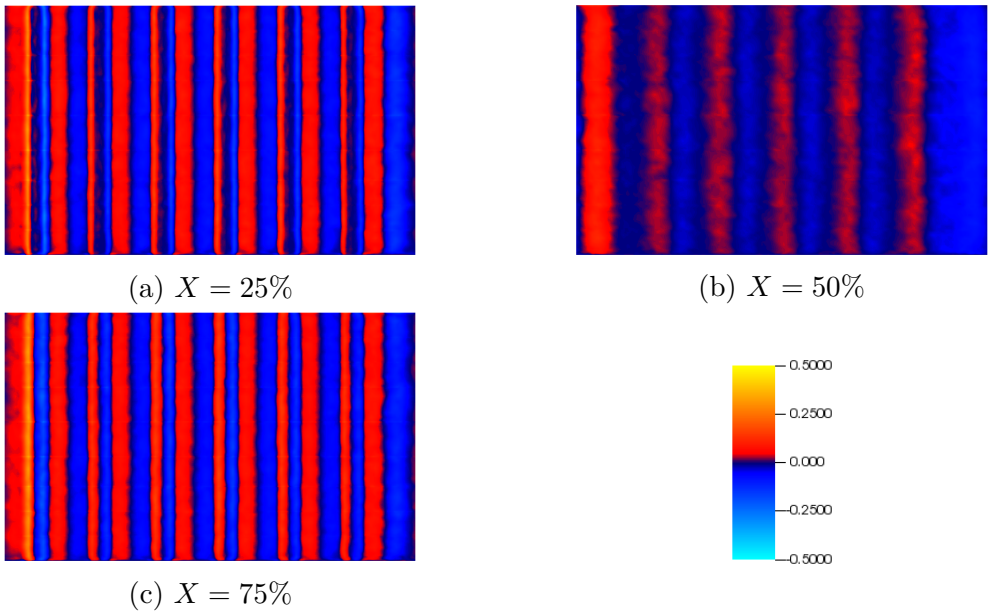

(a) $X = 25\%$

(b) $X = 50\%$

(c) $X = 75\%$

Figure 3.37: $\overline{u'w'}$ plots for $Re_b = 18000$ at sections IV, V & VI

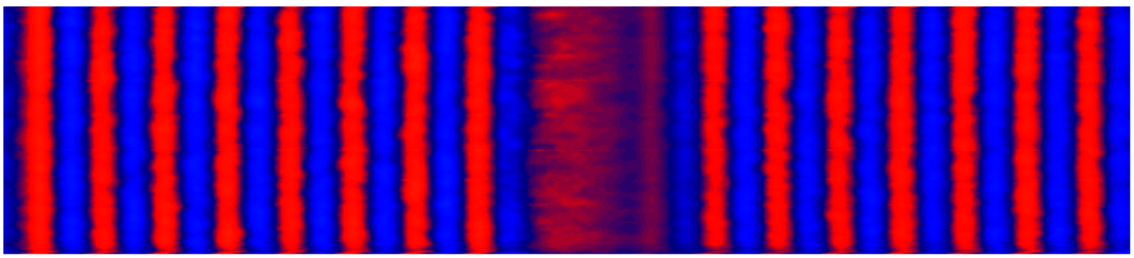

Figure 3.38: $\overline{u'w'}$ plot for $Re_b = 18000$ at section VII ($Y = 50\%$)

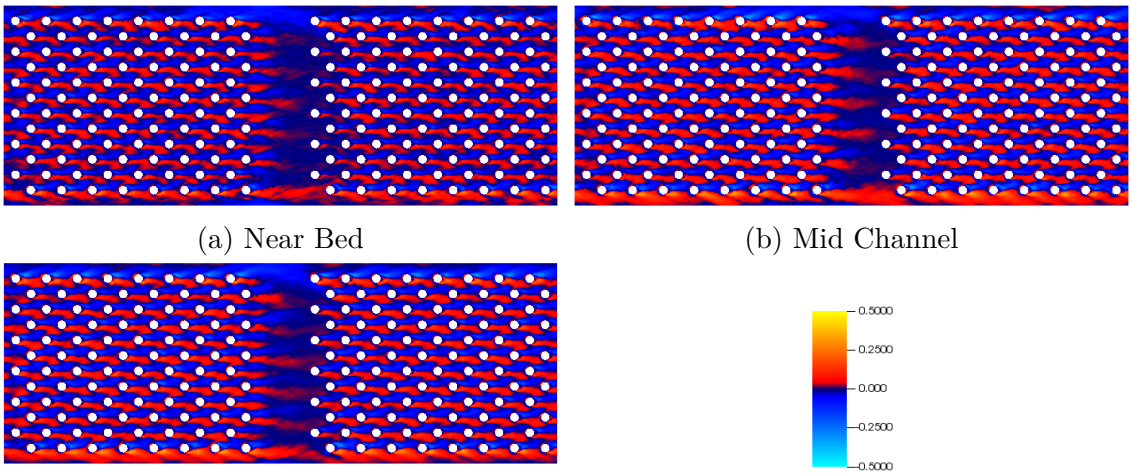

(a) Near Bed

(b) Mid Channel

(c) Near Surface

Figure 3.39: $\overline{u'w'}$ plots for $Re_b = 20000$ at sections I, II & III

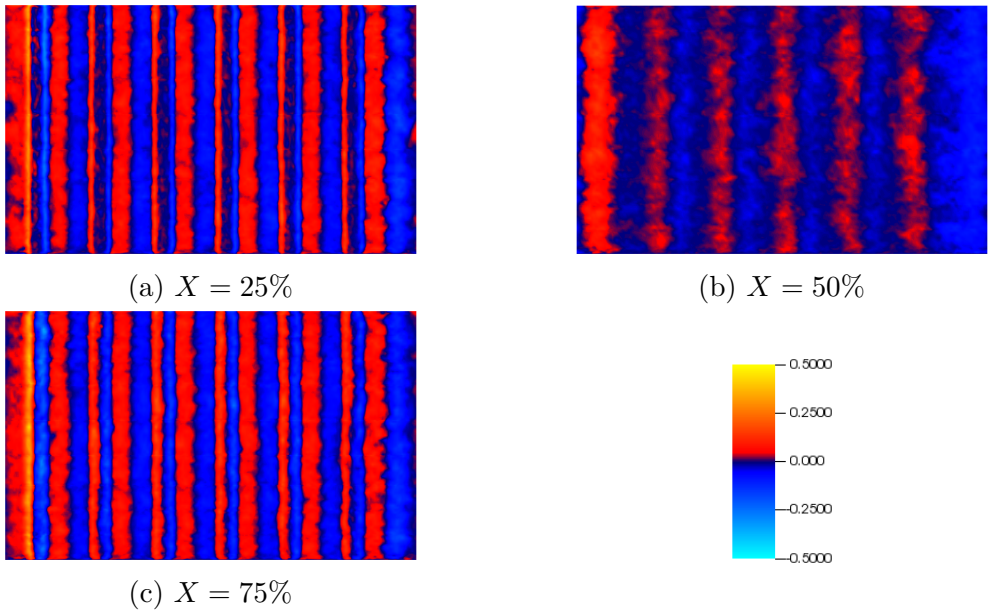

(a) $X = 25\%$

(b) $X = 50\%$

(c) $X = 75\%$

Figure 3.40: $\overline{u'w'}$ plots for $Re_b = 20000$ at sections IV, V & VI

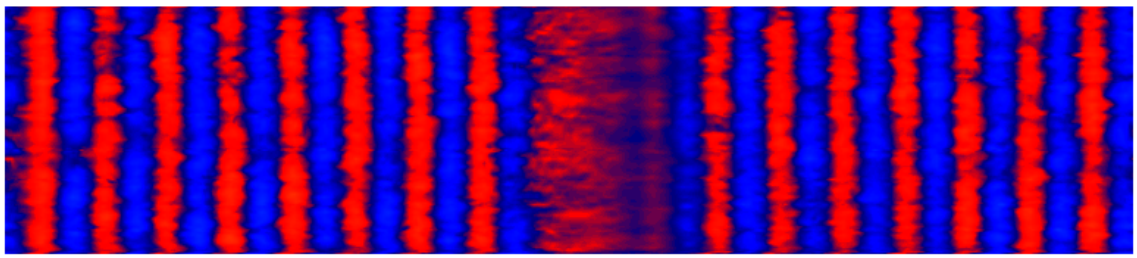

Figure 3.41: $\overline{u'w'}$ plot for $Re_b = 20000$ at section VII ($Y = 50\%$)

3.5 Turbulence Intensity

Turbulence intensity, I is the measure of level of turbulence in the flow. It is defined as the ratio of root mean square fluctuations to the mean velocity of flow.

$$I = \frac{u'_{rms}}{U} \tag{3.3}$$

where,

$u'_{rms} = \sqrt{\frac{1}{3}\left(u'^2_x + u'^2_y + u'^2_z\right)} = \sqrt{\frac{2}{3}k}$

$U = \sqrt{U_x^2 + U_y^2 + U_z^2}$

u'_i is the fluctuation, and

U_i is the mean velocity in i direction. Fig. 3.42-3.53 shows the Turbulence Intensity across all the seven cross-sections, expressed as percentage of mean velocity of flow. The patterns are similar to that of TKE, as the stem scale wakes dominate the production of turbulence. The gap is again non representative of the turbulent intensity characteristics within the vegetation patch.

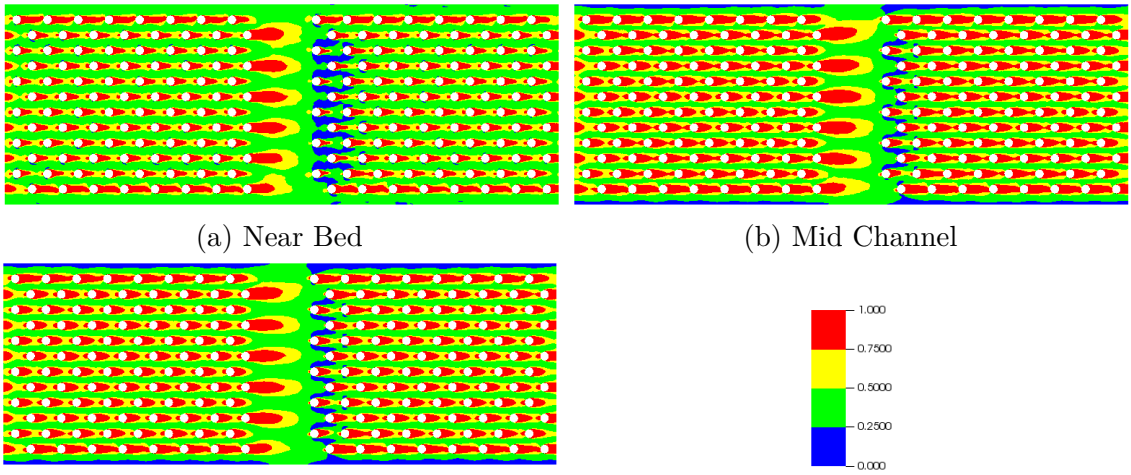

(a) Near Bed

(b) Mid Channel

(c) Near Surface

Figure 3.42: Turbulence Intensity plots for $Re_b = 12000$ at sections I, II & III

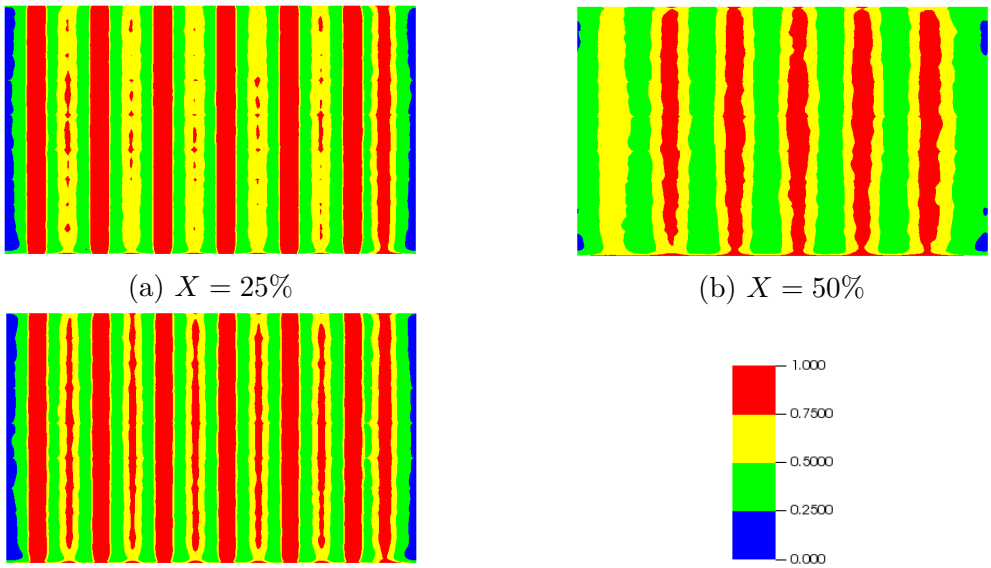

(a) $X = 25\%$

(b) $X = 50\%$

(c) $X = 75\%$

Figure 3.43: Turbulence Intensity plots for $Re_b = 12000$ at sections IV, V & VI

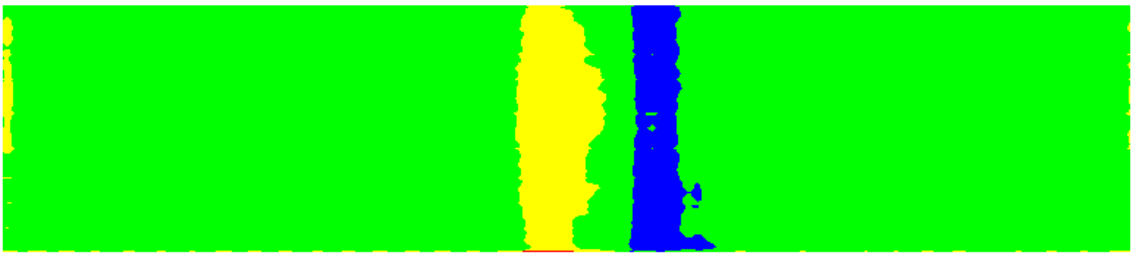

Figure 3.44: Turbulence Intensity plot for $Re_b = 12000$ at section VII ($Y = 50\%$)

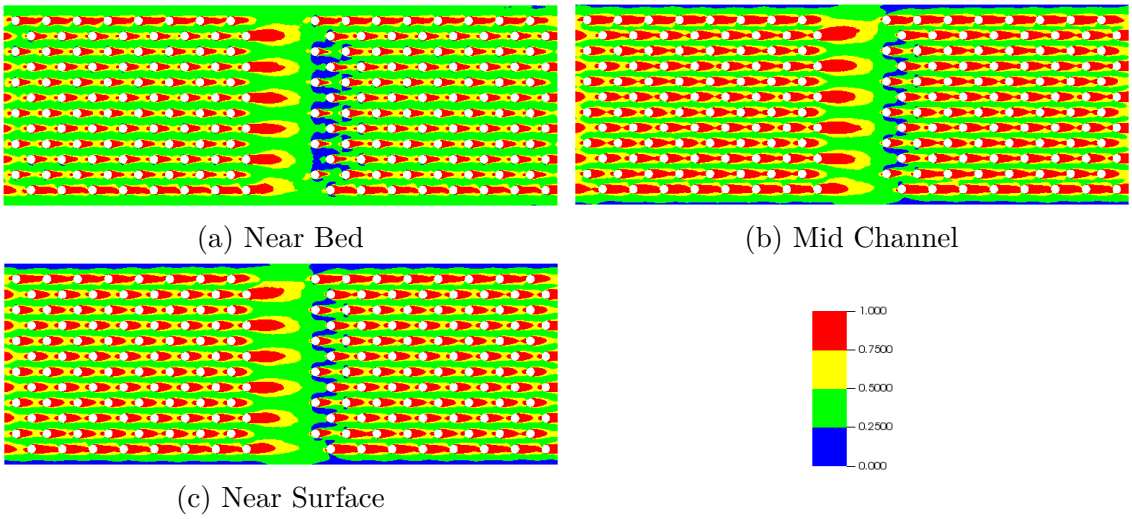

(a) Near Bed

(b) Mid Channel

(c) Near Surface

Figure 3.45: Turbulence Intensity plots for $Re_b = 15000$ at sections I, II & III

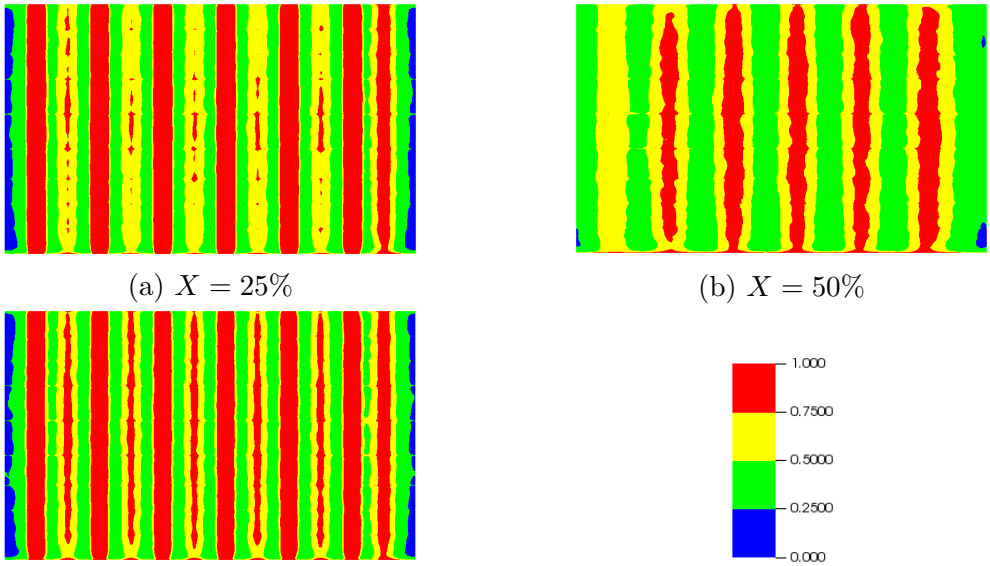

(a) $X = 25\%$

(b) $X = 50\%$

(c) $X = 75\%$

Figure 3.46: Turbulence Intensity plots for $Re_b = 15000$ at sections IV, V & VI

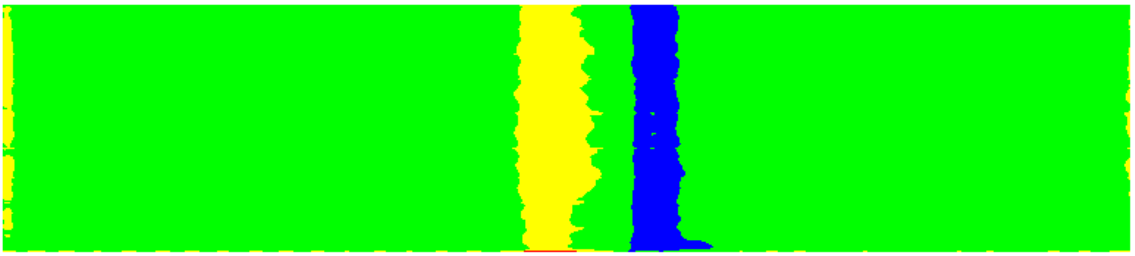

Figure 3.47: Turbulence Intensity plot for $Re_b = 15000$ at section VII ($Y = 50\%$)

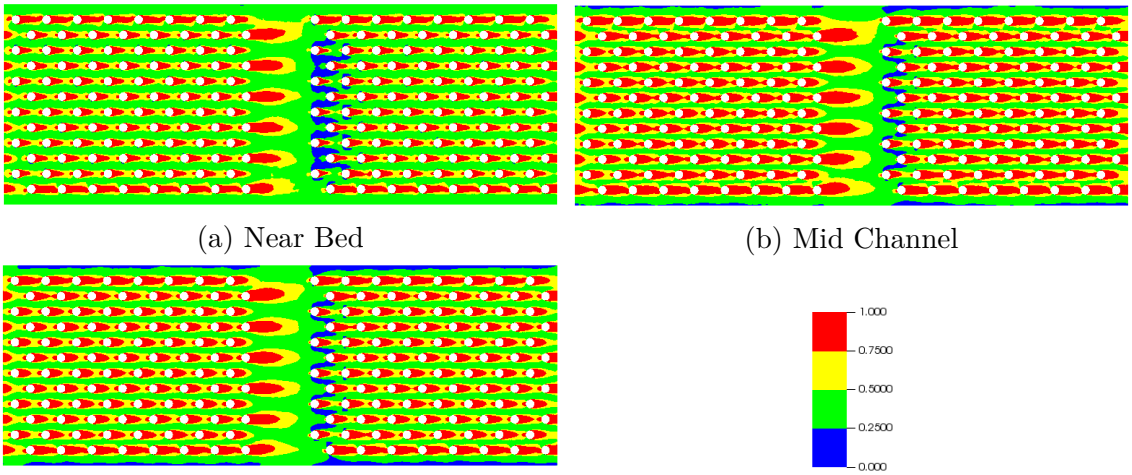

(a) Near Bed

(b) Mid Channel

(c) Near Surface

Figure 3.48: Turbulence Intensity plots for $Re_b = 18000$ at sections I, II & III

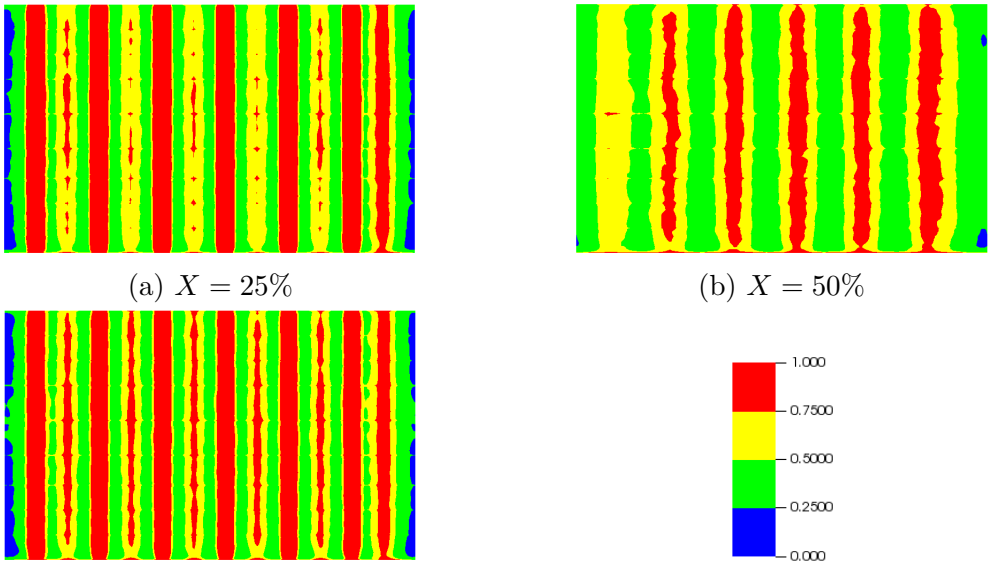

(a) $X = 25\%$

(b) $X = 50\%$

(c) $X = 75\%$

Figure 3.49: Turbulence Intensity plots for $Re_b = 18000$ at sections IV, V & VI

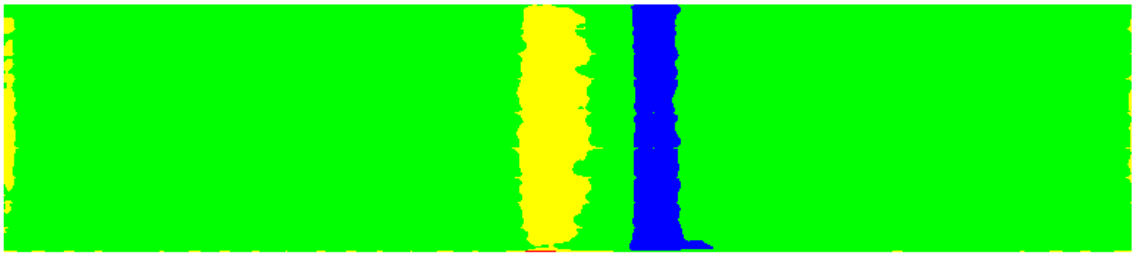

Figure 3.50: Turbulence Intensity plot for $Re_b = 18000$ at section VII ($Y = 50\%$)

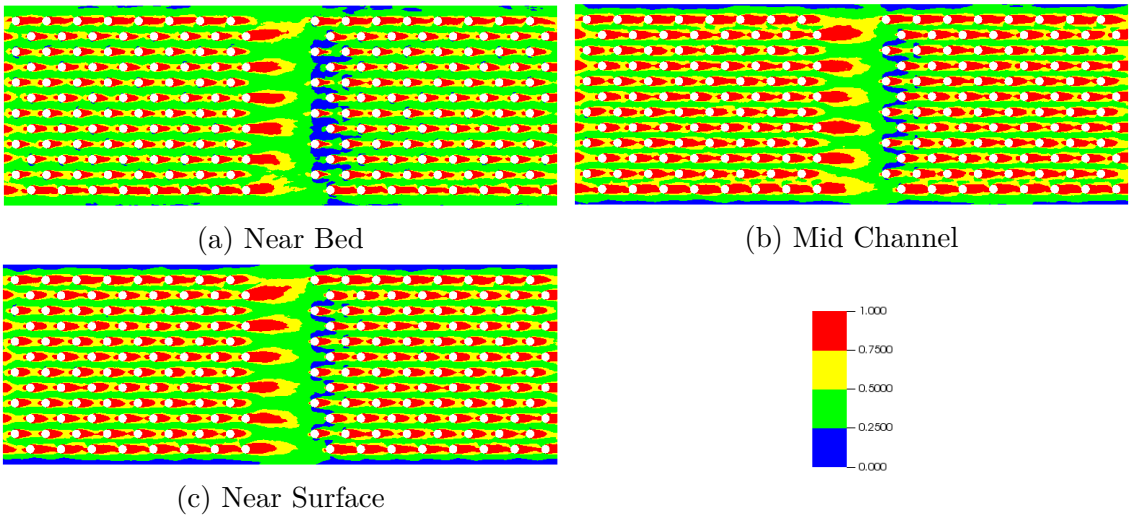

(a) Near Bed

(b) Mid Channel

(c) Near Surface

Figure 3.51: Turbulence Intensity plots for $Re_b = 20000$ at sections I, II & III

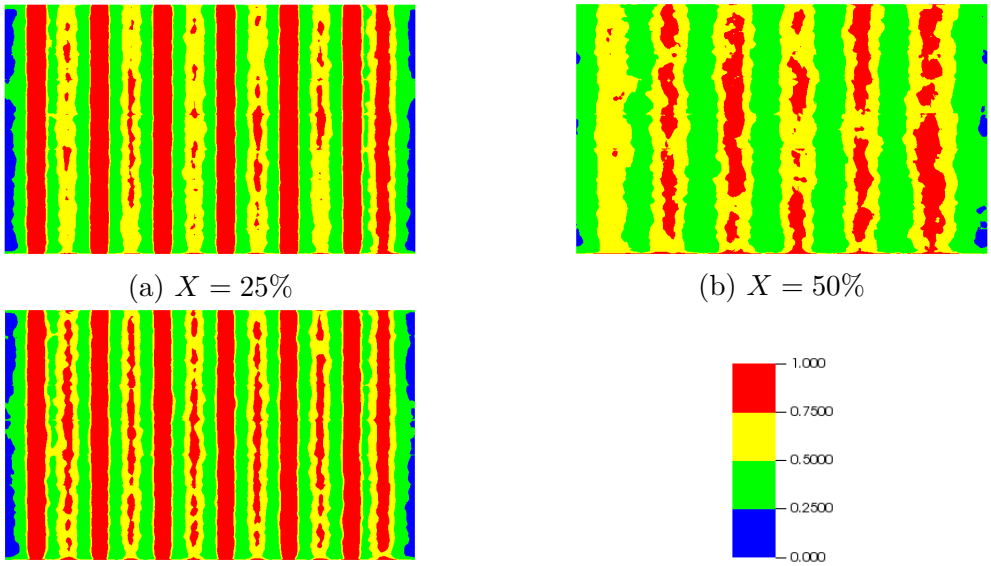

(a) $X = 25\%$

(b) $X = 50\%$

(c) $X = 75\%$

Figure 3.52: Turbulence Intensity plots for $Re_b = 20000$ at sections IV, V & VI

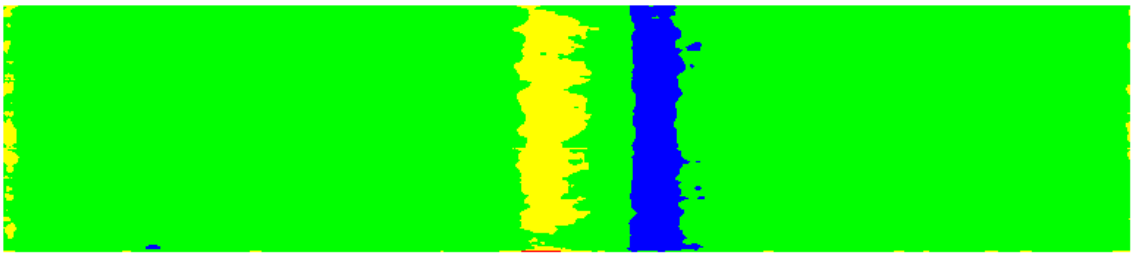

Figure 3.53: Turbulence Intensity plot for $Re_b = 20000$ at section VII ($Y = 50\%$)

3.6 Quadrant Analysis

Quadrant analysis (Antonia, 1981) was performed for the channel to determine the dominant quadrant at each of the point within the channel. Sweeps and ejections near the bed of the channel have been plotted in Fig. 3.54, which determine the sediment distribution pattern near the bed. The plots were prepared by performing quadrant analysis for every point near the bed for at least five convective cycles and identifying the dominant quadrant at each grid point. It can be seen that while the upstream of the cylinders is dominated by sweeps the downstream shows predominant ejections. The intermediate gap and preferential flow paths within the channel are also dominated by ejections. It is observed that with increasing Re, inward and outward interactions become dominant as sweeps and ejections tend to decrease.

3.7 Shear Stress

Bed shear was calculated by using the following formulation (Yen, 2002):

$$\tau_b = \mu \frac{\partial \tilde{\mathbf{u}}}{\partial \tilde{z}}\bigg|_{z=0} \tag{3.4}$$

where $\tilde{\mathbf{u}} = \frac{u}{U}$ is the non-dimensional velocity vector, $\tilde{z} = \frac{z}{H}$ is the non-dimensional distance along channel depth and $\mu = \frac{1}{Re_b}$ is the non-dimensional dynamic viscosity. Shear stress at the bed of the channel is shown in Fig. 3.55 for increasing Re. It is observed that irrespective of the Reynold's number of the flow, bed shear stress around the cylinder is high which is responsible for scouring of bed around a cylinder. The area of high bed shear stress around the cylinders decreases with increasing Re, which indicates more scouring near to the cylinder with increasing bulk flow velocity.

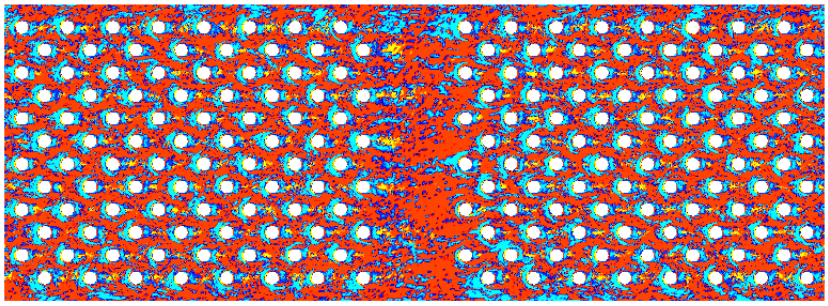

(a) $Re_b = 12000$

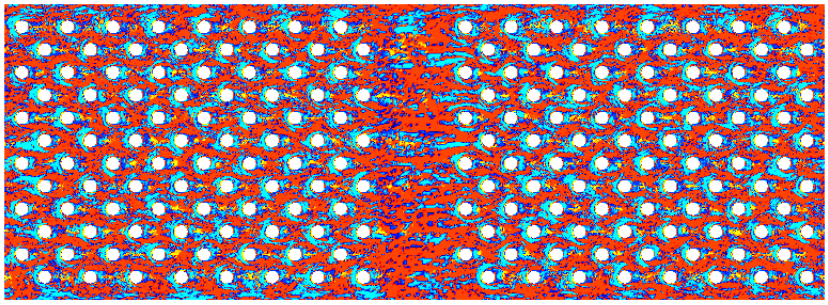

(b) $Re_b = 15000$

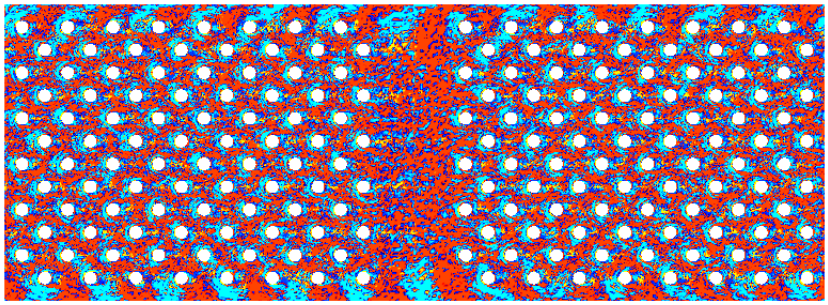

(c) $Re_b = 18000$

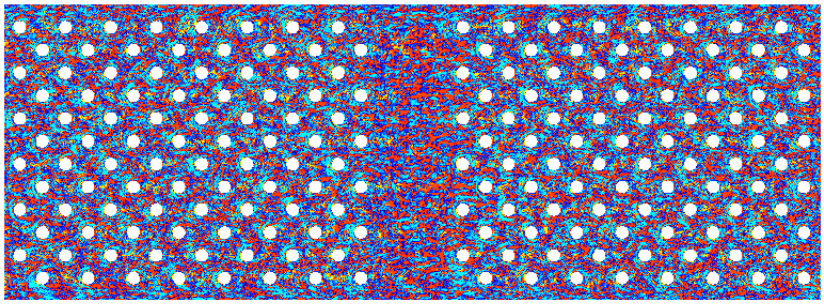

(d) $Re_b = 20000$

Figure 3.54: Dominant Quadrant plots at near bed for increasing Re_b: red represents ejections, cyan represents sweeps, blue and yellow represent inward and outward interactions respectively

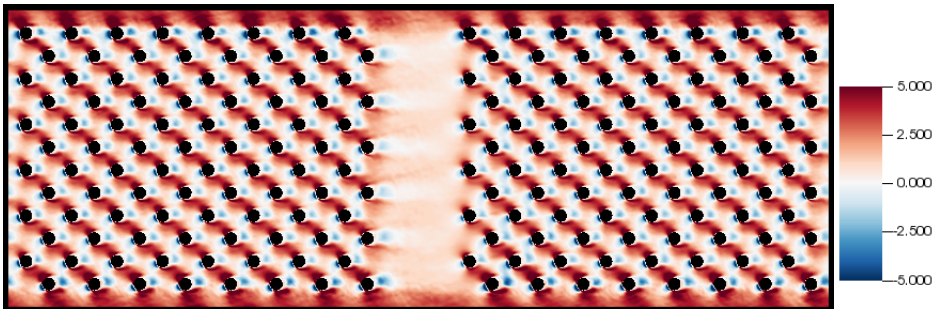

(a) $Re_b = 12000$

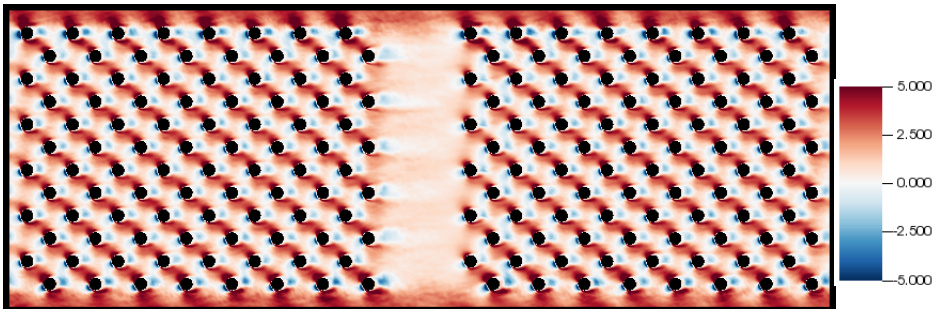

(b) $Re_b = 15000$

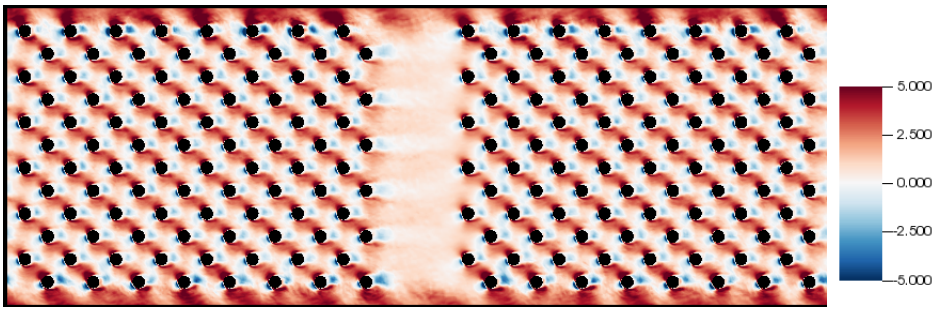

(c) $Re_b = 18000$

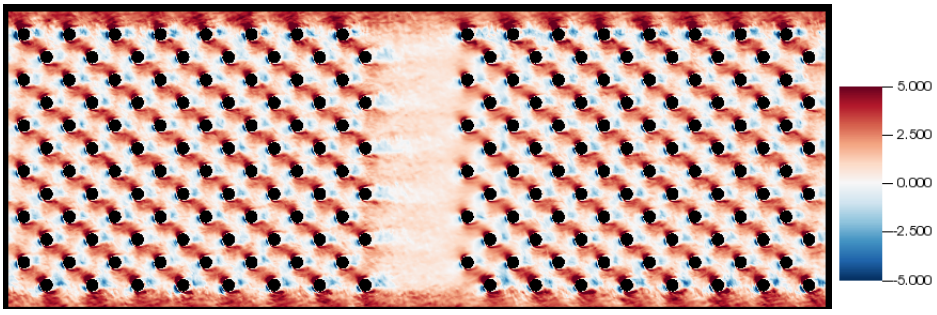

(d) $Re_b = 20000$

Figure 3.55: Bed shear stress plots for increasing Re_b

3.8 Drag Measurements

Drag has been calculated for the entire canopy by integrating the pressure distribution along individual cylinder and summing up for all elements in the canopy. This is akin to the drag measurement of Tinoco and Cowen (2013) who measured the drag on the canopy using a drag plate.

3.8.1 Grid Independence

An important part of every numerical study is to investigate grid independence of the results i.e. there is no significant change in the observed flow characteristics as we increase the resolution of the simulations. Grid resolution in Nek5000 is described by the variable, $lx1$ which represents the polynomial order used for approximating the solution. Fig. 3.56 shows the change in the mean drag measurements as we move from low resolution ($lx1 = 10$) to a high resolution ($lx1 = 12$) simulation, and it can be observed that there is no significant change ($\approx 1.5\%$) in the measured value of mean drag. This validates grid independence of the simulations, i.e. the resolution of $lx1 = 10$ is sufficient to capture the flow characteristics and further increase in grid resolution would not improve the results significantly. Grid independence was studies for the case with highest Reynolds number i.e. $Re = 20000$, and it was assumed that the results will be true for other cases with lower Re as well.

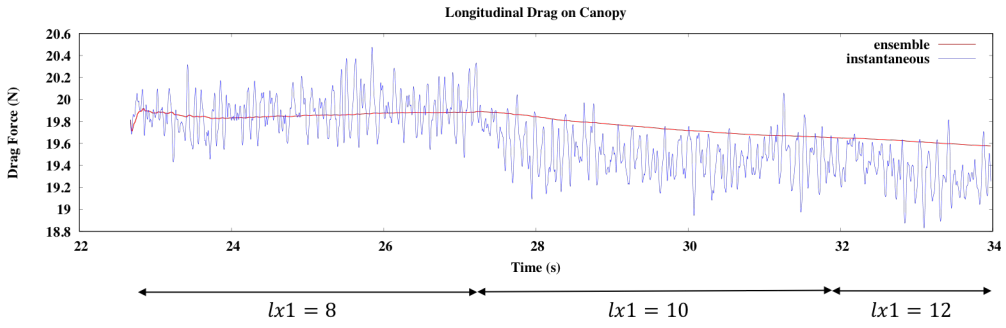

Figure 3.56: Plot showing grid independence for the simulations. As we move from lower ($lx1 = 10$) to higher ($lx1 = 12$) resolution, the measured canopy drag doesn't change significantly.

3.8.2 Drag Coefficient

Fig. 3.57 shows the variation of drag coefficient with the bulk Reynold's number of the flow. Although there is a decrease in drag coefficient with increasing Reynold's number, the change is insignificant which indicates weak dependence of canopy drag coefficient with Reynold's number of the flow. Such trends were also observed in the experiments by Kothyari et al. (2009a), who measured drag on an array of rigid emergent cylinders arranged in a triangular staggering pattern (refer Fig. 3.58). The canopy density λ, i.e. the cross-sectional area per unit bed area for the current study is 0.1106, which is higher than the maximum density (0.0885) in Kothyari et al., so a direct comparison of the drag coefficients could not be made between the two. However the weak dependence of C_D on Re can be clearly observed for both the cases.

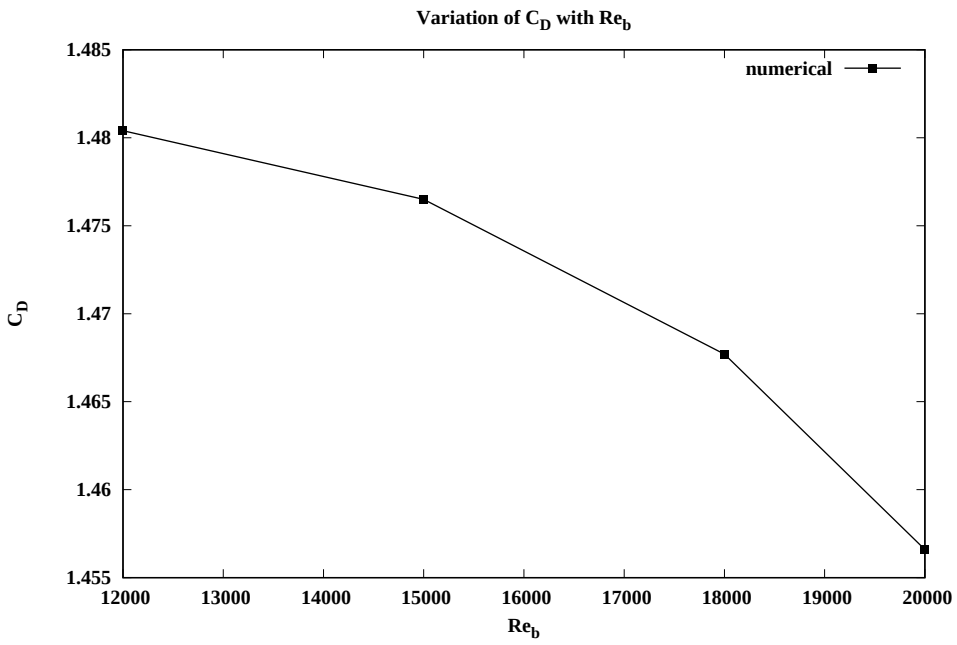

Figure 3.57: Variation of Drag Coefficient with Reynolds Number

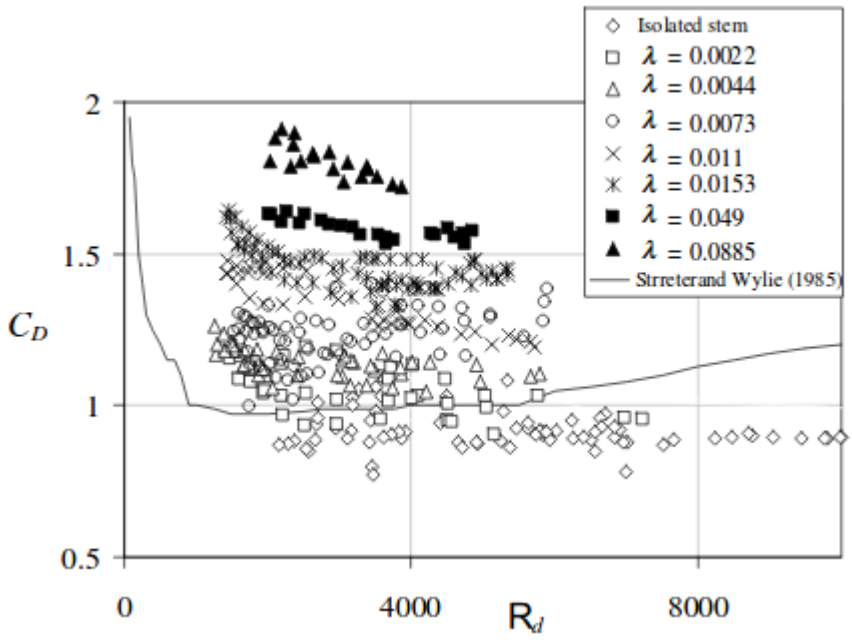

Figure 3.58: Variation of C_D with Re_d for varying canopy density (λ) (Kothyari et al., 2009a)

3.8.3 Drag Time Series

Fig. 3.59-3.62 show the time series of longitudinal and lateral drag on the canopy for increasing Re. A running ensemble of the instantaneous values of drag force has been done to get a time averaged value for drag. It is seen that lateral drag is both positive and negative, which can be attributed to the changing direction of lateral velocity. Hence, ensemble for the lateral drag has been performed for the absolute value of drag force. While the longitudinal drag contributes significantly to the flow resistance, the lateral drag which is generally considered to be insignificant, soars up to $6-8\%$ of the longitudinal drag. Similar trends are observed for higher Reynolds numbers.

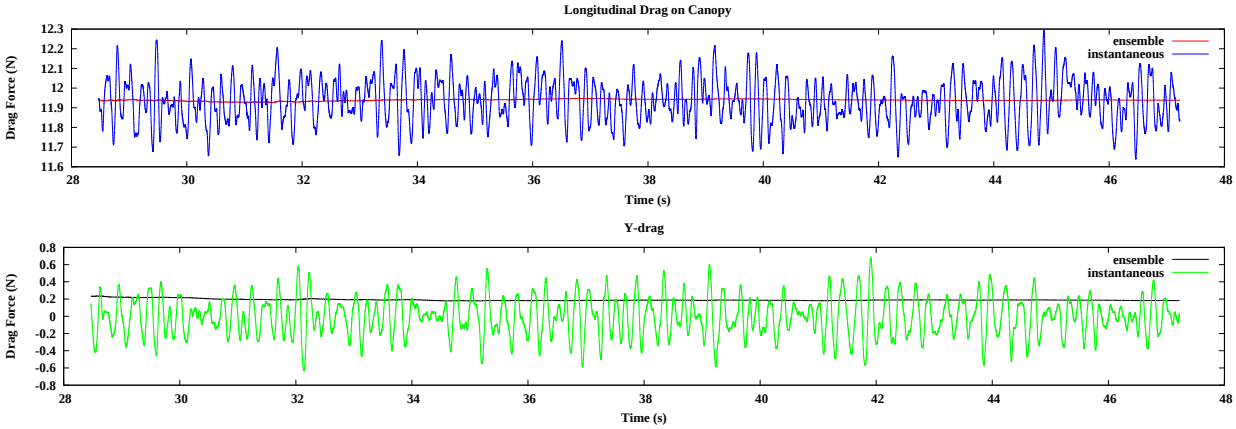

Figure 3.59: Time series of drag measurement for $Re = 12000$

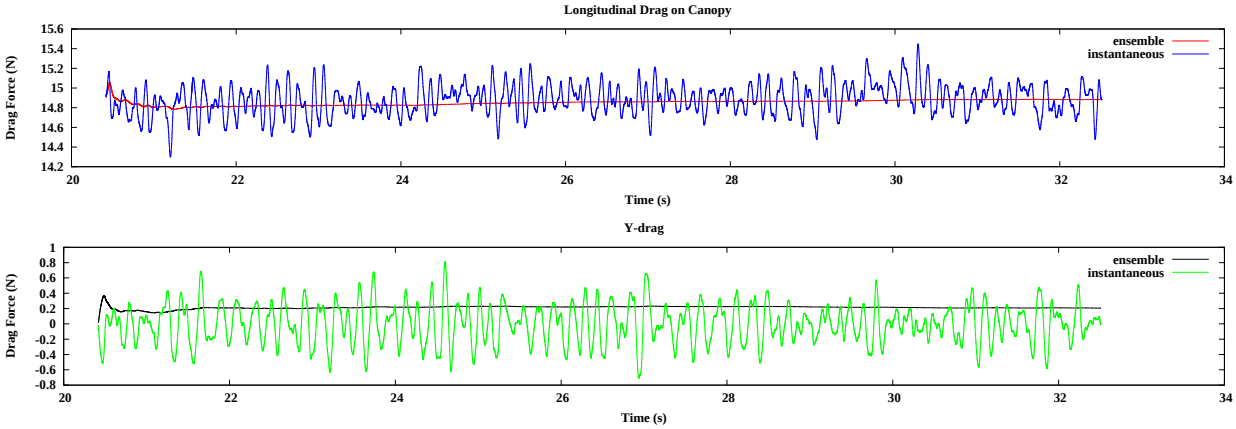

Figure 3.60: Time series of drag measurement for $Re = 15000$

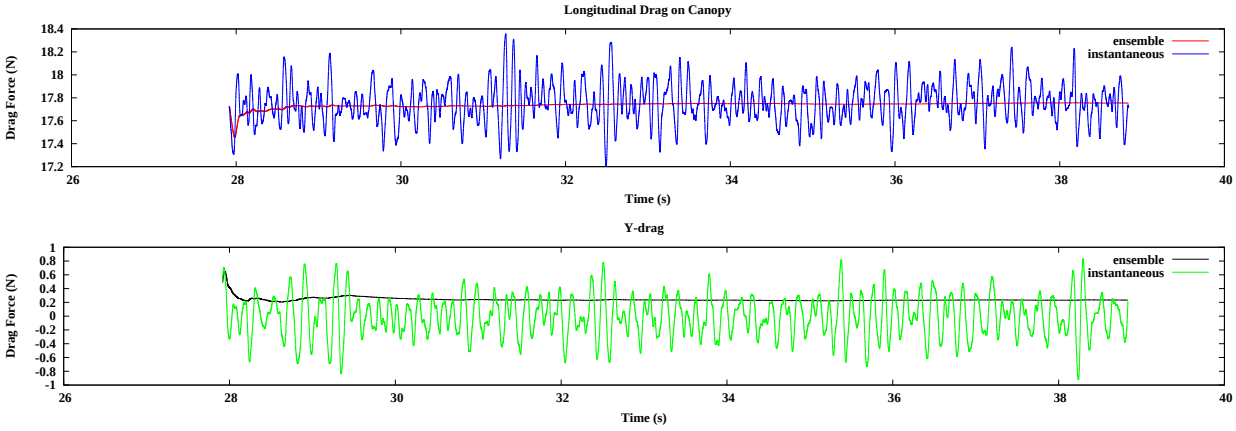

Figure 3.61: Time series of drag measurement for $Re = 18000$

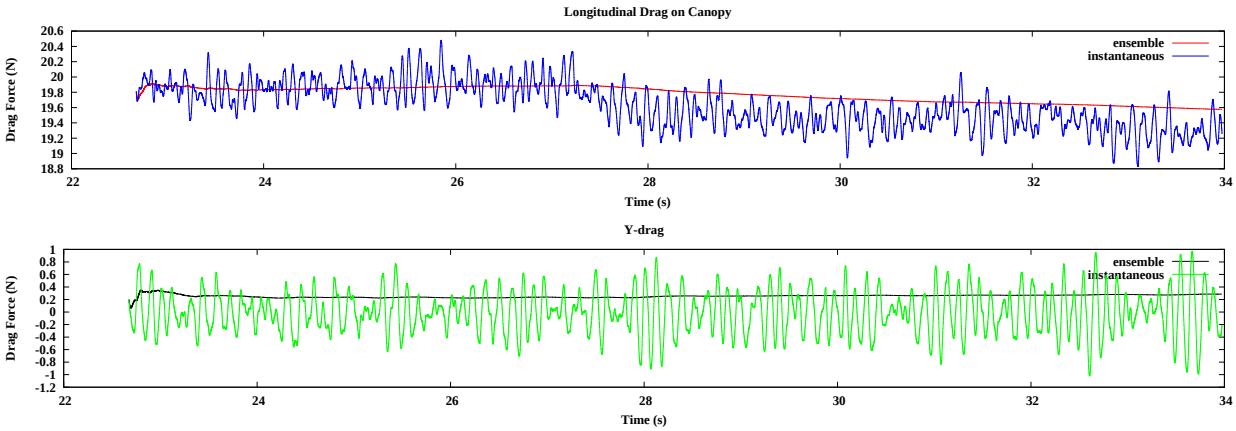

Figure 3.62: Time series of drag measurement for $Re = 20000$

Chapter 4

Suspended Sediment Transport Modeling

4.1 Introduction

Sediment in natural channels is transported primarily as suspended sediment, which plays an important role in the morphodynamics of the system. Suspended sediment differs from the bed load in that it may be diffused throughout the vertical fluid column due to turbulence. Suspended particles are transported by convective fluxes, which has two components: one associated with mean flow and the other with turbulence in the flow. Thus, determination and control of sediment flux in a channel is imperative for engineering applications. However, in situ measurement of suspended sediments is a highly discontinuous and expensive process, so accurate modeling of transport of suspended sediment is essential for correct approximation of the net sediment flux in a river (Dutta et al., 2014). The suspended sediment can be modeled by two approaches, Lagrangian and Eulerian. In the Lagrangian model, each sediment particle is tracked individually while in the Eulerian model, the dispersed phase is treated as a continuum i.e. a scalar field. For sufficiently small particle velocities, the particle velocity is completely governed by the local flow properties, and under these circumstances suspended sediments can be modeled under the Eulerian framework (Ferry & Balachandar, 2001).

Transport of heavy particles under suspension occurs under a turbulent regime. Owing to its weight, these particles have a tendency to settle down, and a concentration gradient develops in the vertical direction. This density stratification modulates the turbulence structure,

thus reducing and suppressing the ability of the flow to carry particles. Due to this constant feedback of sediment to the flow, we have to model the sediments as active scalars. The work presents a model to perform direct numerical simulation (DNS) of sediment-laden flow in a channel employing an Eulerian approach, which has been validated by replicating works of Cantero et al. (2009) and Dutta et al. (2014). The model has been further extended to model transport of suspended sediments through rigid emergent vegetation canopy.

Early attempts at modeling suspended sediment transport through vegetation were done by López and García (1998) who extended the $\kappa - \epsilon$ model from Lopez and Garcia (1997) to compute the values of kinematic eddy viscosity which was then used to solve the sediment diffusion equation and predict the suspended sediment profile in vegetation canopy. They found that the model predictions were in excess of the predictions using the Rouse formula. There have been recent attempts at modeling pollutant (passive scalar) transport through vegetation canopy using Large Eddy Simulations (Poggi et al., 2006; Okamoto & Nezu, 2010; Lu & Dai, 2018). However, to the author's knowledge, transport of active scalars through vegetation canopy have not been successfully modeled using LES till present date. This study is probably one of the first successfully attempts at modeling an active scalar (sediment with fall velocity) in a vegetation canopy using high resolution LES.

4.2 1D model for suspended sediment transport

Initial attempts to model suspended sediment have focused on developing a 1D model to estimate the sediment distribution along the channel depth (Parker, 1978; Rijn, 1984; Ikeda & Nishimura, 1985). The equation describing mass conservation of suspended sediment of uniform size and constant density in a turbulent flow can be written as (M. Garcia & Parker,

1991)

$$\frac{\partial \overline{c}}{\partial t} + \frac{\partial F_i}{\partial x_i} = 0 \tag{4.1}$$

where

$$F_i = (u_i - V_s \delta_{i3})\overline{c} + \overline{u_i' c'} \tag{4.2}$$

x_i = Cartesian coordinate system such that x_3 is directed vertically upward;

t = time;

u_i = fluid velocity averaged over turbulence;

u_i' = turbulent fluctuations;

$\overline{c}$ = volume suspended-sediment concentration averaged over turbulence;

c' = instantaneous fluctuations in concentration;

F_i = volume flux vector of suspended sediment averaged over turbulence;

V_s = fall velocity of sediment in quiescent water;

$\overline{u_i' c'}$ = sediment flux due to turbulence, also known as Reynolds fluxes; and

δ_{i3} is the Kronecker delta, $\delta_{ij} = 0,\ i \neq j$; and $\delta_{ij} = 1,\ i = j$

The main assumption here is that the sediment particles follow the fluid particles except in the vertical ($i = 3$) direction, where gravity introduces an additional fall velocity. The simplest closure assumption to represent the Reynolds fluxes is to assume that these are proportional to the gradient in sediment concentration

$$\overline{u_i' c'} = -D \frac{\partial \overline{c}}{\partial x_i} \tag{4.3}$$

where D is the eddy diffusivity of the sediment.

Equations (4.1) and (4.2) are valid only for dilute suspensions i.e. $\overline{c} \ll 1$ of particles in size less than $0.5mm$. A complete derivation of the above mass conservation equation can

be found in M. Garcia (2001). Equations (4.1) and (4.2) along with (4.3) represent an advection-diffusion equation for suspended sediment transport (M. Garcia, 2001). Considering a uniform turbulent flow over a flat bed in a wide rectangular channel, the equations reduce to

$$\frac{\partial c}{\partial t} - V_s \frac{\partial c}{\partial z} = D \frac{\partial^2 c}{\partial z^2} \tag{4.4}$$

Further considering steady conditions, the equations reduce to

$$\frac{\partial}{\partial z}\left(D \frac{\partial \overline{c}}{\partial z} + V_s \overline{c} \right) = 0 \tag{4.5}$$

4.2.1 Boundary conditions

The net vertical flux of sediment across the water surface is identically zero which forms the upper boundary condition.

$$\overline{F_z}|_{z=H} = -V_s \overline{c} + \overline{w'c'} = 0 \tag{4.6}$$

The boundary condition at the bed differs from that at the surface as it accounts for entrainment of sediment into the flow from the bed and deposition of sediment onto the bed. These boundary conditions accounting for sediment entrainment and deposition have been discussed in great detail in M. H. Garcia (2006). However, for simplicity let's consider that the bed is in equilibrium, i.e. for the amount of sediment settling on the bed an equal amount of sediment is resuspended back into the flow. In this case the boundary condition at the bed remains the same as that at the surface:

$$\overline{F_z}|_{z=b} = -V_s \overline{c} + \overline{w'c'} = 0 \tag{4.7}$$

4.2.2 Suspended sediment profile in a steady channel

When we solve equation (4.5) with boundary conditions described by equations (4.6)-(4.7), we get:

$$D\frac{d\overline{c}}{dz} + V_s\overline{c} = 0 \tag{4.8}$$

If the particles are not too large, it is possible to equate vertical diffusivity of sediment to the vertical eddy viscosity of momentum. The relation for sediment eddy diffusivity then becomes (M. H. Garcia, 2006):

$$D = \kappa u_* z\left(1 - \frac{z}{H}\right) \tag{4.9}$$

where κ is the von Kármán constant, u_* is the shear velocity and H is the channel height. Substitute (4.9) in (4.8), and integrate along the channel depth from near bed, b to z

$$\int_b^z \frac{\overline{c}}{\overline{c}} = \frac{-V_s}{\kappa u_*}\int_b^z \frac{H}{z\,(H-z)}dz$$

$$ln\left(\frac{\overline{c}}{\overline{c}_b}\right) = \frac{-V_s}{\kappa u_*}\, ln\left(\frac{H-z}{z}\right)\Bigg|_b^z$$

$$\frac{\overline{c}}{\overline{c}_b} = \left[\frac{(H-z)/z}{(H-b)/b}\right]^{\frac{-V_s}{\kappa u_*}} \tag{4.10}$$

which is the Rouse-Vanoni-Ippen suspended sediment distribution.

4.2.3 Suspended sediment profile in a unsteady channel

To understand the temporal evolution of vertical suspended sediment profile, we need to solve the unsteady advection diffusion equation (4.4) with boundary conditions defined in (4.6)-(4.7). However, it is not possible to analytically solve equation (4.4), so it can be solved numerically. Upon non-dimensionalization (Section 4.3), the set of equations are

$$\frac{\partial \tilde{c}}{\partial \tilde{t}} + \tilde{\mathbf{V}}_s . \frac{\partial \tilde{c}}{\partial z} = \frac{1}{Re_\tau Sc} \frac{\partial^2 \tilde{c}}{\partial z^2} \qquad \tilde{c}\tilde{V}_s + \frac{1}{Re_\tau Sc} \frac{\partial \tilde{c}}{\partial \tilde{z}} = 0; \quad z = \pm 1 \tag{4.11}$$

A one-dimensional spectral element based numerical scheme was developed in Matlab to solve the above mentioned set of equations (4.11) assuming a uniform sediment concentration at $t = 0$. The results are shown in Figure. 4.1. It was observed that for higher settling velocities, we get higher concentration of sediment at the channel bed. Also, the sediment profile closely resembles the Rouse profile derived in the previous section. Further a stability analysis was performed to determine the range of settling velocities of the sediments, for which the model is stable. Further details of the formulation are given in Appendix A.

4.3 Mathematical Model

Suspended sediment particles are assumed to be of constant size, negligible inertia, and having a constant settling velocity $\tilde{V}_s$. Sediment density is considered to be sufficiently small for Boussinesq approximation to hold true. The mathematical formulations are similar to that used by Cantero et al. (2009) in their study on turbulence modulation due to self-stratification in a channel. Suspended sediment has been modeled as an active scalar using a modified scalar advection diffusion equation to incorporate advection due to fall velocity

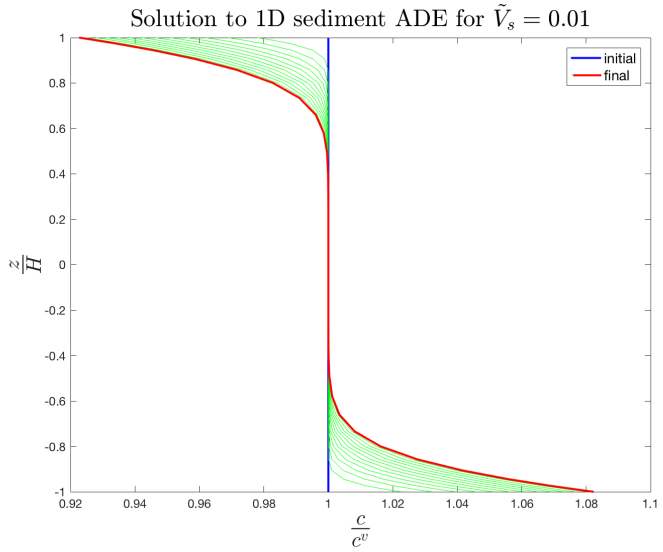

(a) Low settling velocity, $\tilde{V}_s = 0.01$

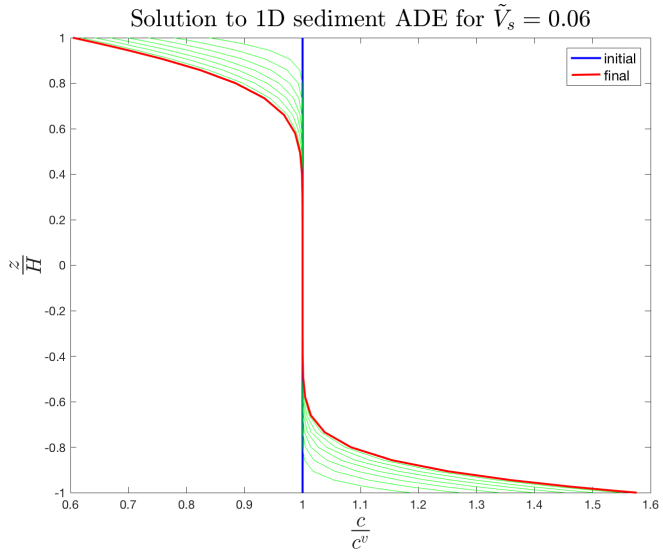

(b) High settling velocity, $\tilde{V}_s = 0.06$

Figure 4.1: Solution to equation (4.11) for increasing settling velocity: The green lines show the evolution of sediment concentration profile with time.

of the sediments. The set of governing equations are:

$$Conservation\ of\ Momentum: \frac{\partial u_i}{\partial t} + u_j \frac{\partial u_i}{\partial x_i} = -\frac{1}{\rho}\frac{\partial p}{\partial x_i} + \mu \frac{\partial^2 u_i}{\partial x_i^2} + gR(c - c^{(h)}) \tag{4.12}$$

$$Conservation\ of\ Mass: \frac{\partial u_i}{\partial x_i} = 0 \tag{4.13}$$

$$Scalar\ transport: \frac{\partial c}{\partial t} + (u_i + \delta_{i3} V_s)\frac{\partial c}{\partial x_i} = D\frac{\partial^2 c}{\partial x_i^2} \tag{4.14}$$

where,

u_i is the fluid velocity (m/s)

ρ_f is the fluid density (kg/m^3)

ρ_s is the sediment density (kg/m^3) p is the fluid pressure (N/m^2)

μ is the dynamic viscosity of fluid (m^2/s)

c is the sediment concentration (m^3/m^3)

V_s is the settling velocity of the sediment (m/s)

D is the sediment diffusivity (m^2/s); and

$gR(c - c^{(h)})$ is the acceleration induced due to stratification (m/s^2), where $R = \left(\frac{\rho_s}{\rho_f} - 1\right)$

The source term effectively modulates turbulence in the flow by counteracting Reynolds stresses with body forces induced as a result of stratification. Here we use x_i to account for the three spatial components, $x_1 = x$ (longitudinal), $x_2 = y$ (transverse) and $x_3 = z$ (vertical), with the associated velocities u, v and w respectively. The equations are further non-dimensionalized using the shear parameters of the flow i.e. shear velocity u_*. When required, it can also be easily non-dimensionalized using bulk flow parameter i.e. bulk velocity U_b. The set of dimensionless equations used to model the flow are:

$$\frac{\partial \tilde{\mathbf{u}}}{\partial \tilde{t}} + \tilde{\mathbf{u}}.\nabla\tilde{\mathbf{u}} = \tilde{\mathbf{G}} - \nabla\tilde{p} + \frac{1}{Re_\tau}\nabla^2\tilde{\mathbf{u}} + Ri_\tau\left(\tilde{c} - c^{(h)}\right)\mathbf{e}_g \tag{4.15}$$

$$\nabla.\tilde{\mathbf{u}} = 0 \tag{4.16}$$

$$\frac{\partial \tilde{c}}{\partial \tilde{t}} + \left(\tilde{\mathbf{u}} + \tilde{\mathbf{V}}_s\right).\nabla\tilde{c} = \frac{1}{Re_\tau Sc}\nabla^2\tilde{c} \tag{4.17}$$

where $\tilde{\mathbf{u}} = \left(\frac{u}{u_*}, \frac{v}{u_*}, \frac{w}{u_*}\right)$ is the dimensionless fluid velocity, $\tilde{c} = \frac{c}{c^v}$ is the dimensionless volumetric concentration of suspended sediments, $c^{(h)}$ is the horizontally averaged dimensionless sediment concentration, $\mathbf{e}_g$ is the unit vector in the direction of gravity, $\tilde{p} = \frac{p}{\rho u_*^2}$ is the pressure field, $\tilde{\mathbf{G}}$ is the driving pressure gradient, and $\tilde{\mathbf{V}}_s = \left(0, 0, -\frac{V_s}{u_*}\right)$ is the dimen-

sionless settling velocity of the sediments.

The non-dimensional numbers appearing in equations (4.15)-(4.17) are defined as:

$$Reynold's number \ : Re_\tau = \frac{u_* h}{\nu} \tag{4.18}$$

$$Richardson number \ : Ri_\tau = \frac{gRc^v h}{u_*^2} \tag{4.19}$$

$$Schmidt Number \ : \frac{\nu}{k} \tag{4.20}$$

Here u_* is the shear velocity, h is the half height of the channel, g is the acceleration due to gravity, $\nu = \frac{\mu}{\rho}$ is the kinematic viscosity, and $c^v = \frac{1}{V}\int c \ dV$ is the volume averaged concentration.

Initial condition of the flow is turbulent with uniform distribution of sediments along all channel dimensions. Periodic boundary conditions were applied in longitudinal and lateral directions for both flow and sediments. No slip bottom boundary condition and no shear top boundary condition was applied for the flow in the vertical direction. For sediments, the following boundary conditions were applied:

$$\tilde{c}\tilde{V}_s + \frac{1}{Re_\tau Sc}\frac{\partial \tilde{c}}{\partial \tilde{z}} = 0 \quad z = \pm 1 \tag{4.21}$$

The sediment boundary condition represents an equilibrium between advective flux and diffusive flux of sediment, i.e. the flux of sediment is balanced by flux due to turbulent diffusion at the boundary. The above equations (4.15)-(4.17) along with the relevant boundary and initial conditions were solved using Nek5000 which is a spectral element based higher-order incompressible Navier-Stokes solver. The turbulence modulation term, $gRi_\tau \left(\tilde{c} - c^{(h)}\right)$ in the momentum equation and the additional advection term due to sediment settling velocity, $\tilde{V}_s \frac{\partial \tilde{c}}{\partial \tilde{x}}$ were treated as source terms in the momentum and scalar transport equations in Nek5000, respectively.

4.4 Cases Simulated and Geometry Description

Two different geometries were simulated to investigate the flow-vegetation-sediment interactions in open channel. The details of different geometries are summarized in Table 4.1

Table 4.1: Geometries simulated for suspended sediment modeling

Geometry No.	Description	Relevant scales
Geom. I	Sediment transport in a channel	Channel Half Height (h) Shear Velocity (u_*) Volumetric Sediment Concentration (c^v)
Geom II	Sediment transport through vegetation	Channel Height (H) Bulk Velocity (U_b) Volumetric Sediment Concentration (c^v)

4.4.1 Geom. I: Sediment transport in a channel

This is the case of flow in a sediment laden closed channel with smooth walls on top and bottom. The equations were non-dimensionalized using the shear velocity (u_*), channel half height (h) and volume averaged sediment concentration,(c^v) as scales for velocity, length and sediment concentration respectively. Dimensions of the rectangular domain used for the simulation were $\tilde{L}_x = 4\pi$, $\tilde{L}_y = \frac{4\pi}{3}$, $\tilde{L}_z = 2$ and was spatially discretized into 720 uniform elements (Fig. 4.2). Each element was discretized with Gauss-Lobatto-Legendre quadrature nodes in the three dimensions and hence the simulation involved a total of over 1.2 million nodes, which sufficiently resolved to be referred as DNS. The channel was considered to be periodic in both longitudinal and lateral directions for both fluid and sediments. It had smooth walls at both the ends in vertical direction, Z and hence no slip boundary condition was applied for fluid at both the walls. However, for the sediments, the equilibrium boundary condition was applied at both the walls, as described in equation 4.21. Three cases were

replicated from Cantero et al. (2009) which are summarized in Table 4.2. A uniform initial condition of $\tilde{c} = 1$ was used for all the cases.

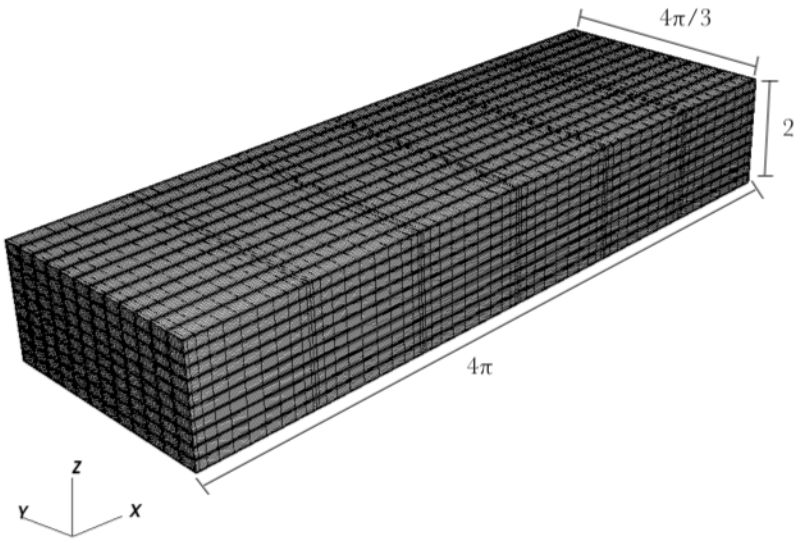

Figure 4.2: Mesh and dimensions for Geom. I

Table 4.2: Cases simulated for Geom. I

Case	$\widetilde{V}_s$	Re_τ	Ri_τ	Sc
SS1	5×10^{-3}	180	18	1
SS3	1.5×10^{-2}	180	18	1
SS5	2×10^{-2}	180	18	1

4.4.2 Geom. II: Sediment transport through vegetation

In this case, suspended sediment transport through a staggered array of vegetation has been modeled. The geometry for this case is shown in figure 4.3, and is exactly the same as that used for the simulation of flow through vegetation. However, unlike Geom. I, here the momentum and sediment transport equations were non-dimensionalized using the bulk velocity (U_b), channel height (H) and volumetric sediment concentration (c^v) as scales for velocity, length and sediment concentration respectively. Further, the channel is periodic in longitudinal and lateral directions for both fluid and sediments. The bottom boundary for fluid is treated as a wall, while the surface holds the rigid lid assumption. Top and bottom boundary conditions for sediment are the same equilibrium conditions as discussed for Geom. I. Only one case was simulated with bulk Reynolds number of flow, $Re_b = 12000$ and dimensionless sediment fall velocity, $\tilde{V_s} = 0.01$. This translates to a physical bulk flow velocity of 0.12 m/s and a settling velocity of 1.2 mm/s. However, modulation of turbulence due to stratification was not considered for this case.

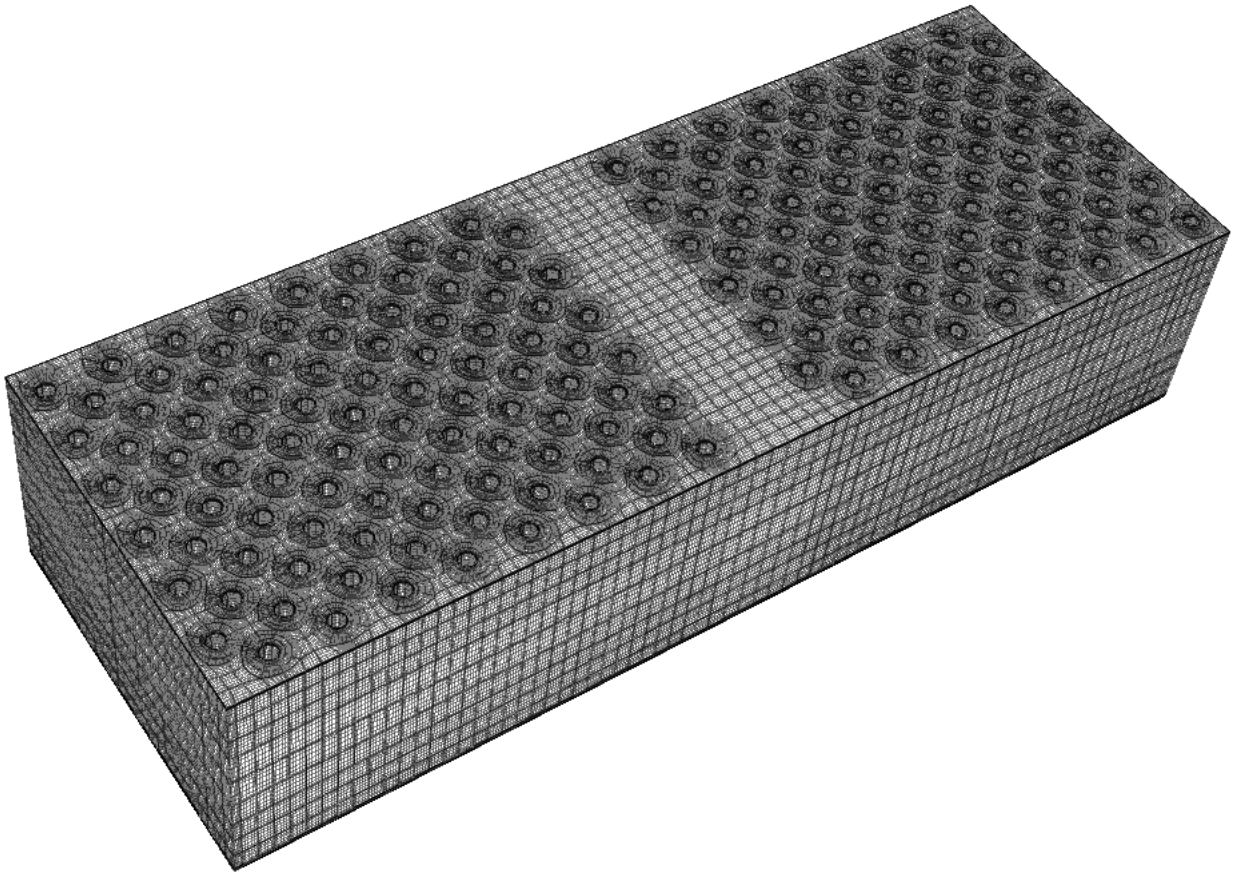

Figure 4.3: Mesh for Geom.II: The high resolution around each cylinder, at the top and bottom boundary is sufficient to resolve boundary layer around the cylinders and at the bed

4.5 Results and Discussion

This section discusses the findings from simulation of sediment transport in closed channel and within a patch of vegetation. As per author's knowledge, high resolution modeling of suspended sediment through vegetation canopy has not been successfully attempted till present day, and these results show probably the first successful attempt at modeling suspended sediment through vegetation canopy.

4.5.1 Geom I: Sediment transport in a channel

The results from sediment transport in periodic channel was compared with the results from previous simulations performed by Cantero et al. (2009); Dutta et al. (2014). These previous studies performed DNS for the periodic channel to investigate effects of self stratification and forced stratification of sediment concentration on the turbulence characteristics of the flow. However, for the current study, these comparisons are done to validate the sediment transport model developed in Nek5000. Fig. 4.4 shows the spatially averaged sediment concentration field, where sediment concentrations are dominantly high near the channel bed and lowers as we move vertically upwards. Further, form the TKE field shown in fig. 4.5, we can clearly see that maximum contribution towards turbulence comes from the top wall as opposed to the bottom wall. A comparison of fig. 4.4 and 4.5 indicates that this is a result of turbulence modulation due to concentration stratification in the channel.

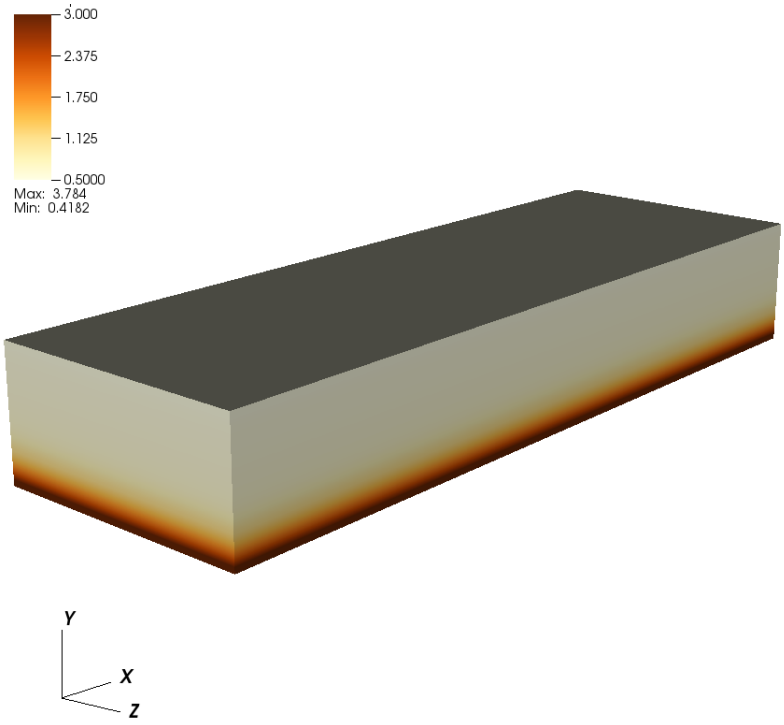

Figure 4.4: Steady state sediment concentration field for case SS3

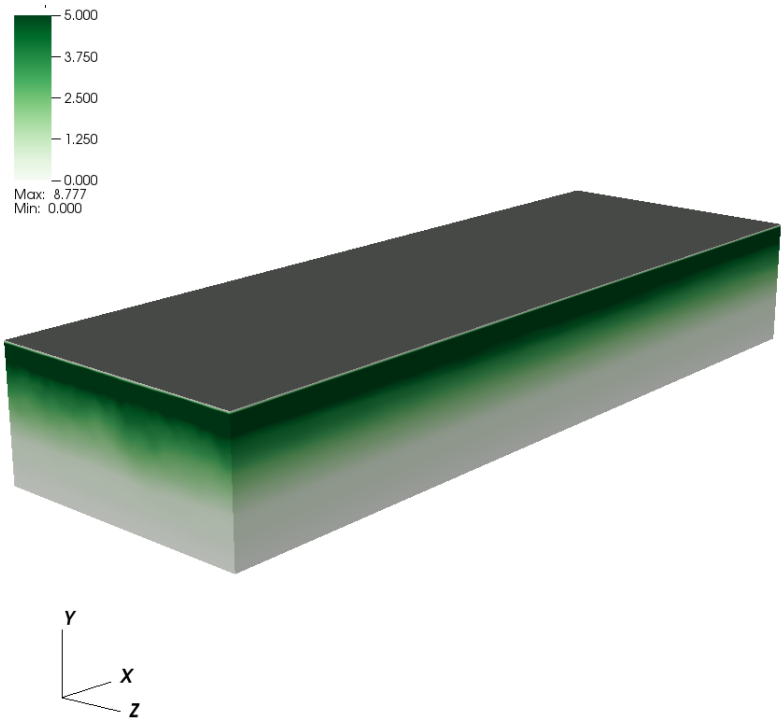

Figure 4.5: Turbulent Kinetic Energy field for case SS3

Fig. 4.6 shows the sediment concentration profiles along the depth of channel from the current study (solid line) and from previous studies (dashed line). The sediment concentration profiles which closely resemble the Rousean profile, are similar to steady state profiles from the 1D model. It is seen that, although the results are close match for lower settling velocities (SS1), the sediment concentration profiles from the current study evolve further than in previous studies for higher settling velocities (SS3,SS5). This is because the previous studies may not have simulated the cases for enough convective flow cycles, so as to reach a statistically steady state. This is further validated as the steady state sediment profiles from the previous studies, were found to be one of the transient sediment profiles in the current study. Some deviation may also be an artifact of errors in digitization of the previous plots and also due to the higher grid resolution of the current study.

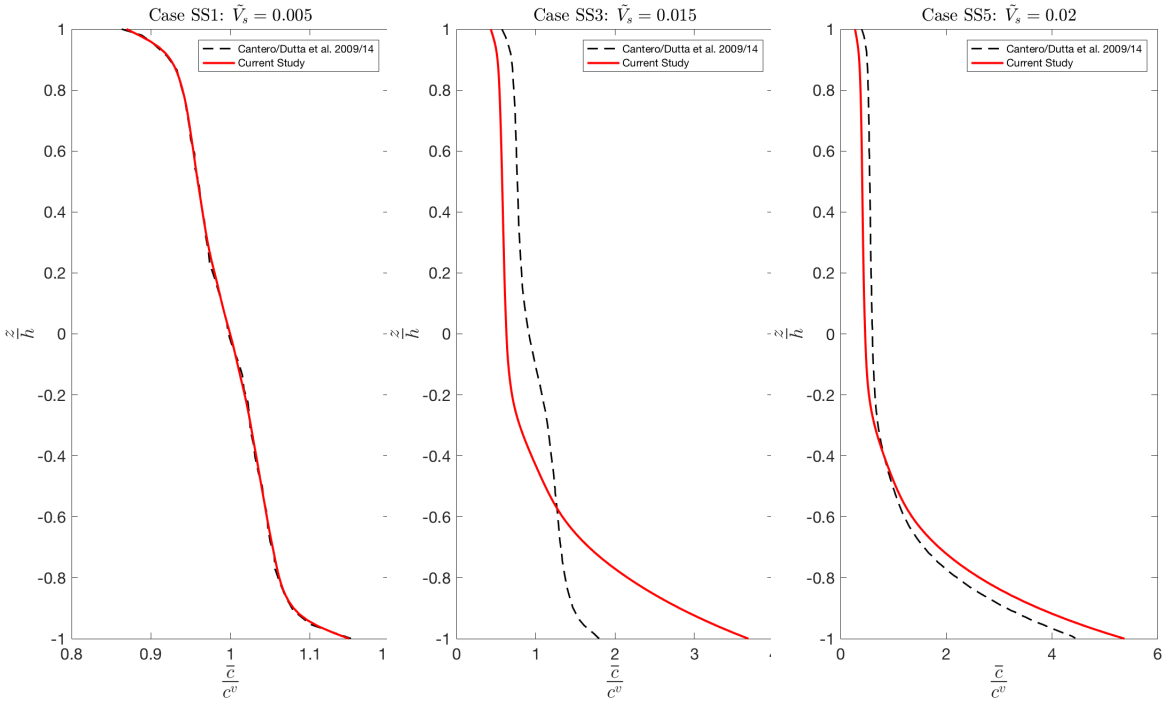

(a) Case SS1 (b) Case SS3 (c) Case SS5

Figure 4.6: Comparison of the sediment concentration profiles from the current study with those from Cantero et al. (2009); Dutta et al. (2014)

Conclusively, it is evident from the findings that the sediment transport model in Nek5000 is capable of modeling suspended sediment transport in channel. Further this model has been used to study sediment transport through vegetation canopy.

4.5.2 Geom II: Sediment transport through vegetation

Fig. 4.7 shows the suspended sediment distribution within the vegetation patch. Stratification within the vegetation patch is evident as there is high concentration of sediments near the channel bed and lower concentration towards the surface. At the bed, we observe high concentration zones within the intermediate gap and in the wakes of the cylinders. This is due to dominant zones of low velocity in the aforementioned areas as shown in fig. 4.8. Also, these results are in close agreement with the TKE and Turbulence Intensity distribution observed in sections 3.3 and 3.5. It was observed that the sediments of the same settling

velocity settled much quicker than in the case of a closed channel. This is due to the lower level of turbulence within the vegetation canopy as compared to the channel, which prevent the resuspension of the sediments. The results conclusively validate the ability of the model to accurately predict suspended sediment transport through rigid vegetation canopy and it can be extended to explore effects of different settling velocities on sediment distribution within the patch.

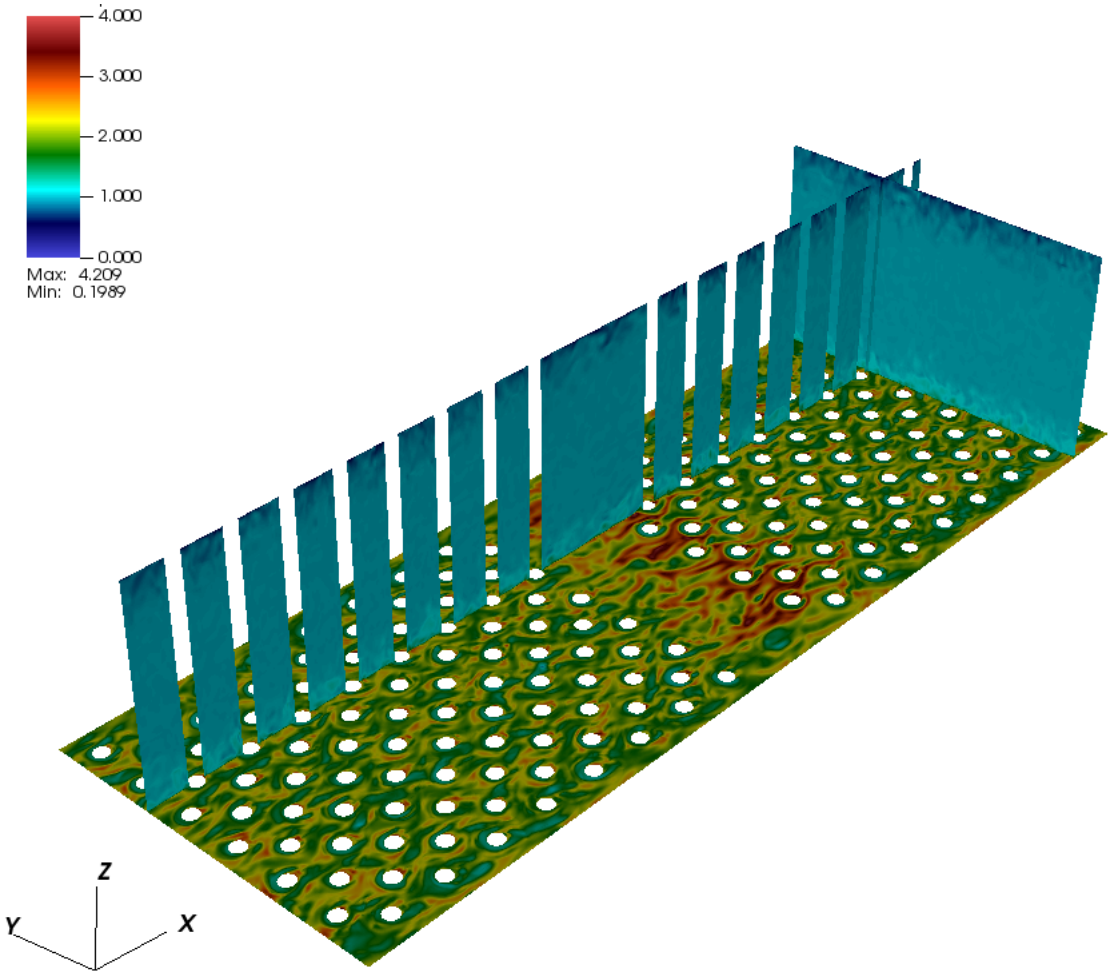

Figure 4.7: Sediment concentration field at the bed and along the longitudinal and lateral cross-sections of vegetation canopy

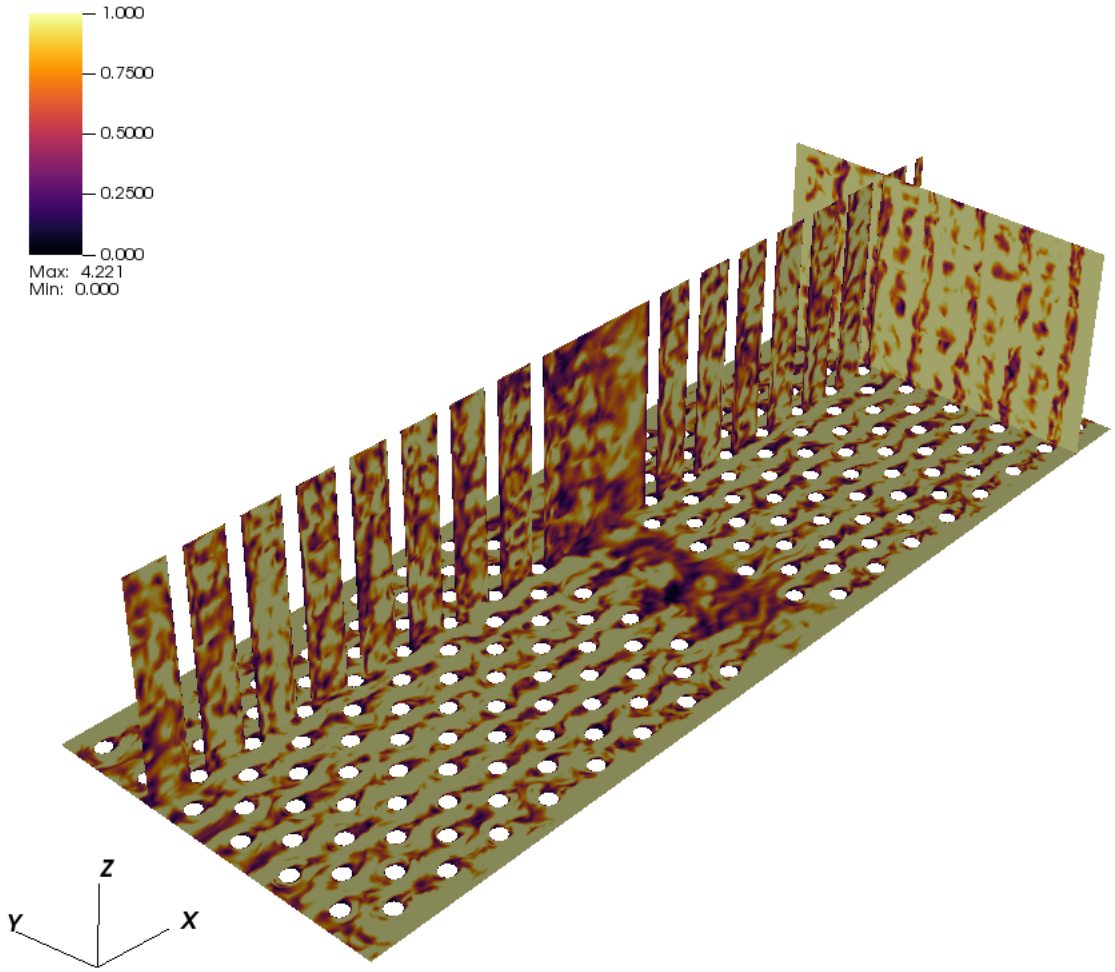

Figure 4.8: Velocity field at near bed and along the longitudinal and lateral cross-sections of vegetation canopy

Chapter 5

Conclusion and Future Work

High resolution Large Eddy Simulations were performed on an unstructured grid to simulate the flow and sediment transport through rigid emergent vegetation. Flow characteristics, such as time averaged velocity, turbulent kinetic energy, bed shear stress, Reynolds stresses etc. were investigated for increasing Reynolds number of the flow. Dominant flow paths within the vegetation array, and low velocity zones behind the wakes of the cylinder were clearly observed. Further, from the plots of TKE, Reynolds stresses and Turbulence intensity, it was found that stem scale turbulence structures were dominant in the flow. The quadrant analysis showed dominant regions of sweep upstream of the cylinders and ejections in the downstream and along the preferential paths of the flow. However, with increasing flow Reynolds number, the inward and outward interactions started becoming dominant.

Drag measurement on the canopy reflected the weak dependence of drag on Reynolds number (H. Nepf, 1999; Kothyari et al., 2009a). It was found that lateral drag, which is often considered insignificant, can at times be significant contributor to the net drag on the canopy. A major motivation behind the study was to investigate if the measurements within the intermediate gap are representative of the flow characteristics within the vegetation canopy. It was however found that the gap, which was a dominant low velocity zone is not representative of any flow characteristics within the canopy. This has implications on the experiments perfomed using instruments where a portion of the vegetation is cleared inside the canopy to take measurements. Such method of experimentation may alter the flow characteristics significantly and the measurements may be non-representative of the actual flow characteristics.

Direct Numerical Simulations (DNS) of a closed channel were performed to validate the sediment transport model developed in Nek5000. The setup was same as the one used by Cantero et al. (2009); Dutta et al. (2014) and three cases were simulated to compare against the findings of the current study. The vertical profiles sediment concentration from the current study were in good agreement with the previous findings of Cantero et al. (2009); Dutta et al. (2014). Self stratification in the channel reduced the turbulence levels in the zones of higher sediment concentration. The results conclusively indicated that suspended sediment transport model in Nek5000 is able to capture the relevant physics of flow in sediment laden channels. Hence, the model was extended to simulate suspended sediment transport through an array of rigid emergent vegetation. The sediment concentration distribution in the channel was found to in line with the existing theory. This is probably the first successful attempt at modeling suspended sediment transport through a vegetation patch using high resolution Large Eddy Simulations.

The results from the current study validate the capability of the model to accurately predict the flow and suspended sediment transport characteristics within a vegetation canopy. In the future, it would be of interest to simulate flow through different arrangement patterns of vegetation and with varying vegetation density. Based on the current and future findings a new formulation for drag coefficient can be derived. Further, the sediment transport model can be used to predict sediment distribution within the canopy with varying flow Reynolds number, vegetation arrangement pattern, sediment fall velocity, level of stratification and vegetation density.

References

Antonia, R. (1981). Conditional sampling in turbulence measurement. *Annual review of fluid mechanics*, *13*(1), 131–156.

Argonne National Laboratory, Illinois. (2017, December). *Nek5000 17.0.* Retrieved from https://nek5000.mcs.anl.gov

Beudin, A., Kalra, T. S., Ganju, N. K., & Warner, J. C. (2017). Development of a coupled wave-flow-vegetation interaction model. *Computers & Geosciences*, *100*, 76–86.

Bode, B., Butler, M., Dunning, T., Hoefler, T., Kramer, W., Gropp, W., & Hwu, W.-m. (2013, April). The Blue Waters super-system for super-science. In *Contemporary high performance computing* (pp. 339–366). Chapman and Hall/CRC. Retrieved from http://www.crcnetbase.com/doi/abs/10.1201/b14677-16 doi: doi:10.1201/b14677-16

Cantero, M. I., Balachandar, S., & Parker, G. (2009). Direct numerical simulation of stratification effects in a sediment-laden turbulent channel flow. *Journal of Turbulence*(10), N27.

Carollo, F., Ferro, V., & Termini, D. (2002). Flow velocity measurements in vegetated channels. *Journal of Hydraulic Engineering*, *128*(7), 664–673.

Carpenter, S. R., & Lodge, D. M. (1986). Effects of submersed macrophytes on ecosystem processes. *Aquatic botany*, *26*, 341–370.

Champion, P. D., & Tanner, C. C. (2000). Seasonality of macrophytes and interaction with flow in a new zealand lowland stream. *Hydrobiologia*, *441*(1), 1–12.

Chang, W.-Y., Constantinescu, G., & Tsai, W. F. (2017). On the flow and coherent structures generated by a circular array of rigid emerged cylinders placed in an open channel with flat and deformed bed. *Journal of Fluid Mechanics*, *831*, 1–40.

Chen, C.-l. (1976). Flow resistance in broad shallow grassed channels. *Journal of the Hydraulics Division*, *102*(3), 307–322.

Cheng, N.-S., & Nguyen, H. T. (2010). Hydraulic radius for evaluating resistance induced by simulated emergent vegetation in open-channel flows. *Journal of Hydraulic Engineering*, *137*(9), 995–1004.

Childs, H., Brugger, E., Whitlock, B., Meredith, J., Ahern, S., Pugmire, D., … Navrátil, P. (2012, Oct). VisIt: An End-User Tool For Visualizing and Analyzing Very Large Data. In *High Performance Visualization–Enabling Extreme-Scale Scientific Insight* (p. 357-372).

Chow, V. T. (1959). *Open-channel hydraulics* (Vol. 1).

Cui, J., & Neary, V. (2002). Large eddy simulation (les) of fully developed flow through vegetation. In *Proceedings of the 5th international conference on hydroinformatics.*

Cui, J., & Neary, V. S. (2008). Les study of turbulent flows with submerged vegetation. *Journal of Hydraulic Research*, *46*(3), 307–316.

Deville, M. O., Fischer, P. F., & Mund, E. H. (2002). *High-order methods for incompressible fluid flow* (Vol. 9). Cambridge university press.

Dutta, S., Cantero, M., & Garcia, M. (2014). Effect of self-stratification on sediment diffusivity in channel flows and boundary layers: a study using direct numerical simulations. *Earth Surface Dynamics*, *2*(2), 419–431.

Etminan, V., Lowe, R. J., & Ghisalberti, M. (2017). A new model for predicting the drag exerted by vegetation canopies. *Water Resources Research*, *53*(4), 3179–3196.

Fairbanks, J. D., & Diplas, P. (1998). Turbulence characteristics of flows through partially and fully submerged vegetation. In *Engineering approaches to ecosystem restoration* (pp. 865–870).

Fathi-Maghadam, M., & Kouwen, N. (1997). Nonrigid, nonsubmerged, vegetative roughness on floodplains. *Journal of Hydraulic Engineering*, *123*(1), 51–57.

Ferry, J., & Balachandar, S. (2001). A fast eulerian method for disperse two-phase flow. *International journal of multiphase flow*, *27*(7), 1199–1226.

Fischer, P. F., Loth, F., Lee, S. E., Lee, S.-W., Smith, D. S., & Bassiouny, H. S. (2007). Simulation of high-reynolds number vascular flows. *Computer methods in applied mechanics and engineering*, *196*(31-32), 3049–3060.

Fischer-Antze, T., Stoesser, T., Bates, P., & Olsen, N. (2001). 3d numerical modelling of open-channel flow with submerged vegetation. *Journal of Hydraulic Research*, *39*(3), 303–310.

Fisher, K. (1992). The hydraulic roughness of vegetated channels. *Report SR*, *305*.

Garcia, M. (2001). *Modeling sediment entrainment into suspension, transport, and deposition in rivers.* Wiley & Sons, Chichester, UK.

Garcia, M., & Parker, G. (1991). Entrainment of bed sediment into suspension. *Journal of Hydraulic Engineering*, *117*(4), 414–435.

Garcia, M. H. (2006). Asce manual of practice 110—sedimentation engineering: Processes, measurements, modeling and practice. In *World environmental and water resource congress 2006: Examining the confluence of environmental and water concerns* (pp. 1–4).

García, M. H., López, F., Dunn, C., & Alonso, C. V. (2004). Flow, turbulence, and resistance in a flume with simulated vegetation. *Riparian vegetation and fluvial geomorphology*, 11–27.

Ghisalberti, M., & Nepf, H. (2004). The limited growth of vegetated shear layers. *Water Resources Research*, *40*(7).

Green, E. P., Short, F. T., Frederick, T., et al. (2003). *World atlas of seagrasses.* Univ of California Press.

Green, J. C. (2005). Comparison of blockage factors in modelling the resistance of channels containing submerged macrophytes. *River research and applications*, *21*(6), 671–686.

Green, J. C. (2006). Effect of macrophyte spatial variability on channel resistance. *Advances in Water Resources*, *29*(3), 426–438.

Huai, W., Zeng, Y., Xu, Z., & Yang, Z. (2009). Three-layer model for vertical velocity distribution in open channel flow with submerged rigid vegetation. *Advances in Water Resources*, *32*(4), 487–492.

Huthoff, F., Augustijn, D., & Hulscher, S. J. (2007). Analytical solution of the depth-averaged flow velocity in case of submerged rigid cylindrical vegetation. *Water resources research*, *43*(6).

Ikeda, S., & Nishimura, T. (1985). Bed topography in bends of sand-silt rivers. *Journal of Hydraulic Engineering*, *111*(11), 1397–1410.

James, C., Birkhead, A., Jordanova, A., & O'sullivan, J. (2004). Flow resistance of emergent vegetation. *Journal of Hydraulic Research*, *42*(4), 390–398.

Järvelä, J. (2002). Flow resistance of flexible and stiff vegetation: a flume study with natural plants. *Journal of hydrology*, *269*(1-2), 44–54.

Klopstra, D., Barneveld, H., Van Noortwijk, J., & Van Velzen, E. (1996). Analytical model for hydraulic roughness of submerged vegetation. In *Proceedings of the congress-international association for hydraulic research* (pp. 775–780).

Koch, E. W. (2001). Beyond light: physical, geological, and geochemical parameters as possible submersed aquatic vegetation habitat requirements. *Estuaries*, *24*(1), 1–17.

Kothyari, U. C., Hayashi, K., & Hashimoto, H. (2009a). Drag coefficient of unsubmerged rigid vegetation stems in open channel flows. *Journal of Hydraulic Research*, *47*(6), 691–699.

Kothyari, U. C., Hayashi, K., & Hashimoto, H. (2009b). Drag coefficient of unsubmerged rigid vegetation stems in open channel flows. *Journal of Hydraulic Research*, *47*(6), 691–699.

Kouwen, N., & Unny, T. E. (1973). Flexible roughness in open channels. *Journal of the Hydraulics Division*, *99*(hy5).

Kreiss, H.-O., & Oliger, J. (1972). Comparison of accurate methods for the integration of hyperbolic equations. *Tellus*, *24*(3), 199–215.

Li, R., & Shen, H. W. (1973). Effect of tall vegetations on flow and sediment. *Journal of the hydraulics division*, *99*(hy5).

Lindner, K. (1982). *Der strömungswiderstand von pflanzenbeständen. mitteilungen 75. leichtweiss-institut für wasserbau, technische universität braunschweig* (Unpublished doctoral dissertation). Doctoral thesis.

Liu, D., Diplas, P., Fairbanks, J., & Hodges, C. (2008). An experimental study of flow through rigid vegetation. *Journal of Geophysical Research: Earth Surface*, *113*(F4).

Lopez, F., & Garcia, M. (1997). *Open-channel flow through simulated vegetation: Turbulence modeling and sediment transport.* (Tech. Rep.). ILLINOIS UNIV AT URBANA DEPT OF CIVIL ENGINEERING.

López, F., & García, M. (1998). Open-channel flow through simulated vegetation: Suspended sediment transport modeling. *Water resources research*, *34*(9), 2341–2352.

López, F., & García, M. H. (2001). Mean flow and turbulence structure of open-channel flow through non-emergent vegetation. *Journal of Hydraulic Engineering*, *127*(5), 392–402.

Lu, J., & Dai, H. (2018). Numerical modeling on pollution transport in flexible vegetation.

Applied Mathematical Modelling.

Luhar, M., Rominger, J., & Nepf, H. (2008). Interaction between flow, transport and vegetation spatial structure. *Environmental Fluid Mechanics*, *8*(5-6), 423.

Maskell, E. (1963). *A theory of the blockage effects on bluff bodies and stalled wings in a closed wind tunnel* (Tech. Rep.). AERONAUTICAL RESEARCH COUNCIL LONDON (UNITED KINGDOM).

Neary, V. (2003). Numerical solution of fully developed flow with vegetative resistance. *Journal of engineering mechanics*, *129*(5), 558–563.

Nepf, H. (1999). Drag, turbulence, and diffusion in flow through emergent vegetation. *Water resources research*, *35*(2), 479–489.

Nepf, H., Sullivan, J., & Zavistoski, R. (1997). A model for diffusion within emergent vegetation. *Limnology and Oceanography*, *42*(8), 1735–1745.

Nepf, H. M. (2012). Flow and transport in regions with aquatic vegetation. *Annual Review of Fluid Mechanics*, *44*, 123–142.

Nicolle, A., & Eames, I. (2011). Numerical study of flow through and around a circular array of cylinders. *Journal of Fluid Mechanics*, *679*, 1–31.

Okamoto, T.-a., & Nezu, I. (2010). Large eddy simulation of 3-d flow structure and mass transport in open-channel flows with submerged vegetations. *Journal of Hydro-environment Research*, *4*(3), 185–197.

Olsen, N. R., & Stokseth, S. (1995). Three-dimensional numerical modelling of water flow in a river with large bed roughness. *Journal of Hydraulic Research*, *33*(4), 571–581.

Oplatka, M. (1998). *Stabilität von weidenverbauungen an flussufern. mitteilungen 156, versuchsanstalt für wasserbau, hydrologie und glaziologie, eth zürich* (Unpublished doctoral dissertation). Doctoral thesis.

Palau, G., Stoesser, T., Rummel, A., & Rodi, W. (2007). Turbulent shallow flow through emergent vegetation. In *Iceh: Int. conf. on ecohydraulics.*

Parker, G. (1978). Self-formed straight rivers with equilibrium banks and mobile bed. part 2. the gravel river. *Journal of Fluid mechanics*, *89*(1), 127–146.

Pasche, E. (1984). 'turbulence mechanism in natural streams and the possibility of its mechanical representation. *Mitteilungen Institut für Wasserbau and Wasser-wirtschaft*(52).

Pasche, E., & Rouvé, G. (1985). Overbank flow with vegetatively roughened flood plains. *Journal of Hydraulic Engineering*, *111*(9), 1262–1278.

Patel, V., & Yoon, J. (1995). Application of turbulence models to separated flow over rough surfaces. *Journal of Fluids Engineering*, *117*(2), 234–241.

Petryk, S., & Bosmajian III, G. (1975). Analysis of flow through vegetation. *Journal of the Hydraulics Division*, *101*(ASCE# 114517 Proceeding).

Poggi, D., Katul, G., & Albertson, J. (2006). Scalar dispersion within a model canopy: measurements and three-dimensional lagrangian models. *Advances in Water Resources*, *29*(2), 326–335.

Pujol, D., Serra, T., Colomer, J., & Casamitjana, X. (2013). Flow structure in canopy models dominated by progressive waves. *Journal of hydrology*, *486*, 281–292.

Raupach, M. (1992). Drag and drag partition on rough surfaces. *Boundary-Layer Meteorology*, *60*(4), 375–395.

Raupach, M., Finnigan, J., & Brunet, Y. (1996). Coherent eddies and turbulence in vegetation canopies: the mixing-layer analogy. In *Boundary-layer meteorology 25th anniversary volume, 1970–1995* (pp. 351–382). Springer.

Raupach, M., & Shaw, R. (1982). Averaging procedures for flow within vegetation canopies. *Boundary-Layer Meteorology*, *22*(1), 79–90.

Ree, W. O., & Palmer, V. J. (1949). *Flow of water in channels protected by vegetative linings* (No. 967). US Dept. of Agriculture.

Rijn, L. C. v. (1984). Sediment transport, part ii: suspended load transport. *Journal of hydraulic engineering*, *110*(11), 1613–1641.

Rodi, W. (1997). Comparison of les and rans calculations of the flow around bluff bodies. *Journal of wind engineering and industrial aerodynamics*, *69*, 55–75.

Rollet-Miet, P., Laurence, D., & Ferziger, J. (1999). Les and rans of turbulent flow in tube bundles. *International Journal of Heat and Fluid Flow*, *20*(3), 241–254.

Sand-Jensen, K., JEPPESEN, E., NIELSEN, K., VAN DER BIJL, L., HJERMIND, L., NIELSEN, L. W., & IVLRSLN, T. M. (1989). Growth of macrophytes and ecosystem consequences in a lowland danish stream. *Freshwater Biology*, *22*(1), 15–32.

Shimizu, Y. (1994). Numerical analysis of turbulent open-channel flow over a vegetation layer using a κ-ε turbulence model. *Journal of Hydroscience and Hydraulic Engineering, JSCE*, *11*(2), 57–67.

Stoesser, T. (1997). Numerical modeling of reservoir sedimentation processes in prototype and physical model. *University of Karlsruhe*.

Stoesser, T., Kim, S., & Diplas, P. (2010). Turbulent flow through idealized emergent vegetation. *Journal of Hydraulic Engineering*, *136*(12), 1003–1017.

Stoesser, T., Liang, C., Rodi, W., & Jirka, G. (2006). Large eddy simulation of fully-developed turbulent flow through submerged vegetation. In *International conference on fluvial hydraulics, sep06-08. lisbon, portugal* (Vol. 1, pp. 227–234).

Stoesser, T., Salvador, G. P., Rodi, W., & Diplas, P. (2009). Large eddy simulation of turbulent flow through submerged vegetation. *Transport in porous media*, *78*(3), 347–365.

Stone, B. M., & Shen, H. T. (2002). Hydraulic resistance of flow in channels with cylindrical roughness. *Journal of hydraulic engineering*, *128*(5), 500–506.

Svensson, U. (1986). *Probe–an instruction manual* (Tech. Rep.). Swed. Meteorol. and Hydrol. Inst., Norrkping, Sweden.

Tanino, Y., & Nepf, H. M. (2008). Laboratory investigation of mean drag in a random array of rigid, emergent cylinders. *Journal of Hydraulic Engineering*, *134*(1), 34–41.

Tinoco, R. O., & Cowen, E. A. (2013). The direct and indirect measurement of boundary stress and drag on individual and complex arrays of elements. *Experiments in fluids*, *54*(4), 1509.

Tsujimoto, T., Shimizu, T., & Okada, T. (1991). *Turbulent structure of flow over rigid vegetation-covered bed in open channels. khl progressive report 1.* (Tech. Rep.). Hydraulic Laboratory, Kanazawa University, Japan.

Watson, D. (1987). Hydraulic effects of aquatic weeds in uk rivers. *Regulated Rivers: Research & Management*, *1*(3), 211–227.

Wu, F.-C., Shen, H. W., & Chou, Y.-J. (1999). Variation of roughness coefficients for

unsubmerged and submerged vegetation. *Journal of hydraulic Engineering*, *125*(9), 934–942.

Yang, W., & Choi, S.-U. (2010). A two-layer approach for depth-limited open-channel flows with submerged vegetation. *Journal of Hydraulic Research*, *48*(4), 466–475.

Yen, B. C. (1992). *Channel flow resistance: centennial of manning's formula*. Water Resources Publication.

Yen, B. C. (2002). Open channel flow resistance. *Journal of hydraulic engineering*, *128*(1), 20–39.

Appendix A

SEM formulation for 1D ADE

Consider a 1D Advecion Diffusion Equation:

$$f \quad : \quad \frac{\partial c}{\partial t} + V_s \frac{\partial c}{\partial z} = k \frac{\partial^2 c}{\partial z^2} \tag{A.1}$$

with the following mixed boundary conditions,

$$V_s c - k \frac{\partial c}{\partial z} = 0 \quad z = 0 \tag{A.2}$$

$$V_s c - k \frac{\partial c}{\partial z} = 0 \quad z = 1 \tag{A.3}$$

$$\tag{A.4}$$

Now consider the test function, $v(z) = \sum_j \phi_j(z)\tilde{v_j}$, where ϕ_j is the component of orthoginal basis. Using method of weighted residual to minimize the energy product of v and residual $r = f - k\frac{\partial^2 c}{\partial z^2}$.

$$(v, r) = 0$$

$$\int_\Omega v \frac{\partial c}{\partial t} dz + V_s \int_\Omega v \frac{\partial c}{\partial z} = k \int_\Omega v \frac{\partial^2 c}{\partial z^2} dz$$

Integrating by parts;

$$k\int_\Omega v\frac{\partial^2 c}{\partial z^2}dz = -k\int_\Omega \frac{\partial c}{\partial z}\frac{\partial v}{\partial z}dz + v\frac{\partial c}{\partial z}\bigg|_{\partial\Omega} \tag{A.5}$$

$$\int_\Omega v\frac{\partial c}{\partial t}dz + V_s\int_\Omega v\frac{\partial c}{\partial z}dz = -k\int_\Omega \frac{\partial c}{\partial z}\frac{\partial v}{\partial z}dz + v\frac{\partial c}{\partial z}\bigg|_{\partial\Omega} \tag{A.6}$$

where $\partial\Omega$ is the boundary of the domain. Consider the second term on the LHS of A.6, and integrate by parts,

$$V_s\int_\Omega v\frac{\partial c}{\partial z}dz = V_s\, vc|_{\partial\Omega} - V_s\int_\Omega c\frac{\partial v}{\partial z}dz \tag{A.7}$$

Now consider the second term on the RHS of A.6 and use A.2

$$vk\,\frac{\partial c}{\partial z}\bigg|_{\partial\Omega} = V_s vc|_{\partial\Omega} \tag{A.8}$$

Substituting A.7 and A.8 in A.6 and simplifying we get,

$$\int_\Omega v\frac{\partial c}{\partial t}dz = -k\int_\Omega \frac{\partial v}{\partial z}\frac{\partial c}{\partial z}dz + V_s\int_\Omega c\frac{\partial v}{\partial z}dz \tag{A.9}$$

Consider the approximate solution to c on the orthogonal basis, $\phi(z)$

$$c = \sum_i \phi_i(z)\tilde{c}_i \tag{A.10}$$

$$v = \sum_j \phi_j(z)\tilde{v}_j \tag{A.11}$$

Substituting A.10 in A.9 and simplifying, we get:

$$B\frac{d\underline{\tilde{c}}}{dt} = -kA\underline{\tilde{c}} + V_s C^T\underline{\tilde{c}} \tag{A.12}$$

where;

$\underline{\tilde{c}}$ is the solution vector,

$B = \sum_i \sum_j \int_\Omega \phi_i \phi_j dz$ is the Mass Matrix,

$A = \sum_i \sum_j \int_\Omega \frac{\partial \phi_i}{\partial z} \frac{\partial \phi_j}{\partial z} dz$ is the Stiffness Matrix, and

$C = \sum_i \sum_j \int_\Omega \phi_i \frac{\partial \phi_j}{\partial z} dz$ is the Convection Operator

Equation A.12 gives stable results only when the eigenvalues of A.12 are negative, which means that the energy of the system is decaying with time i.e. the system is stable. Eigenvalues for several values of V_s were calculated and it was found that for the system to be stable, $V_s \leq 0.061$ for $k = 0.02$. Fig. A.1 shows the eigenvalues for a stable and unstable case.

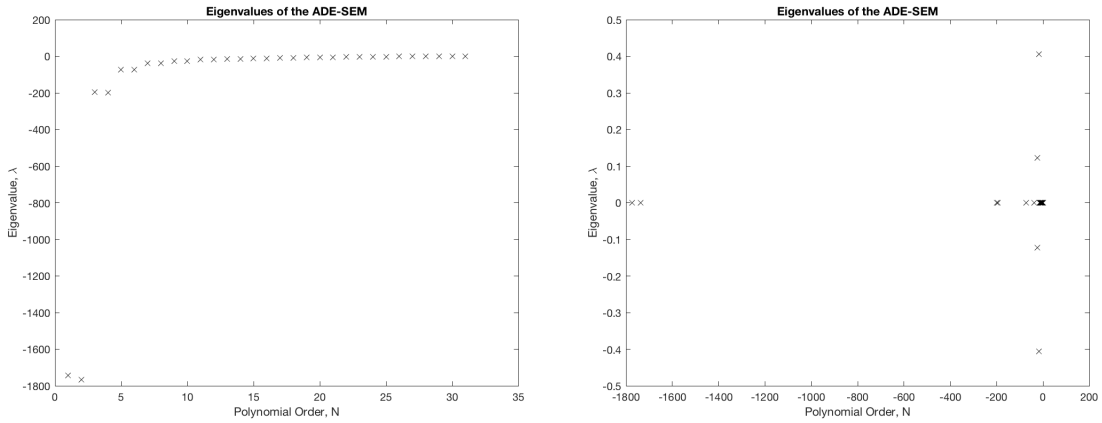

(a) V_s=0.061 (b) V_s=0.062

Figure A.1: Eigenvalues for stable and unstable cases